EMPA

Materials Science & Technology

UNI BASEL

Self-assembled Photonic Mesostructures for Water Splitting Photoanodes

Inauguraldissertation

zur

Erlangung der Würde eines Doktors der Philosophie

vorgelegt der

Philosophisch-Naturwissenschaftlichen Fakultät

der Universität Basel

von

Florent Boudoire

von Frankreich

Dübendorf, 2015

Genehmigt von der Philosophisch-Naturwissenschaftlichen Fakultät
auf Antrag von

Prof. Dr. Edwin C. Constable, Departement Chemie, Universität Basel

Dr. Artur Braun, Laboratory for High Performance Ceramics, Empa

Prof. Dr. Kevin Sivula, Laboratory for Molecular Engineering of Optoelectronic Nanomaterials, École Polytechnique Fédérale de Lausanne

Basel, den 17. Februar 2015

Prof. Dr. Jörg Schibler
Dekan der Philosophisch-
Naturwissenschaftlichen Fakultät

creative commons

Namensnennung-Keine kommerzielle Nutzung-Keine Bearbeitung 3.0 Schweiz
(CC BY-NC-ND 3.0 CH)

Sie dürfen: Teilen — den Inhalt kopieren, verbreiten und zugänglich machen

Unter den folgenden Bedingungen:

Namensnennung — Sie müssen den Namen des Autors/Rechteinhabers in der von ihm festgelegten Weise nennen.

Keine kommerzielle Nutzung — Sie dürfen diesen Inhalt nicht für kommerzielle Zwecke nutzen.

Keine Bearbeitung erlaubt — Sie dürfen diesen Inhalt nicht bearbeiten, abwandeln oder in anderer Weise verändern.

Wobei gilt:

Verzichtserklärung — Jede der vorgenannten Bedingungen kann **aufgehoben** werden, sofern Sie die ausdrückliche Einwilligung des Rechteinhabers dazu erhalten.

Public Domain (gemeinfreie oder nicht-schützbare Inhalte) — Soweit das Werk, der Inhalt oder irgendein Teil davon zur Public Domain der jeweiligen Rechtsordnung gehört, wird dieser Status von der Lizenz in keiner Weise berührt.

Sonstige Rechte — Die Lizenz hat keinerlei Einfluss auf die folgenden Rechte:

- o Die Rechte, die jedermann wegen der Schranken des Urheberrechts oder aufgrund gesetzlicher Erlaubnisse zustehen (in einigen Ländern als grundsätzliche Doktrin des **fair use** bekannt);

- o Die **Persönlichkeitsrechte** des Urhebers;

- o Rechte anderer Personen, entweder am Lizenzgegenstand selber oder bezüglich seiner Verwendung, zum Beispiel für **Werbung** oder Privatsphärenschutz.

Hinweis — Bei jeder Nutzung oder Verbreitung müssen Sie anderen alle Lizenzbedingungen mitteilen, die für diesen Inhalt gelten. Am einfachsten ist es, an entsprechender Stelle einen Link auf diese Seite einzubinden.

Acknowledgements

First I want to thank the Principal Investigator of my thesis, Dr Artur Braun, the Co-Principal Investigator of my thesis Dr Jakob Heier and my thesis advisor Prof Edwin C. Constable. Their guidance allowed me to hasten my research and inspired new development for this thesis. I also want to thank them for teaching and helping me in communicating my research to my peers and also to the general public. Here I would like to thank also Dr Rita Toth, MHV Fellow, that participated in the proposal and fund raising for this thesis and was always available for fruitful discussions. I am thankful also to Matthias Dzung, then bachelor student at ETH Zurich, for his help on the processing and characterization of hematite thin films.

I acknowledge Empa, the Swiss Federal Laboratories for Material Science and Technology, for granting me access to the ensemble of its infrastructure. My thesis project was a collaboration between two Empa laboratories, the Laboratory for High Performance Ceramics and the Laboratory for Functional Polymer. I am thankful to Prof Thomas Graule and the Laboratory for High Performance Ceramics for hosting me as a PhD student for three years. I am likewise grateful to Prof Frank Nüesch for granting me unlimited access to the equipment at the Laboratory for Functional Polymers. I want to thank also the different people that introduced me to the techniques available at Empa: Dr Ulrich Müller for atomic force microscopy; Dr Matthias Nagel for UV-visible spectroscopy; Schreier Daniel for scanning electron microscopy; Hansjürgen Schindler for static light scattering. I would like to thank also Dr Brian Sinnet from Eawag (Swiss Federal Institute of Aquatic Science and Technology) for introducing me to dynamic light scattering. I am also very grateful to the communication team of Empa and

Scientific communications

Parts of this thesis have been published in peer-reviewed literature and presented at scientific events.

Peer-reviewed papers

⬀. Florent Boudoire, Rita Toth, Jakob Heier, Artur Braun, and Edwin C. Constable. Hematite nanostructuring using electrohydrodynamic lithography. *Applied Surface Science*, 305:62–66, 2014.

⬀. Florent Boudoire, Rita Toth, Jakob Heier, Artur Braun, and Edwin C. Constable. Photonic light trapping in self-organized all-oxide microspheroids impacts photoelectrochemical water splitting. *Energy and Environmental Science*, 7:2680–2688, 2014.

Media Echo

⬀. Des petites bêtes alliées de la science. *CQFD radio broadcast on RTS (Radio Télévision Suisse)*, June 20, 2014.

⬀. De l'hydrogène produit avec un œil de mite artificiel. *Le Monde, newspaper article*, June 25, 2014.

⬀. Tiny balls of fire: How to gather more light for solar power. *The Economist, newspaper article*, June 28, 2014.

⬀. Florent Boudoire, Artur Braun, Edwin C. Constable, Jakob Heier and Rita Toth listed among the Top 100 Leading Global Thinkers of 2014. *Foreign Policy, Leading Global Thinkers of 2014*, November 17, 2014.

Oral Presentations

Florent Boudoire, Rita Toth, Jakob Heier, Artur Braun, and Edwin C. Constable. From polymers to oxides: A novel bottom-up approach to grow hematite sub-micro and nanostructures.

Empa PhD Students' Symposium, November 13, 2012, Dübendorf, Switzerland. - **Awarded with the 1st Place Oral Presentation Award.**

Florent Boudoire, Rita Toth, Jakob Heier, Artur Braun, and Edwin C. Constable. Efficient visible light trapping in patterned oxide heterojunction photoanodes for solar water splitting. *Abteilungstagung 2013: 21 Jahre Hochleistungskeramik im 21. Jahrhundert*, July 2, 2013, Dübendorf, Switzerland.

Florent Boudoire, Rita Toth, Jakob Heier, Artur Braun, and Edwin C. Constable. Visible light trapping in microstructured oxide photoanodes for solar water splitting. *Empa PhD Students' Symposium*, October 23, 2013, Dübendorf, Switzerland. - **Awarded with the 3rd Place Oral Presentation Award**.

Florent Boudoire, Rita Toth, Jakob Heier, Artur Braun, and Edwin C. Constable. Self-organized Micron-scale Architectures for Photonic Visible Light Trapping in Metal Oxide Water Splitting Photoanodes. *Seminar at iThemba Labs*, March 11, 2014, Somerset, South Africa.

Florent Boudoire, Rita Toth, Jakob Heier, Artur Braun, and Edwin C. Constable. Self-organized Micron-scale Architectures for Photonic Visible Light Trapping in Metal Oxide Water Splitting Photoanodes. *Seminar at University of Pretoria*, March 14, 2014, Pretoria, South Africa.

Florent Boudoire, Rita Toth, Jakob Heier, Artur Braun, and Edwin C. Constable. Visible Light Trapping in Microstructured Oxide Photoanodes for Solar Water Splitting. *DoE PEC Working Group Meeting*, April 21, 2014, Stanford, California.

Florent Boudoire, Rita Toth, Jakob Heier, Artur Braun, and Edwin C. Constable. Impact of Photonic Light Trapping on Photoelectrochemical Water Splitting in Hematite-coated mWO_3 Microspheroids. *E-MRS, Symposium I: Solution Processing and Properties of Functional Oxide Thin Films and Nanostructures*, May 30, 2014, Lille, France - **Awarded with the Graduate Student Award of Symposium I**.

Florent Boudoire, Rita Toth, Jakob Heier, Artur Braun, and Edwin C. Constable. Self-organized Micron-scale Architectures for Photonic Visible Light Trapping in Metal Oxide Water Splitting Photoanodes. *IPS-20, the 20th International Conference on Conversion and Storage of Solar Energy*, July 29, 2014, Berlin, Germany.

Florent Boudoire, Rita Toth, Jakob Heier, Artur Braun, and Edwin C. Constable. Photonic Light Trapping in Self-Organized All-Oxide Microspheroids Impacts Photoelectrochemical Water Splitting. *3rd General Meeting of the COST Action CM1140, Reducible Oxide Chemistry, Structure and Function*, November 14, 2014, Barcelona, Spain.

Florent Boudoire, Rita Toth, Jakob Heier, Artur Braun, and Edwin C. Constable. Shining Light on Water Splitting Photoanode Microstructures Self-Assembly. *BESSY II BER II User Meeting 2014*, December 4, 2014, Berlin, Germany.

Poster Presentations

Florent Boudoire, Rita Toth, Jakob Heier, Artur Braun, and Edwin C. Constable. From polymers to oxides: A novel bottom-up approach to grow hematite sub-micro and nanostructures. *Empa Evaluier-ungsbesuch durch Internationale Forschungskommission C*, November 7, 2012, Dübendorf, Switzerland.

Florent Boudoire, Rita Toth, Jakob Heier, Artur Braun, and Edwin C. Constable. From polymers to oxides: A novel bottom-up approach to grow hematite sub-micro and nanostructures. *29th annual meeting of the Swiss Working Group on Surface and Interface Science*, January 25, 2013, Fribourg, Switzerland.

Florent Boudoire, Rita Toth, Jakob Heier, Artur Braun, and Edwin C. Constable. Hematite nanopatterning using electrohydrodynamic lithography. *Workshop on Patterns and Hydrodynamic Instabilities in Reactive Systems*, May 14-17, 2013, Brussels, Belgium.

Florent Boudoire, Rita Toth, Jakob Heier, Artur Braun, and Edwin C. Constable. Efficient light trapping on patterned oxide photoanode surface for application in water splitting. *Swiss Nanoconvention*, May 23-24, 2013, Basel, Switzerland.

Florent Boudoire, Rita Toth, Jakob Heier, Artur Braun, and Edwin C. Constable. Impact of photonic light-trapping on photoelectrochemical water splitting in hematite coated mWO_3 microspheroids. *30th annual meeting of the Swiss Working Group on Surface and Interface Science*, January 24, 2014, Fribourg, Switzerland.

Florent Boudoire, Rita Toth, Jakob Heier, Artur Braun, and Edwin C. Constable. Visible Light Trapping in Microstructured Oxide Photoanodes for Solar Water Splitting. *MRS, Symposium F: Controlling the interaction between Light and Semiconductor Nanostructures for Energy Applications*, April 24, 2014, San Francisco, California.

Florent Boudoire, Rita Toth, Jakob Heier, Artur Braun, and Edwin C. Constable. Light Management in Nanostructured Water Splitting Photoanodes. *Swiss Nanoconvention*, May 21-22, 2014, Brugg Windisch, Switzerland.

Abstract

Solar water splitting is a relevant principle for the production of "green" hydrogen fuel. A wealth of different designs has been envisioned to produce hydrogen using sunlight. Among those designs Photoelectrochemical (PE) water splitting offers possible advantages regarding components integration and costs. This technology requires blending many materials requirements in a single component, such as solar light absorption, high electric conductivity, resistance to photocorrosion, and electrocatalytic properties. To achieve this goal it is necessary to build materials with emerging properties by discovering complex architectures at the micrometric and nanometric scales that can overcome bulk material limitations.

Materials of interest for application as photoanode for PE water splitting are metal oxides because of their resistance to corrosion. In this thesis I focused on two of these oxides, namely hematite (α-Fe$_2$O$_3$) and monoclinic tungsten oxide (mWO$_3$) since these materials have a relatively narrow band gap allowing absorption of a significant part of sun's irradiance. In a photoanode they were implemented as thin films on a conductive substrate. I proposed to investigate inexpensive and upscalable structuration processes for the formation of such photoanodes thin films with a controlled microstructure and studied the impact of such structures on the film PE performance.

Self-assembly strategies are bottom-up approaches which allow to grow structures with original morphologies at a low cost compared to top-down techniques such as lithography. I was particularly interested in strategies that would grant a fine control of the feature sizes. Two different processing techniques were implemented, a polymer templated sol-gel route and Electrohydrodynamic Lithography (EHL). Both techniques allowed to obtain metal oxides structures at the meso- to nanoscale. The polymer templated sol-gel route was the most successful strategy. It allowed to produce microspheroids with a tungsten oxide core and a hematite nanometric overlayer with control on the structure dimensions.

In addition to an in depth understanding of the different bottom-up approaches investigated, I proposed a complete description of the relationship between form and function in the film composed of tungsten oxide / hematite microspheroids. These films have significant photonic features linked to their original morphology and I discussed how their photoactivity is influenced by light trapping in these films.

Contents

Acronyms

Chapter 1

General Introduction

This thesis is focused on the implementation of metal oxide with innovative microstructures for application in a solar water splitting system. In this chapter I first analyse the economic, political and environmental relevance of hydrogen production from the sun energy. Then I depict the different technologies that could make the advent of "green hydrogen" possible and an extensive review of the functional materials that are at the core of these devices. It will become clear that metal oxides constitute a promising family of material for this application. However, because many requirements are needed in order to split water using sunlight, these oxides bear strong intrinsic limitations. Solutions to overcome these drawbacks are considered, with an emphasis on micro and nanostructuration which is the main topic of this thesis.

1.1 Solar hydrogen production: rationale, designs and challenges

Fossil fuels have been driving for over one century the development of our civilization due to their abundance and high energy density. However coal, oil and natural gas are nowadays recognized as environmentally harmful and are becoming a scarce resource. Since these fuels constitutes 87%[1] of the modern world energy consumption we need to find an environmentally friendly and renewable alternative. The diversification of fuel sources would also help to counter the globally growing number of energy security threats.

Alternative fuels include biodiesels, electricity, ethanol, hydrogen, natural gas and propane[2]. Among those fuels, hydrogen and electricity are the only zero tailpipe emission candidates. However hydrogen, unlike electricity, can be directly stored and transported. This is a major advantage of hydrogen over electricity, since the latter cannot decouple demand and resource. Another hydrogen asset is its use in most fuel cells. Fuel cells can be more efficient than internal combustion engines in converting chemical energy to mechanical energy. Internal combustion engines are limited by Carnot thermodynamic efficiency and have maximum theoretical efficiencies in the 40 to 60% range whereas fuel cells efficiencies are not limited by temperature and have higher theoretical values, up to 83%. Despite their high efficiencies, fuel cells are considered to be still too expensive and unstable to be a viable economic alternative to combustion engines. Ongoing research and development have brought about new materials and devices that damp these limitations and this technology is already reaching on the market.

Hydrogen chemistry makes this molecule an alternative fuel of choice. Yet its physical properties require significant structural changes before it can replace petroleum in our everyday life. Hydrogen has the lowest molecular weight of all molecules. This property results in a very low mass density compared to gasoline or diesel. It implies that liquid hydrogen stores 5 times less hydrogen bonds than gasoline in the same volume and 3 times more hydrogen bonds for the same mass (fig. 1.1). This property is accentuated by the fact that hydrogen is in gas phase at ambient temperature and pressure and needs compression to get close to its liquid density. Other physical properties linked to H_2 low molecular weight

Figure 1.1: Volumetric energy density as a function of gravimetric energy density of common hydrocarbons and hydrogen in liquid phase[3].

makes it hard to handle. Its low viscosity and high permeability in solids that make it prone to leakage. All these properties makes storage of hydrogen fuel a technical challenge. Even if hydrogen fuel is lighter than hydrocarbonates, implementing larger and leakage free tanks lead to an overall increased weight. It is not an issue for stationary applications where buried tanks can be implemented and volume and weight are not an issue. But for mobile applications,

solutions are developed to compress hydrogen and reach volumetric energy densities that are close to the liquid phase value. Cryo-compressed tanks[4–6], for example, is one of the successful technologies. Car testing showed a 1050 km autonomy with this technology[6], exceeding the benchmark of around 500 km for electric cars. Alternatively, rather than storing hydrogen in a tank, a possibility is to capture hydrogen at the surface and in the bulk of materials. Taking advantage of the smallness of the hydrogen molecule that makes it permeable to many materials, some of them can be converted to hydrides at ambient temperature. In this case hydrogen is absorbed inside the material, stabilized in a solid form as hydride ions, providing a high volumetric energy density. This hydrogen can be subsequently desorbed by heating the hydride material. This method is not yet established and research in this field aims at reducing the cost of the hydrides and their weight.

Nonetheless hydrogen storage is only the tip of the iceberg when it comes to an implementation as an alternative to fossil fuels. The smallness of the hydrogen molecule makes it permeable in most of the metals used in cars and in the industry, like steel, aluminium and magnesium. Whereas this property is beneficial for hydrogen storage, it is detrimental for the structural properties of the absorbing material. Hydrogen poisoning decreases the metal ductility and makes it brittle. In addition to phase transition of the metal that decrease their mechanical lasting, embrittlement can occur when the hydride ions react and form gas inside the bulk of the material.

The many challenges that hinder the change from an oil economy to a hydrogen economy calls for significant investments. A strong momentum needs to be generated to stir the socio-economical entities from short-term fixes of the status-quo, such as increasing internal combustion engine efficiencies, improving fossil fuels quality and capturing greenhouse gases emissions.

The depletion of cheap energy resources threatens energetic independence of governments. On the political side actions have been taken to decrease energy consumption and promote new energy sources. Hydrogen is globally considered as a viable alternative fuel and funding programs are implemented all over the world. Some government have also initiated programs to palliate the lack of infrastructures. In Europe, Germany has programmed the implementation of 50 refuelling stations by 2015[7]. In Switzerland, since 2012, bus fleets powered with fuel cells have been introduced[8]. More recently Empa, the Swiss Federal Laboratories for Material Science and Technology, has designed and built a solar to H_2 refueling gas station called the

"Future Mobility" demonstrator[9]. In the US biodiesels and electricity are the two major players but hydrogen technologies are also funded. Most of the effort towards hydrogen is located in California with funding for 28 new refuelling stations[10]. Japan also shows interest in hydrogen fuels with 100 stations planned for 2016[11]. But the pioneer in adopting the hydrogen economy is Iceland, which proposed in 2001 to get 20% of its vessel powered by hydrogen in 2020[12]. Large hydro- and geothermal resources would ease the energy transition in this country. Nevertheless this early commitment is now stagnating and no significant leap towards a hydrogen economy has yet been made[13].

The main drive for change may come from the industry. Oil companies have little interest in being the driving force for a change not withstanding that they are ready to provide hydrogen gas if the market demands it. But the automakers are interested in alternative fuels because of the political pressure for lower CO_2 emissions. In this context fuel cell technology is attractive, not only because it reduces CO_2 emissions, but also because it converts chemical energy directly to electricity. The availability of electrical power allows stripping off cars from their bulky mechanical parts. This advantageous feature could also be achieved with batteries, but fuel cell vehicles have higher autonomy than their electric counterpart. Therefore hydrogen fuel become more lucrative for longer travel distances and could complement electric vehicles for these applications. Ford, Daimler and Renault-Nissan have teamed up to decrease the cost of fuel cell technology and reach the market by 2017[14]. One goal of this association is also to promote the development of hydrogen infrastructures. Toyota and BMW have also concluded to a similar consortium and Toyota has planned the commercialization of a fuel cell car by 2015[15].

If governments and industries have made one step towards the transition to alternative fuels, including hydrogen, it does not imply that these fuels will be produced in a renewable and eco-friendly fashion. In the case of hydrogen, most of the current hydrogen production is based on the reaction of hydrocarbons or coal with water that also lead to the formation of carbon oxides by-products according to the water-gas shift reaction: $H_2O + CO \rightleftharpoons H_2 + CO_2$. A substitute of choice to avoid the production of "black hydrogen" would be water electrolysis. Water can be split to form hydrogen and oxygen gases using electrical energy. This method is attractive as water is close to be an inexhaustible resource on earth and the reaction products are carbon-free. However this method can only be considered a viable solution if the electricity driving the reaction comes also from sustainable and green sources.

Producing a clean, sustainable energy requires solutions adapted to each territory re-sources. This so-called "energy mix" will diverge from the current centralized energy grid to a decentralized system. Production of hydrogen by water electrolysis is symbiotic to this perspective. Indeed this method does not require bulky and expensive facilities, making it suited for on-site applications. In addition, hydrogen can be stored, which allows to decouple the energy consumption from the availability of the energy source. This is a crucial advantage when considering resources such as wind and solar energy which are intermittent by nature. In this context, solar hydrogen, i.e. the production of hydrogen by using sun energy, is a vast untapped resource. This technology would be a solution of choice in countries of the southern hemisphere where yearly irradiance is elevated.

photons $\xrightarrow[\text{(semiconductor)}]{\text{1. light absorption}}$ electron/hole pairs

2. charge separation

electrons $\xrightarrow{\text{3. HER catalysis}}$ hydrogen
$$2\,H^+_{(aq)} + 2\,e^- \longrightarrow H_{2(g)}$$

holes $\xrightarrow{\text{4. OER catalysis}}$ oxygen
$$2\,H_2O_{(l)} + 4\,h^{\boldsymbol{\cdot}} \longrightarrow 4\,H^+_{(aq)} + O_{2(g)}$$
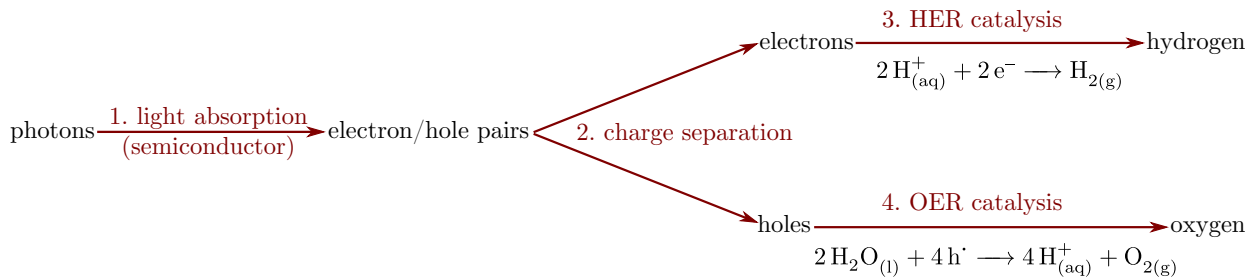
Figure 1.2: Physical and chemical processes required to split water using photons. HER stands for Hydrogen Evolution Reaction and OER stands for Oxygen Evolution Reaction.

However splitting water using sunlight is challenging since it requires gathering in one device many physico-chemical properties (fig. 1.2). A wide variety of designs have been im-plemented. These designs range from all-in-one solutions like photocatalysis, where particles or molecules in water absorb sunlight and produce both hydrogen and oxygen, to disjointed systems like Photovoltaic (PV) electrolysis, where a solar cell is wired to an electrolyser. But the required physical and chemical processes (fig. 1.2) are similar in all architectures. It is especially true for the designs involving two physically separated electrodes. These devices offer the advantage of physically separating the produced hydrogen and oxygen gases, provid-ing pure products and avoiding the formation of the highly flammable 2:1 oxyhydrogen gas (knallgas). In the case of systems comporting two separated electrodes, Jacobsson et al.[16] showed that one technology can easily be converted into another, making the advance in one sub-field relevant for the whole field. Figure 1.3 shows three different architectures involving separated electrodes and shows that the three concepts are equivalent in terms of their main physico-chemical features. We will now see in more details all the processes that lead to the formation of hydrogen using sunlight.
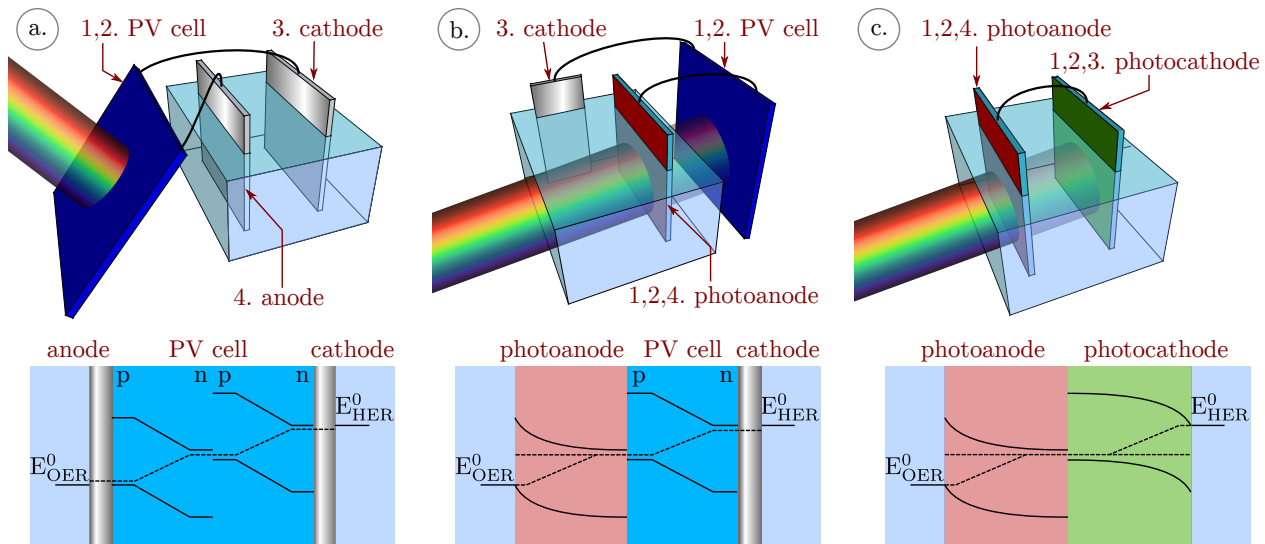
Figure 1.3: Possible designs that regroup the properties presented in figure 1.2 and their schematic energy band diagram: a. PV-electrolysis, double junction solar cell. b. Photoelectochemical water splitting assisted by a single junction solar cell. c. Photoelectochemical water splitting.

The driving force of the process is the absorption of photons and their conversion to charge carriers (fig. 1.2 1.). This property is achieved by a semiconductor. These materials possess an energy gap between their valence and conduction electrons. If a photon with a higher energy than this band gap propagates inside the material it can be absorbed. The photon energy is absorbed by promoting the transition of an electron from the valence band to the conduction band, leaving a hole in the valence band. Due to the presence of a band gap, this electron remains excited on longer timescales than its thermal relaxation would allow and it may be collected. However to avoid that the electrons radiate and return to their ground state, charge separation is needed (fig. 1.2 2.). The wavelengths of the visible range, from 300 to 1000 nm, constitute the wavelengths where the sun outputs most of its power. Hence semiconductor band gaps in the range 1 to 2 eV are preferred for solar powered applications.

The photogenerated electron/hole pairs can diffuse, drift or recombine in the semiconductor. Recombination occurs if the electron/hole pair is not separated spatially on faster time-scales than their thermal relaxation. Diffusion is the propagation of charges following a concentration gradient. Charges can accumulate at these interfaces if the kinetics of charge transfer at the semiconductor interfaces is slow compared to charge generation kinetics, leading to diffusion opposed to the current flow. An asymmetric junction is necessary in order to promote the drift of charges to the surface against diffusion and recombination. This junction is obtained by contacting the semiconductor with a material comporting different densities of

states. In a PV-cell this new material is usually another semiconductor. The band diagram of the PV-electrolysis design (fig. 1.3 a.) shows two PV-cells connected in series. Each PV cell is a stack of a n-type semiconductor and a p-type semiconductor. When these two semiconductors are contacted, charges flow between them until their Fermi levels equilibrate. This new equilibrium results in a gradient of electronic density as a function of the distance from the interface, called the space-charge layer. Within the space-charge layer, photogenerated charge carriers drift, following the potential gradient, and can reach the material surface before recombination. In this case the space-charge layer results from solid state physics, however it can also be obtained by contacting the semiconductor surface with a gas or a liquid. This effect is used for example in Photoelectrochemical Cell (PEC) (fig. 1.3 b. and c.) where metal oxides photoanodes and/or photocathodes are dipped in water. In that case water molecules bond to the metal oxide surface forming hydroxyl groups. These new orbitals result in new electronic states at the surface, the so-called "surface states". Like for the semiconductor heterojunction, a space-charge layer is formed when the Fermi level of the surface states and the semiconductor equilibrates. The band diagrams in figure 1.3 b. and c. show examples of space-charge layer in photoanodes and photocathodes resulting from the formation of surface states.

We have seen that a semiconductor under illumination can behave as a current generator. However, this photocurrent will not evolve hydrogen and oxygen unless different catalytic properties are met (fig. 1.2 3. and 4.). Indeed water splitting does not rely only on the number of charge carriers that reach the interface with water. This reaction is endothermic and requires also its internal energy to be provided by the electric potential difference between the photogenerated electrons and holes. Water splitting (reaction (1.5)) occurs through two redox reactions, the Oxygen Evolution Reaction (OER) and the Hydrogen Evolution Reaction (HER). For each half reaction different reactants and products can be considered (reactions (1.1) to (1.4)). The reduction reaction (1.1) and oxidation reaction (1.2) are preponderant at low pHs while the reduction reaction (1.3) and oxidation reaction (1.4) are preponderant at high pHs. While the reduction (E_{red}^0) and oxidation (E_{ox}^0) potential energies are pH-dependent, the internal energy of the water splitting reaction remains constant ($\Delta E = E_{red}^0 - E_{ox}^0 = 1.23V$). Therefore the difference in potential energy between electrons and holes would need to be at least of 1.23V in order to split water.

$$4\,H^+_{(aq)} + 4\,e^- \xrightleftharpoons{E^0_{red1}} 2\,H_{2(g)} \qquad (1.1)$$

$$4\,H_2O_{(l)} + 4\,e^- \xrightleftharpoons{E^0_{red2}} 2\,H_{2(g)} + 4\,OH^-_{(aq)} \quad (1.3)$$

$$2\,H_2O_{(l)} + 4\,h^+ \xrightleftharpoons{E^0_{ox1}} 4\,H^+_{(aq)} + O_{2(g)} \qquad (1.2)$$

$$4\,OH^-_{(aq)} + 4\,h^+ \xrightleftharpoons{E^0_{ox2}} 2\,H_2O_{(l)} + O_{2(g)} \qquad (1.4)$$

$$2\,H_2O_{(l)} \xrightleftharpoons{\Delta E} 2\,H_{2(g)} + O_{2(g)} \qquad\qquad (1.5)$$

Nevertheless a cell delivering these 1.23V of photovoltage is not sufficient to split water. Overpotentials arise from the kinetics of water electrolysis. These kinetic aspects are usually gathered in three categories, namely activation, concentration and resistance overpotentials. Activation overpotentials relate to the kinetics of charge transfer at the electrode/liquid interface. It includes the kinetics of chemisorption of the reactants on the electrode, the kinetics of reaction with the electrode charges and the kinetics of desorption of the reaction products. These aspects constitute the catalytic properties of an electrode. A good catalyst accelerates the charge transfer processes and thus lowers the activation overpotentials. In water splitting, activation overpotentials are especially present at the anode where the surface must store and transfer four holes at the same reaction site. Hence most of current research is focused on anodes and photoanodes development. Other overpotentials can also arise from a low concentration of charge carriers at the electrodes surface. This concentration overpotential is linked to the solution conductivity, i.e. the ionic strength of the solution and the kinetics of diffusion of the ions. Yet not only ions must reach reaction centers, the photogenerated charge carrier must also drift to these sites. The electrical resistance that can build up between the charge generation regions and the solid/liquid interfaces also lead to significant overpotentials. These resistance overpotentials are a consequence of the cell design. For example in the case of PV-electrolysis (fig. 1.3 a.), wiring the PV to electrodes result in contact and cable resistance, whereas for more integrated systems like photoelectrodes (fig. 1.3 b. and c.) the light absorption region is in microscopic proximity with the catalytic sites.

We have seen that the different designs for water splitting using sun's energy bear the same physico-chemical properties. The main difference lies in the scale of the spatial separation between the light absorber and the catalyst. In a photoelectrode the distance between these two features is nanometric to micrometric whereas this distance is macroscopic in the case of a PV-cell connected to an electrode. This separation makes PV-electrolysis development easier considering that light convertion and catalysis can be optimized separately. The solar

cell materials can be optimized for visible light absorption and charge separation and does not need to be corrosion resistant and catalytically active. De facto photoelectrode implementation is challenging because all these requirements have to be satisfied by one material.

On one hand the physical separation in PV-electrolysis relaxes the materials requirements. But on the other hand wiring the components together leads to increased resistance overpotentials and more photovoltage is needed from a solar cell than from a photoelectrode. The overpotentials in PV-electrolysis are further increased because their current densities are typically 10^2 to 10^4 times higher than photoelectrodes current densities. Indeed for a constant electrical impedance (Z), linked to the different kinetic resistances presented previously, increasing the current (I) leads to an increase of the overpotential (V) according to Ohm's law ($U = Z \times I$). The overpotentials increase in an ohmic fashion at low current densities. At higher current densities, according to Tafel's empirical equation, the overpotentials increase becomes exponential. In the end typical values of photovoltage needed to split water in the case of PV-electrolysis is around 2V while it usually ranges from 1.5 to 1.8 volts in the case of PEC.

So each design bears different challenges, but in the end what will decide the preponderance of a given strategy is the cost of the produced hydrogen. This would promote aspects such as material costs and stability rather than device Solar-To-Hydrogen (STH) efficiency. It is difficult to estimate the cost of hydrogen from the emerging solar-to-hydrogen devices. Krol and Grätzel[17] proposed estimated cost for PV-electrolysis around \$8/kg whereas PE water splitting, due to its compact device integration and lower material costs, could lead to cheaper hydrogen, in the \$3-5/kg range. In this thesis we will focus on the development of a photoanode for PE water splitting that could fit for example in designs depicted in figure 1.3 b. and c., using the so-called "two-step" photoexitation systems. In the next sections we will see the materials of interest for such a device, the importance of light management to overcome these materials limitations and how to achieve this light management by a control of the photoanode microstructure.

1.2   Candidate materials for photoanode thin films

Photoanodes for PE water splitting are typically composed of a thin film coated on a transparent conductive substrate. These transparent substrates are required because for most

applications, light which is not absorbed by the photoanode can be used by other devices, such as a solar cell or a photocathode. Classic conductive transparent substrate are obtained by coating a nanometric conductive thin film, Indium Tin Oxide (ITO) or Fluorinated Tin Oxide (FTO), on a glass slide. Thin films composed of semiconductor materials are subsequently deposited, by physical or chemical means, at these substrate surfaces. The semiconductor thin film composition will determine the critical properties of the photoanodes. As mentioned in the previous section, photoanodes have to gather a wide range of properties, namely resistance to corrosion, visible light absorption, charge carrier separation and OER catalysis. We will see in more details these constraints imposed to photoanode thin films and candidates materials that could fulfill these requirements.

Firstly let us consider the semiconductor band gap requirements. Most of the sun's irradiance is located at wavelengths between 300 nm and 1000 nm, i.e. in the visible range. In order to absorb a large part of this wavelength range the semiconductor band gap has to be smaller than 3 eV. Indeed, the longest wavelength (λ_{max}) that a semiconductor of band gap E_g can absorb is limited to $\lambda_{max} = \frac{hc}{E_g}$, with h the Planck's constant and c the speed of light. Longer wavelengths with less energy will not be absorbed. Hence a semiconductor with a 3eV band gap is already absorbing light only up to 400nm wavelength. Nevertheless small band gaps also mean a low photovoltage. We have seen in the previous section that 1.5 to 1.8V of potential difference between photogenerated electrons and holes are typically needed in order to split water in a PEC. This means that decreasing the semiconductor band gap in order to absorb more of sunlight will be detrimental for the photoanode performance as more additional bias will be needed to split water. As a consequence, the semiconductor band gap has to offer a tradeoff between light absorption and photovoltage. Figure 1.4 shows the band edge position of candidate materials for photoanodes. These semiconductors absorb in the visible and near-UV range and possess a valence band below the OER potential. Their conduction band is close to the HER potential and need only limited additional bias potential in order to split water.

Solar cells are usually composed of non-oxide semiconductors, for example n-doped silicon and GaAs (fig. 1.4, Si band edges are shifted to lower energies when n-doped), that absorb light at visible wavelength that could also be implemented in photoanodes. These photoanodes can potentially deliver high photocurrents but have a stability issue. During operation the photogenerated holes tend to oxidize the photoanode surface instead of oxidizing water. Protective coatings have been developed in order to shield this kind of photoanodes from cor-
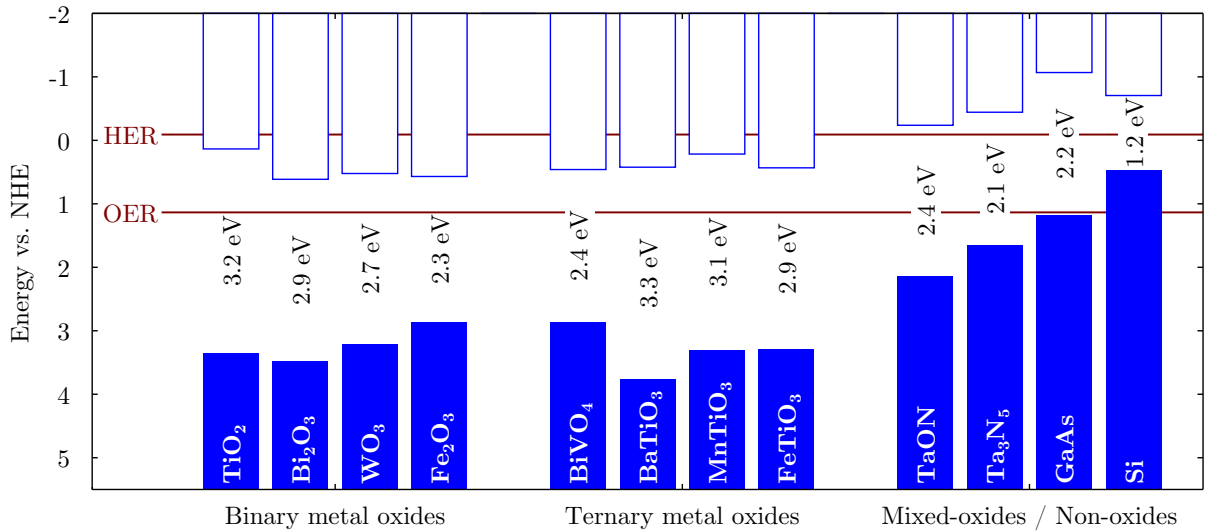
Figure 1.4: Band edge position of different photoanode materials versus OER and HER energy potentials, pH = 2. Band edge values from Bak et al. [18], Chun et al. [19], Van de Walle and Neugebauer [20], Ding et al. [21].

rosion. Obtaining a continuous, conductive and stable film on top of such photoelectrodes is challenging. Yet significant advances have been made by different groups. Kenney et al. [22] stabilized n-Si for 80 hours using a nickel ultra-thin film. More recently Hu et al. [23] developed ultrathin "electrically leaky" amorphous TiO_2 thin films that allowed stabilization of n-Si, GaAs, and GaP photoanodes for more than 100 hours. In addition to the issue on stability, such photoanodes have poor charge transfer kinetics to the electrolyte and require a catalyst at their surface to drive the OER reaction.

Another class of non-oxide/mixed-oxide semiconductor, tantalum (oxy)nitrides, such as TaON and Ta_3N_5, have optimal band edges position compared to HER and OER energy potentials (fig. 1.4). Murphy et al. [24] calculated STH theoretical efficiencies close to the hypothetical theoretical maximum, associated with the relatively small band gaps and opportune band edge positions. The application of such materials as photocatalysts was first investigated by Hitoki et al. [25,26]. These semiconductors are suited for one-step photoexitation strategies using a sacrificial reagent [25–27]. The implementation as a photoanode was also investigated and showed significant photocurrents [28]. Still self-oxidation by the photogenerated holes is here again a strong concern and the surface of those materials passivates within minutes in operando conditions.

In this context oxides are the solution of choice in terms of stability against photocorrosion.

Many oxides have a valence band energy maximum which is far more positive than the OER energy potential. Hence photogenerated holes will thermodynamically tend to oxidize water rather than the metal cations when accumulating at the reaction centers.

The seminal work from Fujishima and Honda[29] introduced TiO_2 in the anatase phase as the first metal oxide investigated for photolysis of water. This material has a large band gap (3.2 eV, fig. 1.4) and can drive the overall water splitting reaction. But as we have seen before, such a large band gap leads also to poor solar light absorption and TiO_2 absorbs only Ultraviolet (UV) light, i.e. 4% of the irradiance from the sun. Band gap narrowing could be achieved for use as photoanode material by different doping strategies[30–34]. Still the lattice defects introduced by atom substitution can act as recombination centers for the photogenerated charge carriers and impede the photoanode performance. Another strategy to overcome the low absorption of TiO_2 in the visible range is the sensitization by a dye molecule. Seminal work by Anderson et al.[35] showed that photocatalyst molecules adsorbed at the TiO_2 surface could transfer photogenerated electrons to the semiconductors while oxidizing water. If these molecules absorb light at longer wavelengths than TiO_2, significant light absorption in the visible range can be achieved.

Since the discovery of the photoelectrochemical properties of TiO_2 different oxides have been scrutinized for photoanodes. Hematite (α-Fe_2O_3), tungsten trioxide (WO_3) and more recently bismuth vanadate ($BiVO_4$) are heavily studied as they gather most of the properties required by a photoanode material. All these oxides are abundant on earth, i.e. relatively inexpensive, and resistant to photocorrosion in a broad range of pHs.

Hematite has the smallest band gap of these three oxides, in the 1.9 to 2.2 eV range. It absorbs yellow to ultraviolet light, and gets from this optical property its red-brown color. This absorption in the visible range makes it the oxide with highest theoretical STH efficiency in the 15% range[36]. Hematite is stable at neutral to basic pHs and this material constitutes a photoanode of choice for alkaline photoelectrolysis.

However, like many oxides, hematite possesses a short charge carrier recombination length compared to its absorption depth. Hematite has an indirect band gap[37], which makes it relatively transparent. Indeed, for a semiconductor with an indirect band gap, the maximal valence band energy level has a different crystal momentum as the minimal conduction band energy level. Hence to excite an electron from the valence band to the conduction band, not only absorption of a photon is required but also absorption of a lattice phonon. The photons

can carry the energy required to excite an electron but cannot provide the required momentum, and the electron needs also to absorb a lattice phonon in order to reach the valence band. Hence the probability of electron transition through an indirect band gap semiconductor like hematite is low and light has to travel in the crystal lattice over a long distance. As a hint on the hematite film thickness needed to absorb a photon, considering Lambertian absorption, it can be deduced from the work of Marusak et al.[38] that hematite's optical thickness is 44.6 nm at a wavelength of 400 nm.

So on one hand hematite is a transparent material and photon absorption occurs over several tenth of nanometer from its surface. But on the other hand the photogenerated holes have to travel to the semiconductor surface to oxidize water while electrons have to reach the FTO back contact. As a consequence, the material has also to gather good electron conductivity and hole conductivity. Hematite doping has been implemented by different research groups[39–41]. A successful strategy is n-doping of hematite, with Si^{4+} or Ti^{4+} for example, that lead to an increase of the majority charge carriers (electrons) and balance the poor electronic conductivity of hematite. Then the diffusion of minority charge carrier (holes) to the surface have also to be addressed. Since hematite's band gap is indirect, the recombination of photogenerated electrons and holes is less likely than in a direct band gap semiconductor since it requires phonons to shift the excited electron momentum. So recombination is more likely to occur at lattice defects in this material. Most synthesis techniques are prone to introduce lattice defects in hematite. These defects may increase the charge carrier concentration but they usually act as recombination centers. Hence the minority charge carrier diffusion length before recombination is in the nanometric range. It was estimated by different authors[37,42] to be ranging from 1 to 5 nm and was confirmed experimentally by the author in this thesis.

The combination of extremely short minority charge carrier recombination length and large light absorption depth is one of the major limitations to the use of hematite as photoanode material. Indeed the transparency issue of hematite could be undertaken by increasing the hematite film thickness. This is typically done with silicon solar cells, which also possess an indirect band gap and are implemented with thicknesses in the sub-millimeter range. However, the poor conductivity of hematite leads to a tremendous decrease in photocurrent as soon as the thickness is exceeding the 10th of nanometer range. We will see in section 1.3 how this limitation can be overcome by non-Lambertian absorption scheme using nanostructuring strategies.

Another concern when dealing with hematite is the charge transfer at the hematite / liquid junction. The surface of a material in contact with another medium has a different atomic structure than its bulk. Hence the surface has particular molecular orbitals leading to new electronic states called "surface states". Holes accumulate at these states and can either participate to the OER or recombine with thermalized electrons from the conduction band[43]. The impact of the recombination at surface states has been characterized using hole scavengers in solution[42,44,45]. A hole scavenger can suppress recombination of hole at surface states by speeding up the OER kinetics. The impact of surface recombination can be characterized by comparing the photocurrent response with and without a hole scavenger. It was shown that surface recombination leads to overpotential in the $0.4 - 0.6$V range[42,45]. Klahr et al.[46] investigated the role of the surface states during operation using impedance spectroscopy. They proved that surface state not only act as recombination centers but also strongly mediate the charge transfer to water. They even showed that most of holes transferred to water are actually coming from these states rather than from the valence band.

Also, because of the slow kinetics of charge transfer, holes tend to accumulate at the hematite surface and this accumulation promotes charge recombination at surface states. This issue regarding charge injection kinetics is linked to the low catalytic activity of hematite. The OER proceeds through a 4-electrons oxidation of water but the modalities of this reaction are not known. Different authors[47,48] proposed for example that iron would store holes upon being oxidized. Since it would be difficult thermodynamically to store 4 holes by oxidation of only one iron, it is probable that multiple iron sites are involved in the splitting of one water molecule and the low probability of such event would create a kinetic bottleneck.

Different surface treatments have been applied to hematite in order to increase its Faradaic efficiency. The goal is to passivate the surface states that have slow kinetics towards water oxidation[49,50] and to promote catalytic centers, sometimes even adding supplementary electrocatalyst material at hematite surface[41,51-54].

In these different studies the nature of the surface states remained unclear. First clues about their nature was brought by Braun et al.[55] who achieved an operando investigation of these surface states using soft X-ray spectroscopy. By developing a custom in-situ cell they could perform oxygen Near Edge X-ray Absorption Fine Structure (NEXAFS) measurement at the hematite/water interface while applying a bias potential and shining simulated solar light on the sample. They identified not one but two electron-hole states that only appear

in the oxygen NEXAFS spectra upon illumination and application of a bias higher than 100 mV vs Reversible Hydrogen Electrode (RHE). These two hole states, which were already hypothesized by Kennedy and Frese[37] thirty years ago, were attributed to different electron hopping mechanisms. The lowest energy level corresponds to a metal to ligand charge transfer (Charge Transfer Band (CTB)) and the highest energy levels would correspond to a metal to metal charge transfer (Upper Hubbard Band (UHB)). While both kind of holes participate to water splitting their different energy level position impact their reactivity. On one hand the UHB energy would be located between the conduction band and the OER potential, hence it would promote charge recombination rather than charge transfer to oxidize water. On the other hand the CTB would be located near the valence band depletion layer and would be more favorable to water oxidation and less prone to recombination. It is therefore possible that the different overlayers investigated in the literature[49,50] passivate the UHB and promote the CTB.

Another oxide that has been under heavy scrutiny since the seventies is monoclinic tungsten trioxide (mWO$_3$). It has a band gap in the 2.5 to 2.7 eV range and therefore can absorb light up to 450 nm wavelength, giving this material an intense yellow color. The wider band gap of this material compared to hematite lead to lower theoretical efficiencies. But in practice this oxide is usually easier to implement as an efficient photoanode due to a larger hole diffusion length of 150 nm[56]. The increased band gap of mWO$_3$ also comes with a down shift of its valence band which provide more potential energy for the holes to oxidize water. In addition WO$_3$ exhibits good catalytic properties towards the OER. Hence very low onset potentials are obtained for this material, around 0.2 V vs AgCl at pH=7, against 0.6 V vs Ag/AgCl for hematite.

Another oxide that has drawn attention since the seminal work of Kudo et al.[57] is bismuth vanadate (BiVO$_4$) in the monoclinic scheelite structure. Like most metal oxides this material suffers from poor charge separation and conduction. Similar approaches as in the case of hematite have been investigated, like N-doping by substitution of V^{5+} by Mo^{6+}, and W^{6+}, allow to increase the majority charge carrier concentration[58,59]. A fine control of a spray pyrolysis process even allowed Abdi et al.[60] to produce BiVO$_4$ photoanodes with a gradient doping of tungsten. This interesting approach leads to a strong band bending from an intrinsic to a highly N-doped extrinsic bismuth vanadate and promotes charge separation.

Research has also focused on discovering new stable metal oxides phases that could gather

all the properties required by a photoanode material and compete with the currently investi-gated metal oxides. High throughput combinatorial approaches[61–63] have been used in order to identify candidates in two and three cations systems. Resulting from these studies differ-ent potential photoanode materials were identified, for example $FeVO_4$[63]. Nevertheless the intricate interplay of nanostructure and microstructure effects in addition to the material com-position makes it difficult to assess if the observed difference in photocurrent can actually be attributed to the chemical composition of the samples.

We have seen that different metal oxides satisfy some of the many criteria required by a photoanode i.e. visible light absorption, resistance to photocorrosion and low-costs. Yet they all suffer from poor charge separation and diffusion coupled to a relative transparency. We have already summarized different strategies to improve charge collection by tuning the photoanode material composition at the bulk and the surface. We will see in the next section that additional improvements can be achieved by controlling the electrode nanostructure and microstructure in order to manage light and photogenerated charges flow.

1.3 Photoanodes architectures at the meso and nanoscales for light and charges management

The implementation of smart nanostructuring and microstructuring has been widely used to overcome materials limitations in the field of heterogeneous catalysis and in the field of pho-tovoltaics[64]. The strategies implemented in these fields can generally be adapted to improve photoelectrodes performances and efficient systems described in the literature always rely on the original properties emerging from the photoelectrode structure. In general the design of a photoanode structure aims at improving one or several of the properties required in order to split water using the energy from sun's photons (fig. 1.2): light absorption, charge separation and OER catalysis. I will focus on the strategies applied to metal oxide photoanodes but the exposed strategies can usually be applied to any kind of material.

Perfect single crystals usually exhibit poor catalytic activity compared to highly textured surfaces. Somorjai[65] calls rough surfaces "flexible" surfaces where numerous surface defects lead to a thermodynamically favored restructuration of atoms and bonds compared to single

crystals where strong ordering at the surface make atomic rearrangement more "rigid". This is one reason to the poor performance of single crystals compared to polycrystalline samples.

Another advantage of nano and microstructuring photoanodes is the increase of surface area. Large surface areas increase the proximity of photogenerated holes in the material bulk to the solid/liquid interface. This design can overcome recombination of charges due to the short minority charge carrier diffusion length in metal oxides. In the case of hematite for example, today's benchmark efficiencies are obtained with highly faceted hierarchical nanostructures, the so-called "cauliflowers" from Kay et al.[66]. The structure help driving the minority charge carriers to the semiconductor/liquid junction while silicon doping is employed in order to increase the majority charge carriers concentration and obtain good electron collection. This strategy has given rise to a wide range of hematite nanostructures such as nanorods[67], nanotubes[68] and stellates[69]. A similar strategy was employed with mWO_3 by different authors[70–74]. Solarska et al.[74] for example used 2.5 μm thick films to absorb light efficiently while the path length for holes was maintained below the hole diffusion length of the oxide (150 nm[56]) as a result of the nanoparticulate nature of the film. Nevertheless high surface areas have one major drawback, they decrease the photoanode photovoltage[64,75]. Increased surface area leads to a decrease of charge concentration at the surface that damps the splitting of quasi Fermi levels[76–79]. As a consequence a ten fold increase in surface area leads to a potential drop of 0.6V[75].

Another architecture that can improve both charge separation and photovoltage consist in stacking different metal oxides in n-n heterojunctions. We have seen in section 1.1 that efficient water splitting can be achieved using a photoanode and a photocathode in series using a 2 photons configuration in order to reach the required photopotential. This dual band gap strategy can also be achieved within one photoelectrode in order to obtain increased photovoltages and improve charge separation. In a photoanode the goal is to match the band edge position of each semiconductor in order to favor electron flow to the back contact and hole flow to water. To achieve this effect the valence band of the semiconductor in contact with water must be closer to the OER potential than the valence band of the semiconductor in the rear. This way the holes can be driven efficiently to water. In order to also drive electrons to the back contact the conduction band of the semiconductor in the rear must also be closer to the HER potential than the semiconductor contacting water. This strategy is usually implemented in highly structured photoanodes in order to maximize charge collection. Different groups[80–82] have used for example N doped silicon as a support for different metal

oxides. The advantage is that the metal oxide can shield the silicon from corrosion while the band edges of silicon are generally well aligned with those of the oxide in order to achieve a successful heterojunction. Nevertheless pinholes in the oxide overlay can easily lead to the dissolution of the silicon and compromise the electrode stability. Other groups[83–85] have oriented their research towards all-oxide n-n heterojunctions. In these studies tungsten oxide constitutes the rear semiconductor with a high surface area and is conformally coated with another metal oxide. Sivula et al.[83] and Mao et al.[85] studied $WO_3/\alpha\text{-}Fe_2O_3$ heterojunctions and showed improved light absorption and photocurrents compared to bare WO_3 samples. Su et al.[84] showed the implementation of a different system, a $WO_3/BiVO_4$ heterojunction, that also showed similar improvement. In a sense the work of Abdi et al.[60] that I described previously, where a gradient of tungsten doping was implemented in $BiVO_4$ photoanodes, also constitute an extreme case of all-oxide n-n heterojunction.

We have seen that structuration of photoanodes can lead to improved catalysis and charge separation. Besides these aspects, rough photoelectrodes also benefit from improved absorption properties. Indeed smooth surfaces at the nanoscale and microscale strongly reflect light by specular reflection. In addition, under normal light incidence and without reflective back reflector, refracted light only propagates once in smooth films. On the contrary textured surfaces scatter light thus decreasing reflection. Scattering centers also deviate incident rays from normal incidence and increase light path in the material hence increasing the absorption depth. This property is very interesting when working with metal oxides since these materials are relatively transparent because of their indirect band gap. For that reason micrometric thin films are usually implemented in order to absorb solar light. A clever light management in photoanodes can allow decreasing the film thickness and therefore improving current collection. A lot of different light trapping schemes have been investigated in the field of photovoltaics such as plasmonic nanoparticles, antireflective coatings, back reflectors, photonic crystal microstructures, and photonic resonators (see fig. 1.5). Most of these strategies have also been applied to photoelectrodes.

Plasmonic effects occurring in metal nanoparticles are sometimes used in order to improve absorption properties of photoactive devices. Gold or silver nanoparticles are deposited at the photoactive material surface or embedded in the material bulk (fig. 1.5 a.). For such particles, conduction band electrons can oscillate in an Electromagnetic (EM) field, for example light EM field. Depending on the relative size of the particle compared to light wavelength the electron oscillations can enter resonance and form an intense EM field localized in the vicinity
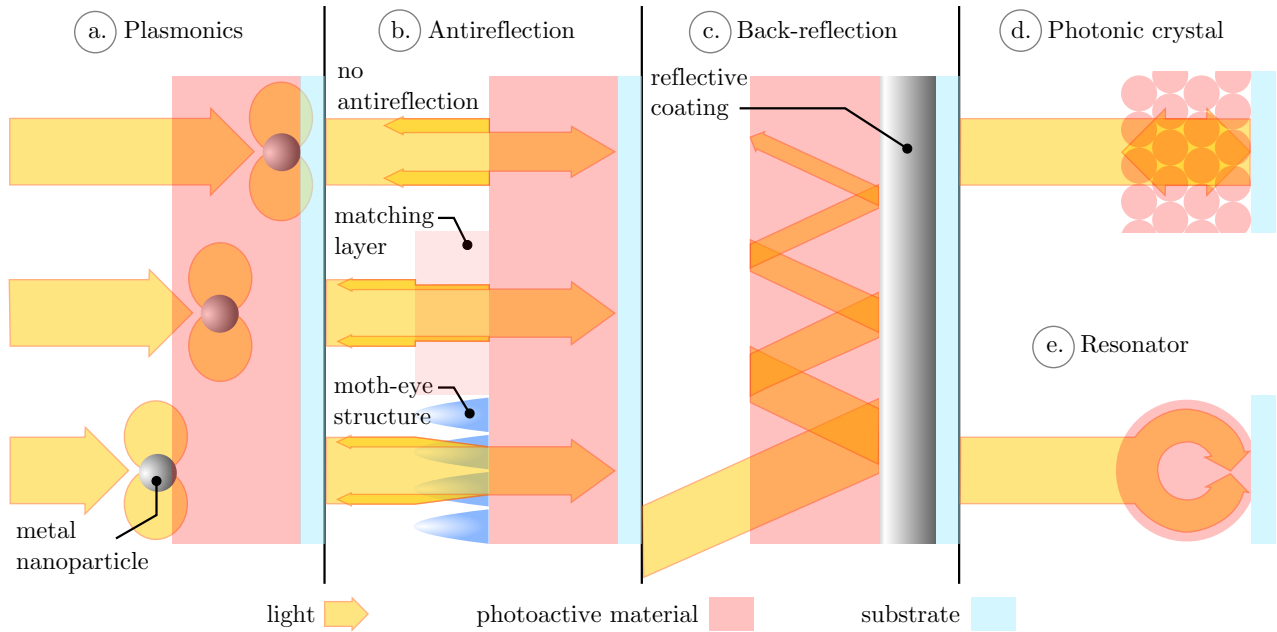
Figure 1.5: Different light trapping approaches: a. Plasmonic metal nanoparticles at the surface and in the bulk of the photoanode thin film; b. Reflection with and without antireflection layers; c. Metal back reflector to obtain total internal reflection; d. Light trapping in a photonic crystal structure; e. Light trapping in a photonic resonator structure.

of the nanoparticle. Warren and Thimsen[86] exposed different motivations for the use of plasmonic metal nanoparticles in photoelectrodes. If the nanoparticles are located near the surface they can act as an antenna and confine light near the photoanode surface. This way light absorption is promoted near the semiconductor/liquid junction reducing the distance that holes have to travel in order to reach water. The plasmonic resonance decays within a few femtoseconds either by reemitting a photon or by emitting a "hot electron". Therefore the plasmonic nanoparticles can also act as a sensitizer by injecting photoexcited electrons in the semiconductor material conduction band. Plasmon enhanced light absorption was achieved in mWO_3 photoanodes by Solarska et al.[87] using silver nanoparticles. They coated tungsten oxide on top of a silver film constituted of nanoislands in order to shield the metal from corrosion during processing and operation. Thimsen et al.[88] also reported the use of plasmonic gold nanoparticles to improve hematite light absorption. Hematite absorption was indeed improved by the presence of such nanoparticles. Still the photocurrent obtained from these films were decreased compared to control samples and Thimsen et al.[88] proposed that the metal particles promote surface recombination. In order to avoid these recombination phenomena Thomann et al.[89] embedded the gold particles in silica shells and showed photocurrent enhancements

at the wavelengths of resonance of the nanoparticles. More recently Gao et al.[90] also showed strong plasmonic enhancements of hematite ultra-thin films coated on gold nanopillar arrays.

We have seen that textured surfaces in general are less reflective that flat and smooth surfaces. Additional strategies can be implemented in order to decrease reflection. Metal oxides have a high refractive index leading to a strong optical contrast with the ambient medium where light propagates before reaching the surface. At normal incidence on a flat surface the reflectance (R) can be calculated as a function of the semiconductor refractive index (n_1) and the medium refractive index (n_0):

$$R = \left(\frac{n_0 - n_1}{n_0 + n_1} \right)^2 \tag{1.6}$$

In the case of metal oxides in water the reflectance is significant, in the 10 to 30% range. The simplest way to decrease reflection is to use an index-matching thin film at the semiconductor surface (fig. 1.5 b.). It is straightforward to deduce from eq. (1.6) that the optimal refractive index of this matching-layer is the geometrical mean of the refractive index of the semiconductor and the ambient medium. Another way to provide a smooth transition of refractive index at the semiconductor surface is to use a layer with a graded refractive index (fig. 1.5 b.). This property is often called the moth's eye effect as it is present on the surface of moth eyes. These lepidoptera eyes are covered with an array of closely packed submicrometric nipples. Due to the subwavelength inter-distance and size of these features compared to incident light wavelengths in the visible range, we can regard the structure as nanoscopic. In the nanoscopic regime we can consider that light waves propagate in the structures without being influenced by each individual feature but rather by the ensemble of those structures. In the case of the moth eye, the nipples have a paraboloid shape and the averaged macroscopic refractive index in which light propagates undergoes a smooth gradient from the tip of the nipples to their basal plane. As a consequence visible light undergoes a smooth transition from the medium to the moth eyes and reflection is negligible. Dewan et al.[91] showed that the moth eyes nipples parabolic shape was optimal for antireflection but other complex structures such as cones are also a suitable alternative. This effect has been exploited for silicon and GaAs solar cells[92–94], but has not yet been studied in photoelectrochemical systems.

If reflection should be avoided at the semiconductor/liquid interface this phenomenon is beneficial at the semiconductor/substrate interface (fig. 1.5 c.). Reflective metal back contact such as aluminium or silver are often used in the PV industry[95]. Recently Dotan et al.[96]

used this approach to obtain resonant total internal reflection in photoanodes composed of an ultra-thin Ti-doped hematite film. The cell they used was V-shaped to achieve an incidence of light above the critical angle corresponding to hematite index of refraction and obtain total internal reflection. The challenging part of this strategy is to shield the reflective metal back reflector from oxidation during hematite processing and cell operation.

We have seen that the control of light reflection at the semiconductor / liquid interface could increase light path in this material, in the best case scenario leading to resonant total internal reflection. Similar effects can also be achieved without implementing additional layers around the photoactive material by a fine control of the photoanode nano- and microstructure. Such fine control allows the implementation of photonic structures that can guide and trap light directly within their bulk. One example of these photonic devices are photonic crystals (fig. 1.5 d.). Such metamaterials are dielectrics with a microstructure that exhibits a long range periodicity, in one or multiple dimensions, at the lengthscale of the light wavelength. When light propagates inside such materials it sees a periodic dielectric constant. Therefore light's wavefunction inside this kind of material can be described by a Bloch wavefunction. At some particular energy light can be confined inside the material in Bloch modes. This kind of light confinement was used already in photoanodes as a well-known process allows to assemble this kind of microstructures easily. This process involves the impregnation by a sol of a 3-dimentional lattice of latex beads obtained by a Langmuir–Blodgett or sedimentation deposition. Pyrolysis of the beads and impregnated sol leads to the formation of an inverse opal photonic crystal structure. Such structures were for example implemented for WO_3 by Chen et al.[97]. They showed that adjusting the slow Bloch modes wavelengths to the optical absorption of WO_3 increased significantly the obtained photocurrents.

Another way to trap light inside a photoactive material is to use a microstructure that can act as a photonic resonator (fig. 1.5 e.). Spheres and cylinders with mesoscopic dimensions compared to incident light wavelengths can act as resonators. Due to the curved surface of the resonator the angle between the propagation direction and the surface can be higher than the critical angle for total internal reflection. In that case the EM field intensity of trapped light is increased upon multiple reflection inside the resonator and constructive interferences. Depending on the relationship between the resonator size and the incoming light wavelength different confined modes can be observed. This effect has been investigated by Grandidier et al.[98,99] to be used with thin film silicon solar cells. A strategy to decrease solar cells cost is to decrease the thickness of the p-i-n silicon heterojunction. To achieve high absorption in

such thin films Grandidier et al. [98,99] proposed to deposit an overlay of optically resonant silica microspheres. Indeed, in addition to light trapping within the resonator bulk, an evanescent EM field is usually leaking from the resonator. They managed to use this leaking field and couple it in the underlying solar cell to improve light absorption.

A wealth of different studies showed that managing the flow of light and electrons inside photoanodes can loosen material requirements. In section 1.1 we have seen that PE water splitting systems have to be low cost in order to compete with existing technologies such as PV-electrolysis. However most of the material required processing steps to implement complex photoanode architectures are expensive. The core topic of this thesis is to study inexpensive self-organization and self-assembly of matter towards the formation of original photoanode architectures and the properties thereof. We will see now in more details the challenges imposed by such an approach and the different solutions discussed throughout this thesis.

1.4   Conclusions and aims of this thesis

To sum up, monoclinic tungsten oxide (mWO$_3$) and hematite have emerged as promising photoanode materials for PE water splitting (section 1.2). These oxides are inexpensive, earth-abundant and gather both a suitable band gap for visible light absorption and a high resistance to photocorrosion. Their major limitation comes from the coupling of a short minority charge carrier diffusion length and a high transparency. Complex material architectures at the nanometer and micrometer scales allow achieving short distances for holes diffusion without compromising light absorption. Since metal oxide photoanodes benefit from the low cost of their constituents, the technique employed to control the photoanode structure should also be inexpensive in order to keep the photoanode cost as low as possible. In addition a successful process for the production of materials for solar energy conversion should also be upscalable. A back-of-the-envelope calculation[17] shows that world energy consumption could be fulfilled by covering an area close to the surface of France with 10% efficient solar panels. Even if such coverage is not achievable in practice, this calculation shows that a production process with a fast output is required if solar energy has to become more than a niche application. Therefore we focused our work on cheap and upscalable processing techniques that would still grant us a high control of the structures morphology.

Well-established micropatterning techniques are usually involving top-down approaches. Inkjet printing for example can write a pattern on a surface directly from a preset design. Photonic devices were implemented with submicrometric resolution[100] but the very slow throughput of this technique in terms of surface area does not make it practical for solar energy applications. Photolithography is another widely used micropatterning method. Direct imprint of light projection through a mask on a photocurable polymer and subsequent etching steps allows to write structures down to the diffraction limit of light (≈ 100 nm). Higher resolutions can be obtained using interferences phenomena but the mask design becomes more complex. This technique requires expensive mask and numerous preparation steps that also make it unpractical for very large scale applications.

The advantage of top-down approaches is the high control they provide towards microstructure design since the desired patterns can be directly printed on surfaces. Nevertheless they are not cost effective for mass production of micro and nanopatterned surfaces. Bottom-up approaches, where matter assembles by itself into the desired structures, offer a cheaper and upscalable alternative. We have already discussed some of those assemblies while reviewing photoanodes architectures. For example the latex beads used to produce photonic crystals photoanodes[101–103] are self-assembling in the opal structure by sedimentation. The latex beads themselves self-organize in spheres with a strongly monomodal distribution by emulsion polymerization[104]? .

In this thesis we will see two different solutions towards the formation of metal oxide photoanodes with original microstructures. The first three following chapters will be focused on the synthesis, photoelectrochemical and optical properties of micrometric and submicrometric oblate spheroids with controlled size distribution. In a first chapter we will study the formation of these structures by using a polymer templated sol-gel process. In a second chapter we investigate the PE water splitting properties of these films. In the third chapter their optical properties will be studied through a simulation model validated experimentally. In that chapter we will see the relationship between the material optical properties and its photoelectrochemical response. The last chapter will detail the results obtained with an alternative self-organization method, namely electrohydrodynamic destabilization.

References

1. ⎘. BP, British Petroleum. Statistical Review of World Energy, June 2014.

2. ⎘. US Public Law. The Energy Policy Act of 1992, October 1992.

3. ⎘. US Departement of Energy, Alternative Fuels Data Center. Fuel Properties Comparison, September 2014.

4. ⎘. S. M. Aceves, J. Martinez-Frias, and O. Garcia-Villazana. Analytical and experimental evaluation of insulated pressure vessels for cryogenic hydrogen storage. *International Journal of Hydrogen Energy*, 25(11):1075–1085, November 2000.

5. ⎘. Salvador M. Aceves, Gene D. Berry, Joel Martinez-Frias, and Francisco Espinosa-Loza. Vehicular storage of hydrogen in insulated pressure vessels. *International Journal of Hydrogen Energy*, 31(15):2274–2283, December 2006.

6. ⎘. Salvador M. Aceves, Francisco Espinosa-Loza, Elias Ledesma-Orozco, Timothy O. Ross, Andrew H. Weisberg, Tobias C. Brunner, and Oliver Kircher. High-density automotive hydrogen storage with cryogenic capable pressure vessels. *International Journal of Hydrogen Energy*, 35(3):1219–1226, February 2010.

7. ⎘. National Organisation Hydrogen and Fuel Cell Technology. News release: 50 hydrogen refuelling stations for Germany - locations confirmed, July 2014.

8. ⎘. PostBus Switzerland Ltd. The first Swiss hydrogen filling station, 2012.

9. ⎘. NEST. Mobility Demonstrator, Mobility of the Future, 2014.

10. ⎘. California Energy Commission. California Investing Nearly $50 Million in Hydrogen Refueling Stations, May 2014.

11. ⎘. The Japan Times. Japan gets its first commercial hydrogen station for vehicles, July 2014.

12. ⎘. WWF, Iceland Nature Conservation Association. Transition to a Hydrogen Economy - a strategy for sustainable development in Iceland, 2001.

13. ⎘. The New York Times, Energy and Environment. Sinking Finances Throw Iceland's 'Hydrogen-Based Economy' Into the Freezer, 2009.

14. ⬓. Daimler AG. The strategic cooperation between Daimler and the Renault-Nissan alliance forms agreement with Ford to accelerate commercialization of fuel cell electric vehicle technology, January 2013.

15. ⬓. Toyota website. Introducing Toyota's Fuel Cell Technology, 2014.

16. ⬓. T. Jesper Jacobsson, Viktor Fjallstrom, Marika Edoff, and Tomas Edvinsson. Sustainable solar hydrogen production: from photoelectrochemical cells to PV-electrolyzers and back again. *Energy Environ. Sci.*, 7:2056–2070, April 2014.

17. ⬓. Roel Krol and Michael Grätzel. Principles of Photoelectrochemical Cells. In Springer, editor, *Photoelectrochemical Hydrogen Production*, volume 102 of *Electronic Materials: Science & Technology*, pages 13–67. Springer US, 2012. ISBN 978-1-4614-1379-0.

18. ⬓. T. Bak, J. Nowotny, M. Rekas, and C. C. Sorrell. Photo-electrochemical hydrogen generation from water using solar energy. Materials-related aspects. *International Journal of Hydrogen Energy*, 27(10):PII S0360–3199(02)00022–8, October 2002.

19. ⬓. W. J. Chun, A. Ishikawa, H. Fujisawa, T. Takata, J. N. Kondo, M. Hara, M. Kawai, Y. Matsumoto, and K. Domen. Conduction and valence band positions of Ta_2O_5, TaON, and Ta_3N_5 by UPS and electrochemical methods. *Journal of Physical Chemistry B*, 107 (8):1798–1803, February 2003.

20. ⬓. C. G. Van de Walle and J. Neugebauer. Universal alignment of hydrogen levels in semiconductors, insulators and solutions. *Nature*, 423(6940):626–628, June 2003.

21. ⬓. Kaining Ding, Bin Chen, Yulu Li, Yongfan Zhang, and Zhongfang Chen. Comparative density functional theory study on the electronic and optical properties of $BiMO_4$ (M = V, Nb, Ta). *Journal of Materials Chemistry A*, 2(22):8294–8303, 2014.

22. ⬓. Michael J. Kenney, Ming Gong, Yanguang Li, Justin Z. Wu, Ju Feng, Mario Lanza, and Hongjie Dai. High-Performance Silicon Photoanodes Passivated with Ultrathin Nickel Films for Water Oxidation. *Science*, 342(6160):836–840, November 2013.

23. ⬓. Shu Hu, Matthew R. Shaner, Joseph A. Beardslee, Michael Lichterman, Bruce S. Brunschwig, and Nathan S. Lewis. Amorphous TiO_2 coatings stabilize Si, GaAs, and GaP photoanodes for efficient water oxidation. *Science*, 344(6187):1005–1009, May 2014.

24. ⍈. A. B. Murphy, P. R. F. Barnes, L. K. Randeniya, I. C. Plumb, I. E. Grey, M. D. Horne, and J. A. Glasscock. Efficiency of solar water splitting using semiconductor electrodes. *International Journal of Hydrogen Energy*, 31(14):1999–2017, November 2006.

25. ⍈. G. Hitoki, A. Ishikawa, T. Takata, J. N. Kondo, M. Hara, and K. Domen. Ta$_3$N$_5$ as a novel visible light-driven photocatalyst (lambda < 600 nm). *Chemistry Letters*, (7): 736–737, July 2002.

26. ⍈. G. Hitoki, T. Takata, J. N. Kondo, M. Hara, H. Kobayashi, and K. Domen. An oxynitride, TaON, as an efficient water oxidation photocatalyst under visible light irradiation (lambda ≤ 500 nm). *Chemical Communications*, (16):1698–1699, August 2002.

27. ⍈. M. Hara, G. Hitoki, T. Takata, J. N. Kondo, H. Kobayashi, and K. Domen. TaON and Ta$_3$N$_5$ as new visible light driven photocatalysts. *Catalysis Today*, 78(1-4):PII S0920– 5861(02)00354–1, February 2003.

28. ⍈. Masanobu Higashi, Kazunari Domen, and Ryu Abe. Fabrication of efficient TaON and Ta$_3$N$_5$ photoanodes for water splitting under visible light irradiation. *Energy & Environmental Science*, 4(10):4138–4147, October 2011.

29. ⍈. A. Fujishima and K. Honda. Electrochemical Photolysis of Water At A Semiconductor Electrode. *Nature*, 238(5358):37–38, 1972.

30. ⍈. R. Asahi, T. Morikawa, T. Ohwaki, K. Aoki, and Y. Taga. Visible-light photocatalysis in nitrogen-doped titanium oxides. *Science*, 293(5528):269–271, July 2001.

31. ⍈. A. Monnier and J. Augustynski. Photoelectrolysis of Water - Photoresponses of Nickel, Chromium and Zinc-doped Polycrystalline TiO$_2$ Electrodes. *Journal of the Electrochemical Society*, 127(7):1576–1579, 1980.

32. ⍈. S. U. M. Khan, M. Al-Shahry, and W. B. Ingler. Efficient photochemical water splitting by a chemically modified n-TiO$_2$. *Science*, 297(5590):2243–2245, September 2002.

33. ⍈. T. Umebayashi, T. Yamaki, H. Itoh, and K. Asai. Band gap narrowing of titanium dioxide by sulfur doping. *Applied Physics Letters*, 81(3):454–456, July 2002.

34. ⌁. Na Lu, Xie Quan, JingYuan Li, Shuo Chen, HongTao Yu, and GuoHua Chen. Fabrication of boron-doped TiO2 nanotube array electrode and investigation of its photoelectrochemical capability. *Journal of Physical Chemistry C*, 111(32):11836–11842, August 2007.

35. ⌁. S. Anderson, E. C. Constable, M. P. Dareedwards, J. B. Goodenough, A. Hamnett, K. R. Seddon, and R. D. Wright. Chemical Modification of A Titanium(IV) Oxide Electrode To Give Stable Dye Sensitization Without A Supersensitizer. *Nature*, 280 (5723):571–573, 1979.

36. ⌁. Zhebo Chen, Thomas F. Jaramillo, Todd G. Deutsch, Alan Kleiman-Shwarsctein, Arnold J. Forman, Nicolas Gaillard, Roxanne Garland, Kazuhiro Takanabe, Clemens Heske, Mahendra Sunkara, Eric W. McFarland, Kazunari Domen, Eric L. Miller, John A. Turner, and Huyen N. Dinh. Accelerating materials development for photoelectrochemical hydrogen production: Standards for methods, definitions, and reporting protocols. *Journal of Materials Research*, 25(1):3–16, January 2010.

37. ⌁. J. H. Kennedy and K. W. Frese. Photo-oxidation of Water At α-Fe$_2$O$_3$ Electrodes. *Journal of the Electrochemical Society*, 125(5):709–714, 1978.

38. ⌁. L. A. Marusak, R. Messier, and W. B. White. Optical-absorption Spectrum of Hematite, α-Fe$_2$O$_3$ Near IR To UV. *Journal of Physics and Chemistry of Solids*, 41(9): 981–984, 1980.

39. ⌁. Ilkay Cesar, Kevin Sivula, Andreas Kay, Radek Zboril, and Michael Grätzel. Influence of Feature Size, Film Thickness, and Silicon Doping on the Performance of Nanostructured Hematite Photoanodes for Solar Water Splitting. *Journal of Physical Chemistry C*, 113(2):772–782, January 2009.

40. ⌁. Jen-Chun Chou, Szu-An Lin, Chi-Young Lee, and Jon-Yiew Gan. Effect of bulk doping and surface-trapped states on water splitting with hematite photoanodes. *Journal of Materials Chemistry A*, 1(19):5908–5914, 2013.

41. ⌁. Yelin Hu, Debajeet K. Bora, Florent Boudoire, Florian Haussler, Michael Grätzel, Edwin C. Constable, and Artur Braun. A dip coating process for large area silicon-doped high performance hematite photoanodes. *Journal of Renewable and Sustainable Energy*, 5(4):043109, 2013.

42. ⛶. Florian Le Formal, Kevin Sivula, and Michael Grätzel. The Transient Photocurrent and Photovoltage Behavior of a Hematite Photoanode under Working Conditions and the Influence of Surface Treatments. *Journal of Physical Chemistry C*, 116(51):26707–26720, December 2012.

43. ⛶. R. A. Fredlein and A. J. Bard. Semiconductor Electrodes .21. Characterization and Behavior of N-type Fe_2O_3 Electrodes In Acetonitrile Solutions. *Journal of the Electro-chemical Society*, 126(11):1892–1898, 1979.

44. ⛶. M. P. Dare-Edwards, J. B. Goodenough, A. Hamnett, and P. R. Trevellick. Electrochemistry and Photoelectrochemistry of Iron(III) Oxide. *Journal of the Chemical Society-faraday Transactions I*, 79:2027–2041, 1983.

45. ⛶. Hen Dotan, Kevin Sivula, Michael Grätzel, Avner Rothschild, and Scott C. Warren. Probing the photoelectrochemical properties of hematite (α-Fe_2O_3) electrodes using hydrogen peroxide as a hole scavenger. *Energy & Environmental Science*, 4(3):958–964, March 2011.

46. ⛶. Benjamin Klahr, Sixto Gimenez, Francisco Fabregat-Santiago, Thomas Hamann, and Juan Bisquert. Water Oxidation at Hematite Photoelectrodes: The Role of Surface States. *Journal of the American Chemical Society*, 134(9):4294–4302, March 2012.

47. ⛶. Laurence M. Peter, K. G. Upul Wijayantha, and Asif A. Tahir. Kinetics of light-driven oxygen evolution at α-Fe_2O_3 electrodes. *Faraday Discussions*, 155:309–322, 2012.

48. ⛶. Krisztina Gajda-Schrantz, Simon Tymen, Florent Boudoire, Rita Toth, Debajeet K. Bora, Wolfram Calvet, Michael Gratzel, Edwin C. Constable, and Artur Braun. Formation of an electron hole doped film in the alpha-Fe(2)O(3) photoanode upon electrochemical oxidation. *Physical chemistry chemical physics : PCCP*, 15(5):1443–51, February 2013.

49. ⛶. Florian Le Formal, Nicolas Tetreault, Maurin Cornuz, Thomas Moehl, Michael Grätzel, and Kevin Sivula. Passivating surface states on water splitting hematite photoanodes with alumina overlayers. *Chemical Science*, 2(4):737–743, 2011.

50. ⛶. Monica Barroso, Camilo A. Mesa, Stephanie R. Pendlebury, Alexander J. Cowan, Takashi Hisatomi, Kevin Sivula, Michael Grätzel, David R. Klug, and James R. Durrant.

Dynamics of photogenerated holes in surface modified α-Fe$_2$O$_3$ photoanodes for solar water splitting. *Proceedings of the National Academy of Sciences of the United States of America*, 109(39):15640–15645, September 2012.

51. ⎗. Diane K. Zhong, Jianwei Sun, Hiroki Inumaru, and Daniel R. Gamelin. Solar Water Oxidation by Composite Catalyst/α-Fe$_2$O$_3$ Photoanodes. *Journal of the American Chemical Society*, 131(17):6086–6087, May 2009.

52. ⎗. Alan Kleiman-Shwarsctein, Yong-Sheng Hu, Galen D. Stucky, and Eric W. McFarland. NiFe-oxide electrocatalysts for the oxygen evolution reaction on Ti doped hematite photoelectrodes. *Electrochemistry Communications*, 11(6):1150–1153, June 2009.

53. ⎗. Diane K. Zhong, Maurin Cornuz, Kevin Sivula, Michael Grätzel, and Daniel R. Gamelin. Photo-assisted electrodeposition of cobalt-phosphate (Co-Pi) catalyst on hematite photoanodes for solar water oxidation. *Energy & Environmental Science*, 4 (5):1759–1764, May 2011.

54. ⎗. Benjamin Klahr, Sixto Gimenez, Francisco Fabregat-Santiago, Juan Bisquert, and Thomas W. Hamann. Photoelectrochemical and Impedance Spectroscopic Investigation of Water Oxidation with "Co-Pi"-Coated Hematite Electrodes. *Journal of the American Chemical Society*, 134(40):16693–16700, October 2012.

55. ⎗. Artur Braun, Kevin Sivula, Debajeet K. Bora, Junfa Zhu, Liang Zhang, Michael Grätzel, Jinghua Guo, and Edwin C. Constable. Direct Observation of Two Electron Holes in a Hematite Photoanode during Photoelectrochemical Water Splitting. *Journal of Physical Chemistry C*, 116(32):16870–16875, August 2012.

56. ⎗. M. A. Butler, R. D. Nasby, and R. K. Quinn. Tungsten Trioxide As An Electrode For Photoelectrolysis of Water. *Solid State Communications*, 19(10):1011–1014, 1976.

57. ⎗. A. Kudo, K. Ueda, H. Kato, and I. Mikami. Photocatalytic O$_2$ evolution under visible light irradiation on BiVO$_4$ in aqueous AgNO$_3$ solution. *Catalysis Letters*, 53(3-4): 229–230, 1998.

58. ⎗. Hyun S. Park, Kyoung Eun Kweon, Heechang Ye, Eunsu Paek, Gyeong S. Hwang, and Allen J. Bard. Factors in the Metal Doping of BiVO$_4$ for Improved Photoelectrocatalytic Activity as Studied by Scanning Electrochemical Microscopy and First-Principles

Density-Functional Calculation. *Journal of Physical Chemistry C*, 115(36):17870–17879, September 2011.

59. ⌕. Sean P. Berglund, Alexander J. E. Rettie, Son Hoang, and C. Buddie Mullins. Incorporation of Mo and W into nanostructured $BiVO_4$ films for efficient photoelectrochemical water oxidation. *Physical Chemistry Chemical Physics*, 14(19):7065–7075, 2012.

60. ⌕. Fatwa F. Abdi, Lihao Han, Arno H. M. Smets, Miro Zeman, Bernard Dam, and Roel van de Krol. Efficient solar water splitting by enhanced charge separation in a bismuth vanadate-silicon tandem photoelectrode. *Nature Communications*, 4:2195, July 2013.

61. ⌕. Michael Woodhouse and B. A. Parkinson. Combinatorial discovery and optimization of a complex oxide with water photoelectrolysis activity. *Chemistry of Materials*, 20(7): 2495–2502, April 2008.

62. ⌕. Jordan E. Katz, Todd R. Gingrich, Elizabeth A. Santori, and Nathan S. Lewis. Combinatorial synthesis and high-throughput photopotential and photocurrent screening of mixed-metal oxides for photoelectrochemical water splitting. *Energy & Environmental Science*, 2(1):103–112, 2009.

63. ⌕. Takeo Arai, Yoshinari Konishi, Yasukazu Iwasaki, Hideki Sugihara, and Kazuhiro Sayama. High-throughput screening using porous photoelectrode for the development of visible-light-responsive semiconductors. *Journal of Combinatorial Chemistry*, 9(4): 574–581, July 2007.

64. ⌕. B. M. Kayes, H. A. Atwater, and N. S. Lewis. Comparison of the device physics principles of planar and radial p-n junction nanorod solar cells. *Journal of Applied Physics*, 97(11):114302, June 2005.

65. ⌕. G. A. Somorjai. The Flexible Surface - Correlation Between Reactivity and Restructuring Ability. *Langmuir*, 7(12):3176–3182, December 1991.

66. ⌕. Andreas Kay, Ilkay Cesar, and Michael Grätzel. New benchmark for water photooxidation by nanostructured α-Fe_2O_3 films. *Journal of the American Chemical Society*, 128 (49):15714–15721, December 2006.

67. ⌐. T. Lindgren, H. L. Wang, N. Beermann, L. Vayssieres, A. Hagfeldt, and S. E. Lindquist. Aqueous photoelectrochemistry of hematite nanorod array. *Solar Energy Materials and Solar Cells*, 71(2):231–243, February 2002.

68. ⌐. Susanta K. Mohapatra, Shiny E. John, Subarna Banerjee, and Mano Misra. Water Photooxidation by Smooth and Ultrathin α-Fe_2O_3 Nanotube Arrays. *Chemistry of Materials*, 21(14):3048–3055, July 2009.

69. ⌐. Debajeet K. Bora, Artur Braun, Rolf Erni, Giuseppino Fortunato, Thomas Graule, and Edwin C. Constable. Hydrothermal Treatment of a Hematite Film Leads to Highly Oriented Faceted Nanostructures with Enhanced Photocurrents. *Chemistry of Materials*, 23(8):2051–2061, April 2011.

70. ⌐. C. Santato, M. Odziemkowski, M. Ulmann, and J. Augustynski. Crystallographically oriented Mesoporous WO_3 films: Synthesis, characterization, and applications. *Journal of the American Chemical Society*, 123(43):10639–10649, October 2001.

71. ⌐. C. Santato, M. Ulmann, and J. Augustynski. Enhanced visible light conversion efficiency using nanocrystalline WO_3 films. *Advanced Materials*, 13(7):511–514, April 2011.

72. ⌐. C. Santato, M. Ulmann, and J. Augustynski. Photoelectrochemical properties of nanostructured tungsten trioxide films. *Journal of Physical Chemistry B*, 105(5):936–940, February 2001.

73. ⌐. Jinzhan Su, Xinjian Feng, Jennifer D. Sloppy, Liejin Guo, and Craig A. Grimes. Vertically Aligned WO_3 Nanowire Arrays Grown Directly on Transparent Conducting Oxide Coated Glass: Synthesis and Photoelectrochemical Properties. *Nano Letters*, 11(1):203–208, January 2011.

74. ⌐. Renata Solarska, Rafal Jurczakowski, and Jan Augustynski. A highly stable, efficient visible-light driven water photoelectrolysis system using a nanocrystalline WO_3 photoanode and a methane sulfonic acid electrolyte. *Nanoscale*, 4(5):1553–1556, 2012.

75. ⌐. Michael G. Walter, Emily L. Warren, James R. McKone, Shannon W. Boettcher, Qixi Mi, Elizabeth A. Santori, and Nathan S. Lewis. Solar Water Splitting Cells. *Chemical Reviews*, 110(11):6446–6473, November 2010.

76. ⌕. M. X. Tan, C. N. Kenyon, and N. S. Lewis. Experimental-measurement of Quasi-fermi Levels At An Illuminated Semiconductor/liquid Contact. *Journal of Physical Chemistry*, 98(19):4959–4962, May 1994.

77. ⌕. C. N. Kenyon, M. X. Tan, O. Kruger, and N. S. Lewis. Behavior of Si photoelectrodes under high level injection conditions .3. Transient and steady-state measurements of the quasi-Fermi levels at Si/CH_3OH contacts. *Journal of Physical Chemistry B*, 101(15): 2850–2860, April 1997.

78. ⌕. O. Kruger, C. N. Kenyon, M. X. Tan, and N. S. Lewis. Behavior of Si photoelectrodes under high level injection conditions .2. Experimental measurements and digital simulations of the behavior of quasi-Fermi levels under illumination and applied bias. *Journal of Physical Chemistry B*, 101(15):2840–2849, April 1997.

79. ⌕. M. X. Tan, C. N. Kenyon, O. Kruger, and N. S. Lewis. Behavior of Si photoelectrodes under high level injection conditions .1. Steady-state current-voltage properties and quasi-Fermi level positions under illumination. *Journal of Physical Chemistry B*, 101 (15):2830–2839, April 1997.

80. ⌕. G. Hodes, L. Thompson, J. DuBow, and K. Rajeshwar. Heterojunction silicon/indium tin oxide photoelectrodes: development of stable systems in aqueous electrolytes and their applicability to solar energy conversion and storage. *Journal of the American Chemical Society*, 105(3):324–330, 1983.

81. ⌕. Yun Jeong Hwang, Akram Boukai, and Peidong Yang. High Density $n-Si/n-TiO_2$ Core/Shell Nanowire Arrays with Enhanced Photoactivity. *Nano Letters*, 9(1):410–415, January 2009.

82. ⌕. Roel van de Krol and Yongqi Liang. An $n-Si/n-Fe_2O_3$ Heterojunction Tandem Photoanode for Solar Water Splitting. *Chimia*, 67(3):168–171, 2013.

83. ⌕. Kevin Sivula, Florian Le Formal, and Michael Grätzel. $WO_3-Fe_2O_3$ Photoanodes for Water Splitting: A Host Scaffold, Guest Absorber Approach. *Chemistry of Materials*, 21(13):2862–2867, July 2009.

84. ⌕. Jinzhan Su, Liejin Guo, Ningzhong Bao, and Craig A. Grimes. Nanostructured $WO_3/BiVO_4$ Heterojunction Films for Efficient Photoelectrochemical Water Splitting. *Nano Letters*, 11(5):1928–1933, May 2011.

85. ⬀. Aiming Mao, Jung Kyu Kim, Kahee Shin, Dong Hwan Wang, Pill J. Yoo, Gui Young Han, and Jong Hyeok Park. Hematite modified tungsten trioxide nanoparticle photoanode for solar water oxidation. *Journal of Power Sources*, 210:32–37, July 2012.

86. ⬀. Scott C. Warren and Elijah Thimsen. Plasmonic solar water splitting. *Energy & Environmental Science*, 5(1):5133–5146, January 2012.

87. ⬀. Renata Solarska, Agata Krolikowska, and Jan Augustynski. Silver Nanoparticle Induced Photocurrent Enhancement at WO_3 Photoanodes. *Angewandte Chemie-international Edition*, 49(43):7980–7983, 2010.

88. ⬀. Elijah Thimsen, Florian Le Formal, Michael Gräetzel, and Scott C. Warren. Influence of Plasmonic Au Nanoparticles on the Photoactivity of Fe_2O_3 Electrodes for Water Splitting. *Nano Letters*, 11(1):35–43, January 2011.

89. ⬀. Isabel Thomann, Blaise A. Pinaud, Zhebo Chen, Bruce M. Clemens, Thomas F. Jaramillo, and Mark L. Brongersma. Plasmon Enhanced Solar-to-Fuel Energy Conversion. *Nano Letters*, 11(8):3440–3446, August 2011.

90. ⬀. Hanwei Gao, Chong Liu, Hoon Eui Jeong, and Peidong Yang. Plasmon-Enhanced Photocatalytic Activity of Iron Oxide on Gold Nanopillars. *Acs Nano*, 6(1):234–240, January 2012.

91. ⬀. Rahul Dewan, Stefan Fischer, V. Benno Meyer-Rochow, Yasemin Oezdemir, Saeed Hamraz, and Dietmar Knipp. Studying nanostructured nipple arrays of moth eye facets helps to design better thin film solar cells. *Bioinspiration & Biomimetics*, 7(1):016003, March 2012.

92. ⬀. Yi-Fan Huang, Surojit Chattopadhyay, Yi-Jun Jen, Cheng-Yu Peng, Tze-An Liu, Yu-Kuei Hsu, Ci-Ling Pan, Hung-Chun Lo, Chih-Hsun Hsu, Yuan-Huei Chang, Chih-Shan Lee, Kuei-Hsien Chen, and Li-Chyong Chen. Improved broadband and quasi-omnidirectional anti-reflection properties with biomimetic silicon nanostructures. *Nature Nanotechnology*, 2(12):770–774, December 2007.

93. ⬀. Young Min Song, Si Young Bae, Jae Su Yu, and Yong Tak Lee. Closely packed and aspect-ratio-controlled antireflection subwavelength gratings on GaAs using a lenslike shape transfer. *Optics Letters*, 34(11):1702–1704, June 2009.

94. ⎘. Z. N. Yu, H. Gao, W. Wu, H. X. Ge, and S. Y. Chou. Fabrication of large area subwavelength antireflection structures on Si using trilayer resist nanoimprint lithography and liftoff. *Journal of Vacuum Science & Technology B*, 21(6):2874–2877, November 2003.

95. ⎘. J. Muller, B. Rech, J. Springer, and M. Vanecek. TCO and light trapping in silicon thin film solar cells. *Solar Energy*, 77(6):917–930, 2004.

96. ⎘. Hen Dotan, Ofer Kfir, Elad Sharlin, Oshri Blank, Moran Gross, Irina Dumchin, Guy Ankonina, and Avner Rothschild. Resonant light trapping in ultrathin films for water splitting. *Nature Materials*, 12(2):158–164, February 2013.

97. ⎘. Xiaoqing Chen, Jinhua Ye, Shuxin Ouyang, Tetsuya Kako, Zhaosheng Li, and Zhigang Zou. Enhanced Incident Photon-to-Electron Conversion Efficiency of Tungsten Trioxide Photoanodes Based on 3D-Photonic Crystal Design. *Acs Nano*, 5(6):4310–4318, June 2011.

98. ⎘. Jonathan Grandidier, Dennis M. Callahan, Jeremy N. Munday, and Harry A. Atwater. Light Absorption Enhancement in Thin-Film Solar Cells Using Whispering Gallery Modes in Dielectric Nanospheres. *Advanced Materials*, 23(10):1272–1276, March 2011.

99. ⎘. Jonathan Grandidier, Raymond A. Weitekamp, Michael G. Deceglie, Dennis M. Callahan, Corsin Battaglia, Colton R. Bukowsky, Christophe Ballif, Robert H. Grubbs, and Harry A. Atwater. Solar cell efficiency enhancement via light trapping in printable resonant dielectric nanosphere arrays. *Physica Status Solidi A-applications and Materials Science*, 210(2):255–260, February 2013.

100. ⎘. K. K. B. Hon, L. Li, and I. M. Hutchings. Direct writing technology-Advances and developments. *Cirp Annals-manufacturing Technology*, 57(2):601–620, 2008.

101. ⎘. Xiaoqing Chen, Zhaosheng Li, Jinhua Ye, and Zhigang Zou. Forced Impregnation Approach to Fabrication of Large-Area, Three-Dimensionally Ordered Macroporous Metal Oxides. *Chemistry of Materials*, 22(12):3583–3585, June 2010.

102. ⎘. Siva Krishna Karuturi, Chuanwei Cheng, Lijun Liu, Liap Tat Su, Hong Jin Fan, and Alfred Iing Yoong Tok. Inverse opals coupled with nanowires as photoelectrochemical anode. *Nano Energy*, 1(2):322–327, March 2012.

103. ⬏. Siva Krishna Karuturi, Jingshan Luo, Chuanwei Cheng, Lijun Liu, Liap Tat Su, Alfred Iing Yoong Tok, and Hong Jin Fan. A Novel Photoanode with Three-Dimensionally, Hierarchically Ordered Nanobushes for Highly Efficient Photoelectrochemical Cells. *Advanced Materials*, 24(30):4157–4162, August 2012.

104. ⬏. J. Ugelstad, K. H. Kaggerud, F. K. Hansen, and A. Berge. Absorption of Low-molecular Weight Compounds In Aqueous Dispersions of Polymer-oligomer Particles .2. Step Swelling Process of Polymer Particles Giving An Enormous Increase In Absorption Capacity. *Makromolekulare Chemie-macromolecular Chemistry and Physics*, 180(3):737–744, 1979.

Chapter 2

Self-assembly of tungsten oxide microspheroids

A wealth of complex microstructures can be obtained by using polymers. These chain-like molecules are composed of repeating units, formed from monomers, that bond to form chains that can extend to several thousands of these units. A polymer, or a polymer blend, can self-assemble from monomers or from crosslinking between multiple polymer chains into architectures that can be controlled by processing parameters. These structures can be "frozen" upon drying or precipitation of the polymer. A well-established strategy to obtain complex microstructures is for example polymer blend demixing. In the frame of this thesis we are interested in converting these polymer structures into metal oxide structures. This can be achieved by loading the polymer with a metal oxide precursor, before or after the polymer self-assembly, and then heating up the system at a temperature where the polymer will decompose and evaporate while the metal oxide will be formed from its precursors. This kind of polymer templated technique has been used already, in the production of high porosity metal oxides photoanodes[1–3] and more complex architectures such as inverse opals photonic crystals[4]. In this chapter we will discover an original approach involving the use of a polyelectrolyte and a tungsten salt in an aqueous solution containing ammonia (NH_3). Upon thin film casting and subsequent pyrolysis we will see that an original microstructure can be obtained, composed of micrometric oblate spheroids of monoclinic tungsten trioxide. The focus of this chapter is to unravel the phenomena that lead to these oxide spheroids self-assembly and to identify the parameters of influence on the microspheroids size and shape.

2.1 Introduction

I want to use polymer assemblies that can act as template for novel metal oxides thin films microstructures. Our goal is to obtain a strong interaction between a metal salt precursor and the polymer in order to enclose the metal salt inside polymeric structures. In order to keep this process inexpensive I chose water as medium for this self-assembly process. Hence I had to use compounds that are highly soluble in water to obtain homogeneous solutions, suited for casting on the FTO glass substrates used to produce the photoanode assembly. I used Ammonium Meta-Tungstate (AMT) as metal salt precursor for mWO_3. This specie is more soluble in water for a wider range of pHs than alternative salts like Ammonium Para-Tungstate (APT), tungstic acid (H_2WO_4) and tungsten chloride (WCl_6). The polymer I chose for this study was a polyelectrolyte, Poly(4-styrenesulfonic acid) (PSS). Polyelectrolytes are polymers bearing ionizable groups. These groups can hydrolyse, making polyelectrolytes soluble in water. In addition PSS is known for its ability to self-assemble in solution in layer-by-layer self-assembly processes and into nanometric domains[5–8].

I found that addition of ammonium ions to a water based solution containing PSS and AMT was leading upon casting to a monolayer of tungsten rich spheroidal domains enclosed in a polymer matrix. Upon pyrolysis these domains become mWO_3 oblate tungsten spheroids while the polymer is pyrolysed. I propose here to explain this self-assembly process based on optical measurements realized on solutions, during spin coating and after spin coating the films. In particular I will emphasize the influence of ammonia (NH_3) concentration, which triggers the spheroids formation upon casting.

2.2 Materials and methods

2.2.1 mWO_3 microspheroids synthesis route

The mWO_3 thin film composed of microspheroids is casted from an aqueous solution containing PSS, AMT and NH_3. In the present study various amounts of ammonia have been investigated with concentrations ranging between 0 mol/L and 4.5 mol/L. The concentrations of AMT (0.5 mol/L) and PSS (0.2 mol/L) were kept constant. These solutions are prepared in 3 steps. First an aqueous ammonia solution (5 mol/L, Sigma-Aldrich) is diluted in Deionized (DI) water in

order to obtain the desired ammonia concentration. Then AMT powder (Sigma-Aldrich) is added to the solution which is stirred until full dissolution. A PSS aqueous solution is then added to the solution and the mixture is further stirred for 5 minutes.
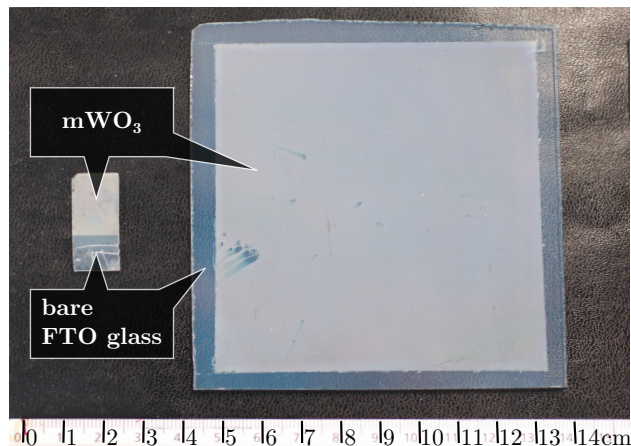

Figure 2.1: 1.5×1.5 cm and 10×10 cm photoanodes obtained by spin coating at 3000 rpm and pyrolysis at 500°C of a PSS (0.2 mol/L) / AMT (0.2 mol/L) / NH_3 (0.2 mol/L) solution on FTO glass. These photoanodes are composed of a monolayer of micrometric mWO_3 spheroids.

The final solution containing 4.5 mol/L of NH_3 was spin coated on FTO glass slides of 1.5×2.5 cm (fluorinated tin-oxide coated aluminoborosilicate glass, 10 $\Omega.sq^{-1}$ from Solaronix) using a Primus STT15 (ATM group) spin coater. Different spin coating speeds were investigated, from 1000 to 6000 rpm, with an acceleration of 3000 rpm/s and a holding time of 60 seconds. The resulting films were then pyrolysed at 500°C for 2 hour, with a heating ramp of 5°C/min. This whole synthesis is simple and easily upscalable. The samples used for characterization have a size of 1.5×2.5 cm, but photoanodes with dimensions close to 10×10 cm could also be obtained with the same synthesis process (fig. 2.1).

2.2.2 Scanning X-ray transmission microscopy

Scanning Transmition X-ray Microscopy (STXM) was used in order to probe the chemical composition of the different domains obtained in thin films upon casting of PSS / AMT / NH_3 solutions. This spectroscopy technique allows to record X-ray absorption spectra of small areas with nanometric dimensions. By scanning a sample surface, a mapping of the sample chemical composition can be obtained with a resolution at the nanoscale. This experiment was realized at Helmholtz Zentrum's Bessy II synchrotron in Berlin, beamline U41-FSGM,

end station U41-TXM. The samples were prepared by spin coating of PSS / AMT / NH_3 solutions at the surface of silicon nitride (Si_3N_4) windows, 200 nm thick, from SPI Supplies.

2.2.3 Conductometric and PH-metric titration

I realized titration experiments in order to understand how the compounds in the PSS / AMT / NH_3 solutions react with each other's. Titrations are usually performed by preparing a first solution, the analyte, in which a second solution is poured, the titrant. The variations in conductivity of the analyte with titrant addition are proportional to addition and/or consumption of ions and give quantitative information on the chemical reaction between the titrant and the analyte. The variations of pH are related to the concentration of hydronium ions in solution, recorded through variations of surface potential when ions adsorb at the electrode surface, according to the relation: pH = -log($[H_3O^+]$). An increase of the volume of solution occurs during titration, leading to a dilution of the analyte. This dilution of the analyte can shift its chemicals concentrations to a range where no structures form upon casting and where the chemical reactions are possibly different from the one encountered in the solution used for spin coating. To avoid this issue it was necessary to prepare a large number of solutions with fixed concentration of PSS and AMT and different concentrations of NH_3.

2.2.4 Optical measurements: dynamic light scattering, in-situ interferometry and static light scattering

In order to study the formation of structures in solution, during and after casting, optical measurements were performed. Dynamic Light Scattering (DLS) proved to be a useful technique for the study of solutions. DLS relies on the fact that particles in solution scatter light in all directions. These multiple scattered light fields interfere with each other leading to a speckle pattern that can be recorded by a Charge-Coupled Device (CCD) camera, with one picture each $\delta t \approx 1$ µs. Each snapshot is correlated to the first snapshot (t = 0) and a correlation coefficient is calculated. This correlation coefficient is comprised between 0 and 1 and represents the extent of change of the speckle pattern over time. The evolution of the correlation coefficient over time is called a correlogram and constitutes the raw data obtained from the DLS instrument. The correlation coefficient evolution over time (C(t)) can be modeled by a sum of exponential decays:

$$C(t) = \sum_{i=1}^{n} A_i \, \exp(-\Gamma_i \, t) \tag{2.1}$$

Where each time constant (Γ_i) correspond to a diffusion coefficient (D_i) in solution:

$$D_i = \frac{\Gamma_i}{q^2} \tag{2.2}$$

$$q = \frac{4\,\pi\,n}{\lambda} \, \sin\left(\frac{\theta}{2}\right)$$

n : particle refractive index

θ : laser angle of incidence

λ : laser light wavelength

And each diffusion coefficient (D_i) relates to a radius of gyration (R_i) through the Stokes-Einstein formula:

$$R_i = \frac{k\,T}{6\,\pi\,\eta\,D_i} \tag{2.3}$$

k : Boltzmann's constant

T : temperature

η : medium dynamic viscosity

I also investigated in-situ interferometry during spin coating. In that case sapphire glass slides, from Stettler sapphire AG, were used as substrates in order to avoid effects linked to the FTO glass roughness. This technique allows to follow interference variations over time, occurring during spin coating due to the decrease of film thickness (fig. 2.2). This method was also used in the literature to monitor other structural changes, such as phase separation[9]. In these experiments an increase in scattering due to the formation of micrometric domains during spin coating leads to a decrease in the reflected intensity over time.
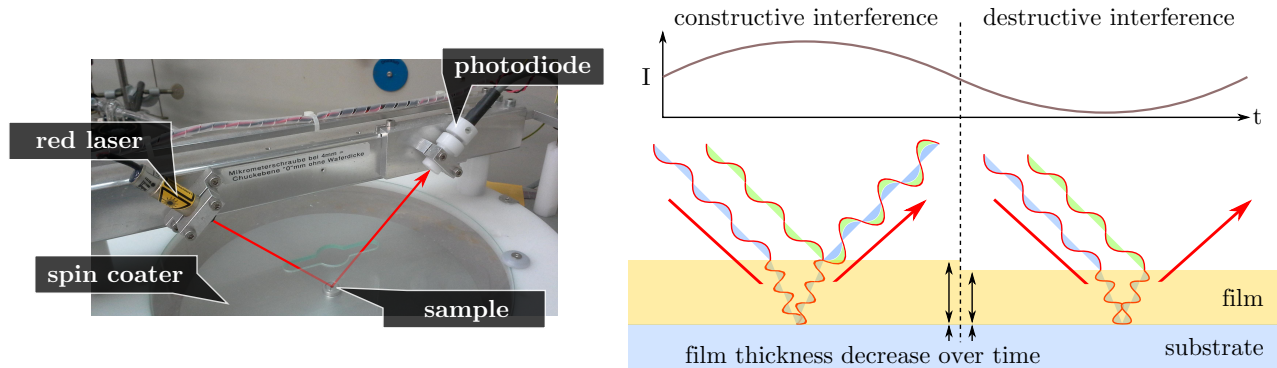
Figure 2.2: In-situ interferometry during spin coating. Left: Experimental setup. Right: Schematic representation of interference phenomena recorded during spin coating.

Finally angle resolved Static Light Scattering (SLS) was used on films after their spin coating in order to confirm the results obtained with in-situ interferometry. These experiments were performed on the same films used in the interferometry study, which were coated on sapphire glass. In this experiment a monochromatic laser is pointed orthogonally to the sample surface while recording the scattered intensity with a detector rotating around the sample (fig. 2.3).
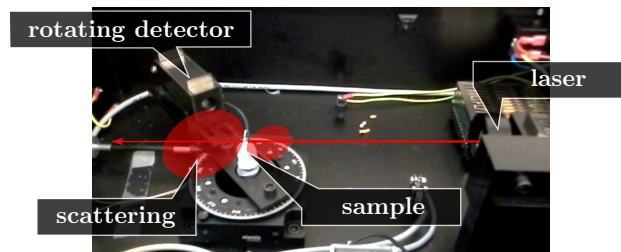
Figure 2.3: Angle resolved SLS, experimental setup.

2.3   Results and discussion

After spin coating of an aqueous solution of ammonium tungstate and PSS at high concentration of ammonia, the microstructure of the film was studied by Scanning Electron Microscopy (SEM) (fig. 2.4 a.) and STXM (fig. 2.5). SEM micrographs show that upon spin coating of the aqueous ammonium tungstate / PSS solution, micrometric domains are stabilized into droplets embedded in a matrix. This electron micrograph was realized by recording secondary electrons and the matrix appears darker than the droplets due to charging effects.

This contrast is not linked to the film topography but rather to differences in electric conductivity. The film surface before pyrolysis is indeed flat at the nanometer scale (annex 6, fig. A.2).
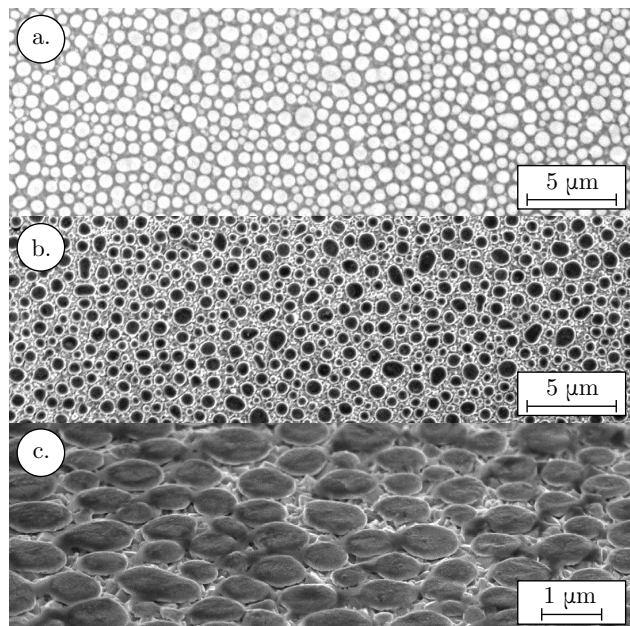

Figure 2.4: Ammonium tungstate / PSS film surface (spin coating speed 3000 rpm): a. SEM picture before pyrolysis (top view). b. SEM picture after pyrolysis (top view). c. SEM picture after pyrolysis (side view).
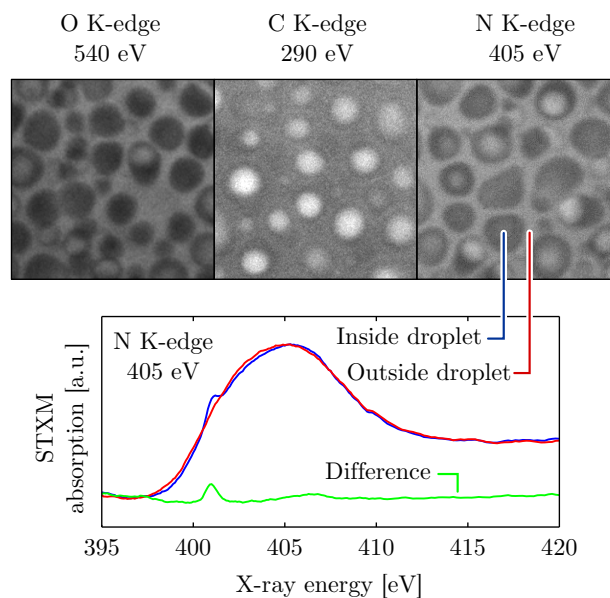

Figure 2.5: Scanning X-ray absorption microscopy (STXM) pictures at the O K-edge, the C K-edge and the N K-edge, before pyrolysis.

X-ray absorption with spatial resolution was also recorded on this film (fig. 2.5). STXM images prove that the matrix, between the droplets, is formed by the polymer, since the absorption at the carbon K-edge is higher in these regions. The droplets have a higher absorption of X-rays at the oxygen K-edge and can therefore contain some remaining water. Less absorption contrast is obtained at the nitrogen K-edge, because the substrates used for the STXM measurements are silicon nitride windows, also containing nitrogen in an amorphous phase. Nevertheless, a fine structure is present in the nitrogen K-edge spectra recorded inside the droplets which is absent outside the droplets. A similar peak at the nitrogen K-edge was observed by different authors[10,11] in $(NH_4)_2SO_4$ samples. This spectral feature corresponds to the well-known nitrogen $1s \rightarrow \pi^*$ transition in ammonium ions and proves the localization of ammonium tungstate inside the droplets.

This correlated SEM and STXM studies prove that polystyrene sulfonic acid is forming vesicles enclosing the ammonium tungstate precursor. A monolayer of those vesicles is coated

onto the substrate during the spin coating. Upon pyrolysis the polymer vesicles act as microreactors constraining the mWO_3 crystallization to spheroid shape with controlled dimensions (fig. 2.4 b. and c.). The phase and crystallinity of the mWO_3 phase was confirmed by X-ray diffraction (annex 6, fig. A.1).

I would like to understand how the microspheroids form from solution upon casting. One important observation I made is that the microspheroids forms only at high concentrations of ammonia. Therefore I decided to investigate the impact of ammonia concentration on the solution chemistry.

I observed that microspheroids form upon casting of PSS / AMT / NH_3 solutions when the concentration of NH_3 was higher than a critical value situated around 0.5 mol/L. In order to understand the reactions that occur in solution upon addition of NH_3, conductometric and pH-metric measurements were conducted on solutions containing a fixed concentration of PSS and AMT and various concentrations of NH_3. The pH and conductivity of these solutions were measured and plotted versus the concentration of NH_3 (fig. 2.6).

$$PSS^- + H_3O^+ + NH_3 \rightleftharpoons PSS^- + NH_4^+ + H_2O$$

$$(NH_4)_6H_2W_{12}O_{40}(H_2O)_{10} + 2\,NH_3 \rightleftharpoons [(NH_4)_6W_{12}O_{40}(H_2O)_{10}]^{2-} + 2\,NH_4^+$$
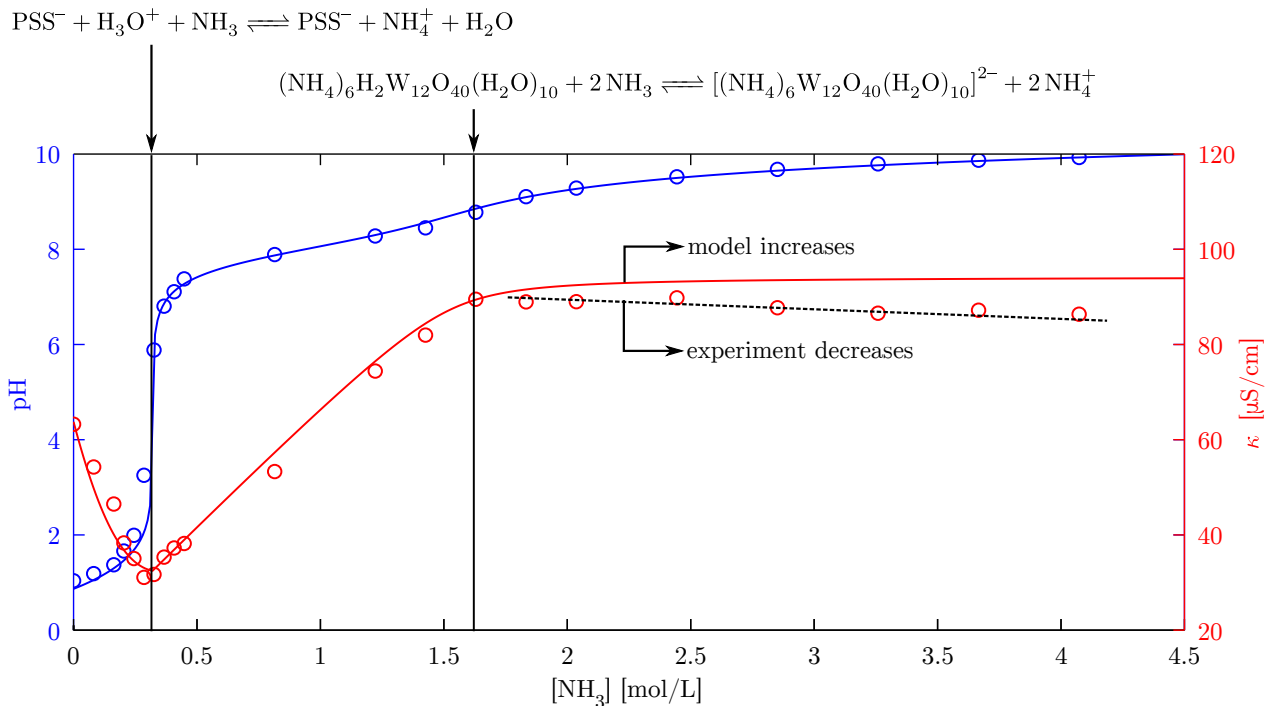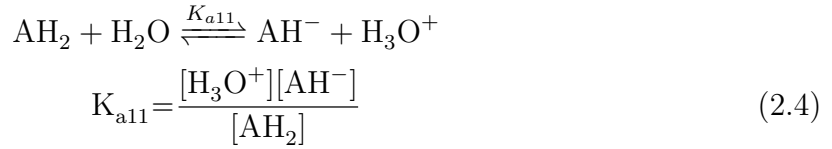
Figure 2.6: pH-metric (blue circles) and conductometric (red circles) titration curves obtained by fixing the concentrations of PSS (0.2 mol/L) and AMT (0.5 mol/L) and varying the concentration of NH_3. The blue line is the result of the pH modelization and the red curve the result of the conductivity modelization.
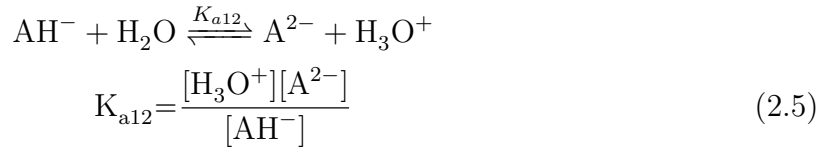
The pH and conductivity were modeled using the following reactions:

- Model reactions for AMT with AH_2 standing for $(NH_4)_6H_2W_{12}O_{40}(H_2O)_{10}$, AH^- standing for $[(NH_4)_6HW_{12}O_{40}(H_2O)_{10}]^-$ and A^{2-} standing for $[(NH_4)_6W_{12}O_{40}(H_2O)_{10}]^{2-}$:

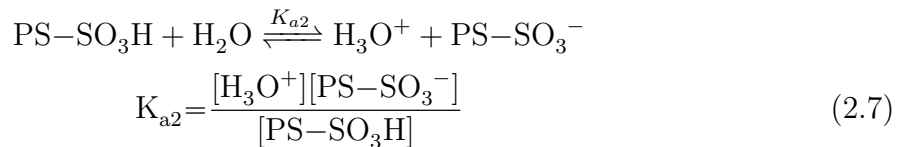<div align="center">Reaction of AH_2 with water:</div>

$$AH_2 + H_2O \xrightleftharpoons{K_{a11}} AH^- + H_3O^+$$

$$K_{a11} = \frac{[H_3O^+][AH^-]}{[AH_2]} \qquad (2.4)$$

<div align="center">Reaction of AH^- with water:</div>

$$AH^- + H_2O \xrightleftharpoons{K_{a12}} A^{2-} + H_3O^+$$

$$K_{a12} = \frac{[H_3O^+][A^{2-}]}{[AH^-]} \qquad (2.5)$$

<div align="center">Balance of tungsten:</div>

$$[AH_2] + [AH^-] + [A^{2-}] = [AH_2]_0 \qquad (2.6)$$

- Model reactions for PSS with $PS-SO_3H$ standing for the protonated sulfonic groups, and $PS-SO_3^-$ standing for the deprotonated sulfonic groups:
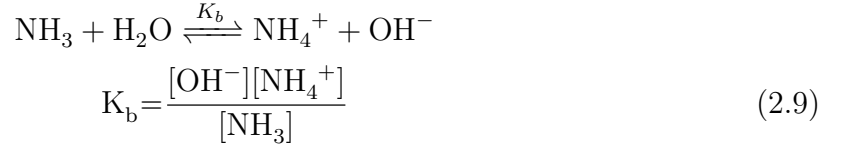
<div align="center">Reaction of PSS with water:</div>

$$PS-SO_3H + H_2O \xrightleftharpoons{K_{a2}} H_3O^+ + PS-SO_3^-$$

$$K_{a2} = \frac{[H_3O^+][PS-SO_3^-]}{[PS-SO_3H]} \qquad (2.7)$$

<div align="center">Balance of sulfur:</div>

$$[PS-SO_3H] + [PS-SO_3^-] = [PS-SO_3H]_0 \qquad (2.8)$$

- Model reaction for NH_3:

$$NH_3 + H_2O \xrightleftharpoons{K_b} NH_4^+ + OH^-$$

$$K_b = \frac{[OH^-][NH_4^+]}{[NH_3]} \tag{2.9}$$

Balance of nitrogen:

$$[NH_3] + [NH_4^+] = [NH_3]_0 \tag{2.10}$$

- Autoionization of water:

$$2\,H_2O \xrightleftharpoons{k_w} OH^- + H_3O^+$$

$$k_w = [OH^-][H_3O^+] \tag{2.11}$$
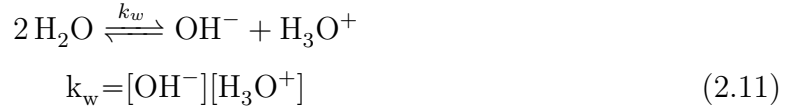
Using a balance of charges I calculate the pH and conductivity:

$$[PS-SO_3^-] + [AH^-] + 2\,[A^{2-}] + [OH^-] = [NH_4^+] + [H_3O^+] \tag{2.12}$$

Considering all of the equilibrium relations and mass balances described previously (equations 2.4 to 2.11), the equation 2.12 can be expressed as a function of $x = [H_3O^+]$ in a polynomial of degree 6:

$x^6 \times K_b$

$+\, x^5 \times (\, K_{a11}\, K_b\, +\, K_{a2}\, K_b\, +\, [NH_3]\, K_b\, +\, k_w\,)$

$-\, x^4 \times (\, [AH_2]_0\, K_{a11}\, K_b\, -\, [PS-SO_3H]_0\, K_{a2}\, K_b\, -\, K_b\, k_w\, +\, K_{a11}\, K_{a12}\, K_b\, +\, K_{a2}\, K_{a11}\, K_b\, +\, [NH_3]\, K_{a11}\, K_b\, +\, [NH_3]\, K_{a2}\, K_b\, +\, K_{a11}\, k_w\, +\, K_{a2}\, k_w\,)$

$-\, x^3 \times (2[AH_2]_0\, K_{a11}\, K_{a12}\, K_b\, -\, [PS-SO_3H]_0\, K_{a2}\, K_{a11}\, K_b\, -\, [AH_2]_0\, K_{a2}\, K_{a11}\, K_b\, +\, K_{a2}\, K_{a11}\, K_{a12}\, K_b\, +\, [NH_3]\, K_{a11}\, K_{a12}\, K_b\, +\, [NH_3]\, K_{a2}\, K_{a11}\, K_b\, -\, K_{a11}\, K_b\, k_w\, -\, K_{a2}\, K_b\, k_w\, -\, [AH_2]_0\, K_{a11}\, k_w\, -\, [PS-SO_3H]_0\, K_{a2}\, k_w\, +\, K_{a11}\, K_{a12}\, k_w\, +\, K_{a2}\, K_{a11}\, k_w\, -\, k_w^2\,)$

$-\, x^2 \times (\, [PS-SO_3H]_0\, K_{a2}\, K_{a11}\, K_{a12}\, K_b\, -\, 2\,[AH_2]_0\, K_{a2}\, K_{a11}\, K_{a12}\, K_b\, +\, [NH_3]\, K_{a2}\, K_{a11}\, K_{a12}\, K_b\, -\, K_{a11}\, K_{a12}\, K_b\, k_w\, -\, K_{a2}\, K_{a11}\, K_b\, k_w\, -\, 2\,[AH_2]_0\, K_{a11}\, K_{a12}\, k_w\, -\, [PS-SO_3H]_0\, K_{a2}\, K_{a11}\, k_w\, -\, [AH_2]_0\, K_{a2}\, K_{a11}\, k_w\, +\, K_{a2}\, K_{a11}\, K_{a12}\, k_w\, -\, K_{a11}\, k_w^2\, -\, K_{a2}\, k_w^2\,)$

$- \text{x} \times (\text{K}_{a2} \, \text{K}_{a11} \, \text{K}_{a12} \, \text{K}_{b} \, \text{k}_{w} \; - \; [\text{PS}-\text{SO}_3\text{H}]_0 \, \text{K}_{a2} \, \text{K}_{a11} \, \text{K}_{a12} \, \text{k}_{w} \; - \; 2 \, [\text{AH}_2]_0 \, \text{K}_{a2} \, \text{K}_{a11} \, \text{K}_{a12} \, \text{k}_{w} \; - $
$\text{K}_{a11} \, \text{K}_{a12} \, \text{k}_{w}{}^2 \; - \; \text{K}_{a2} \, \text{K}_{a11} \, \text{k}_{w}{}^2)$

$- \, \text{K}_{a2} \, \text{K}_{a11} \, \text{K}_{a12} \, \text{k}_{w}{}^2$

$= 0$

Solving this polynomial equation allows calculating the pH and the conductivity (κ):

pH = -$\log_{10}(\text{x})$

$$\kappa = \kappa_{(\text{H}_3\text{O}^+)} \cdot \text{x} + \kappa_{(\text{NH}_4{}^+)} \cdot \frac{\text{K}_b \cdot [\text{NH}_3] \cdot \text{x}}{\text{k}_w + \text{K}_b \cdot \text{x}} + \kappa_{(\text{OH}^-)} \cdot \frac{\text{k}_w}{\text{x}} + \kappa_{(\text{PS}-\text{SO}_3{}^-)} \cdot \frac{\text{K}_{a1} \cdot [\text{PS}-\text{SO}_3\text{H}]_0}{\text{x} + K_a} + \kappa_{(\text{AH}^-)} \cdot$$

$$\frac{[\text{AH}_2]_0}{1 + \dfrac{\text{x}}{\text{K}_{a11}} + \dfrac{\text{K}_{a12}}{\text{x}}} + \kappa_{(\text{A}^{2-})} \cdot \frac{2\text{K}_{a12} \cdot [\text{AH}_2]_0}{\text{K}_{a12} + x + \dfrac{\text{x}^2}{\text{K}_{a11}}}$$

The model parameters have the following values:

$\text{pK}_{a11} = 8$
$\text{pK}_{a12} = 8$
$\text{pK}_{a2} = 1$
$\text{pK}_b = 4.3$
$[\text{AH}_2]_0 = 0.6$ mol/L
$[\text{PSS}]_0 = 0.3$ mol/L
$\kappa_{(\text{A}^-)} = 0$ S.$(\text{mol/L})^{-1}.\text{cm}^{-1}$
$\kappa_{(\text{A}^{2-})} = 0$ S.$(\text{mol/L})^{-1}.\text{cm}^{-1}$
$\kappa_{(\text{PS}-\text{SO}_3{}^-)} = 0.05$ S.$(\text{mol/L})^{-1}.\text{cm}^{-1}$
$\kappa_{(\text{H}_3\text{O}^+)} = 0.3498$ S.$(\text{mol/L})^{-1}.\text{cm}^{-1}$
$\kappa_{(\text{OH}^-)} = 0.1986$ S.$(\text{mol/L})^{-1}.\text{cm}^{-1}$
$\kappa_{(\text{NH}_4{}^+)} = 0.0735$ S.$(\text{mol/L})^{-1}.\text{cm}^{-1}$

This model is in good agreement with the experimental data (fig. 2.6). Therefore the reactions in solution can be described by a deprotonation of the polymer, which was also observed in our previous studies, and the reaction of tungstate specie that acts as a diacid. I am showing here the most probable reaction of AMT with NH_3 but any reaction involving two protons can be considered. It is also interesting to see that there is a discrepancy for high concentrations of NH_3 between the model and experimental data in the conductometry measurement. The experimental data is decreasing while the model is increasing. In this

region it seems that the conductivity cannot be described by considering chemical reactions only. This discrepancy occurs in the range where microspheroids are obtained upon casting and could be a consequence of an aggregation of the polymer. When aggregates form the polymer conductivity is decreased, resulting in a molar conductivity decrease. This phenomenon is commonly used to determine critical micelle concentration [12,13].

In order to see if the chemical reactions described in the previous section lead to the formation of aggregates in solution I used DLS on the same solutions that were used for the titration experiment. Figure 2.7 shows the evolution of the correlation coefficient over time as a function of the NH_3 concentration in solution of 0.2 mol/L of PSS and 0.5 mol/L of AMT. The inversion point of the correlation coefficient curves shift to longer times from 0 to 0.5 mol/L of NH_3 and then saturates to around 10 µs. This correlation lag time corresponds to sizes in the range 5 to 15 nm. The trend of the shift can easily be characterized by plotting the correlation coefficient value at the shortest recorded time as a function of the NH_3 concentration (fig. 2.8).
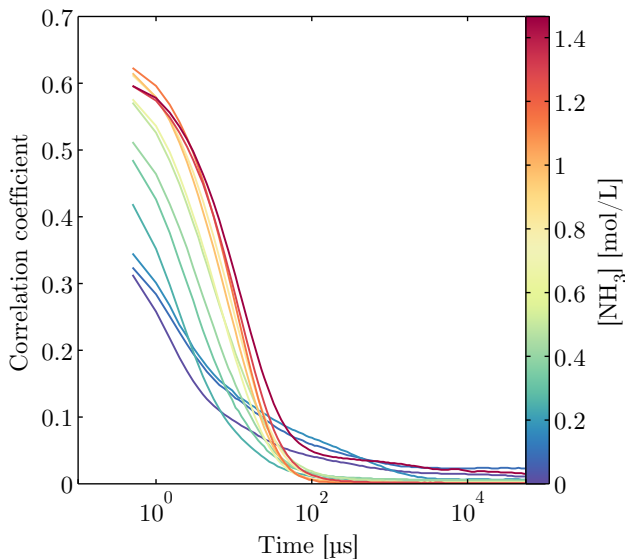
Figure 2.7: DLS correlograms as a function of the NH_3 concentration in a solution of 0.2 mol/L PSS and 0.5 mol/L AMT.
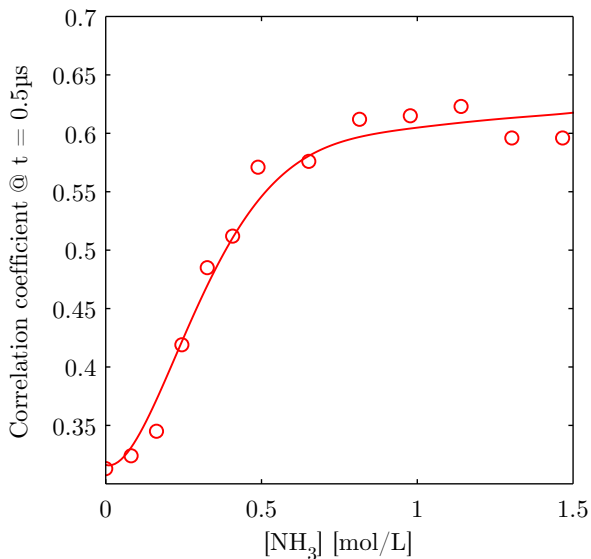
Figure 2.8: Correlation coefficient at 0.5 µs as a function of the concentration of NH_3. The correlation coefficient increases when the whole correlogram shifts to longer time scales.

The shift observed in the correlation curves with increasing concentration of NH_3 relates well with the titration curves reported in the previous section (see fig. 2.9, c.). The onset of saturation of the correlation curves at 0.5 mol/L of NH_3 occurs just after the first pH jump observed with titration, and the shift occurs during this pH jump. It therefore seems to be a relation between the aggregation of the polymer and its deprotonation. These chemical

processes also relate to the microspheroid formation upon spin coating. Before the full de-protonation of the polymer and saturation of the correlation curves shift no microspheroids can be observed upon spin coating (fig. 2.9 a.) whereas microspheroids could be observed in certain regions after this threshold (fig. 2.9 b.).
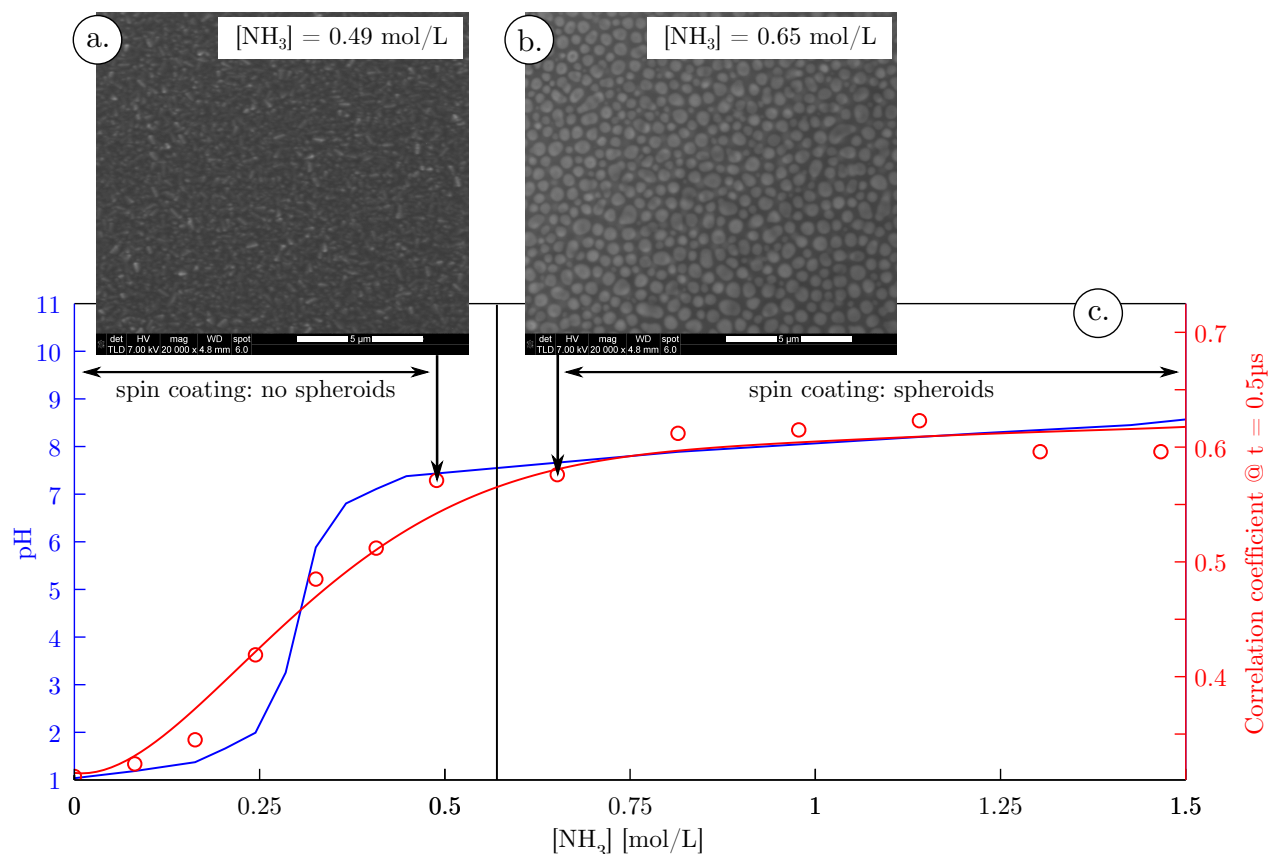

Figure 2.9: a. SEM of a film spin coated from a 0.2 mol/L PSS / 0.5 mol/L AMT and 0.49 mol/L NH_3, no microspheroids are observed. b. SEM of a film spin coated from a 0.2 mol/L PSS / 0.5 mol/L AMT and 0.65 mol/L NH_3, microspheroids are observed in some regions. c. Evolution of the pH and correlation coefficient at 0.5 µs as a function of the NH_3 concentration in a 0.2 mol/L PSS / 0.5 mol/L AMT solution.

This first DLS study shows that the polymer needs to be deprotonated in order to form the nanometric aggregates observed in solution. In addition this aggregate formation occurs at the same concentration as the microspheroid formation meaning these two aspects can be related. I wanted then to know whether the presence of the tungsten salt (AMT) in solution is necessary for the aggregates to form.

I measured DLS in solutions of the polymer (PSS) with different concentrations of NH_3 and no tungsten salt. In that case the inversion point of the correlation curves never reaches timescales that are measurable with the DLS instrument (fig. 2.10), meaning no particles

can be detected. The characteristic length increases also while deprotonation occurs but then decreases again when adding more NH_3 (fig. 2.11). We have seen already that SEM and Atomic Force Microscopy (AFM) studies of the films in that case did not show any microspheroid formation upon spin coating. Therefore the presence of AMT is necessary both for the microspheroid formation upon spin coating and for the formation of aggregates in solution observed with DLS.
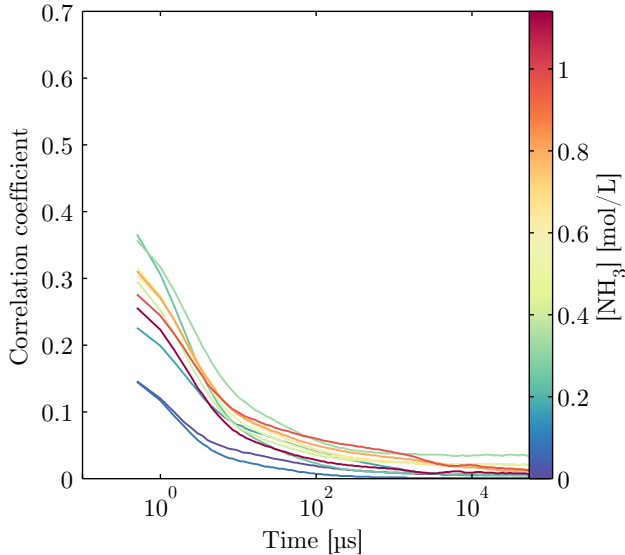
Figure 2.10: DLS correlograms as a function of the NH_3 concentration in a solution of 0.2 mol/L PSS
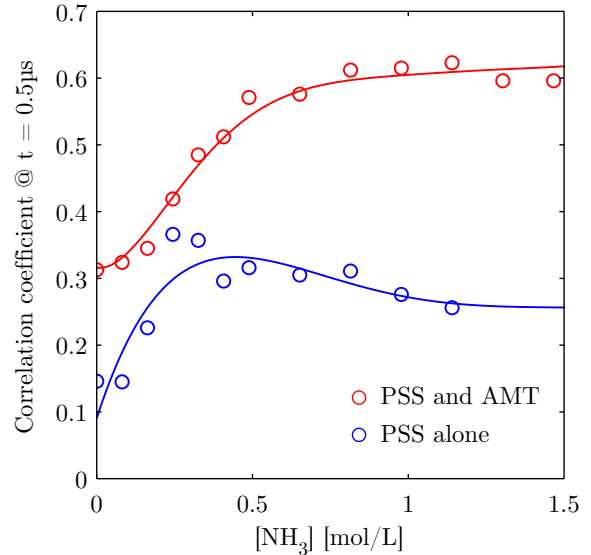
Figure 2.11: Correlation coefficient at 0.5 µs as a function of the concentration of NH_3. The correlation coefficient increases when the whole correlogram shifts to longer time scales.

The fact that the polymer forms aggregates in solution only when AMT is present points to studies in the literature on "polymer domain" formation in polyelectrolyte solutions. Studies on PSS solutions started in the 1950s[7,8,15,16] and show that this polyelectrolyte exists in a dispersed state at all pH values, but as coils and aggregates when the solution ionic strength is high. Further studies on the impact of salt addition to PSS solutions by Zhang et al.[14], using neutron and light scattering, show that the presence of salt leads to the formation of a polymer "cobweb" with two characteristic lengthscales (see fig. 2.12). The first lengthscale corresponds to the interchain distance (ξ_d) which they estimated between 8 and 16 nm using neutron scattering. The second lengthscale is the overall domain size (R_g) and was estimated by light scattering to range between 50 and 100 nm.

This theory is interesting but there is one major discrepancy between the light scattering

results of Zhang et al.[14] and ours. They observe with DLS a radius of gyration R_g which ranges from 50 to 100 nm, whereas in my DLS experiment the observed length is in the 5 to 15 nm range and rather matches the interchain distance (ξ_d). Therefore I wanted to prove that ionic strength can be the cause of the presence of the aggregates observed with DLS in the AMT / PSS / NH$_3$ system.

In order to test whether high ionic strengths can lead to the appearance of the characteristic 5 to 15 nm lengthscale observed with DLS on deprotonated PSS solutions containing AMT, I replaced this salt by NaCl. I investigated different concentrations of NaCl, ranging from 0 to 1 mol/L. DLS experiments on these solutions (figs. 2.13 and 2.14) clearly demonstrate that when increasing the amount of salt, hence the ionic strength in solution, the correlograms shift until they reach the typical 5 to 15 nm length I also observed with AMT. Therefore the polymer domain formation seems to be linked to a deprotonation of the polymer and the compensation of its charge by ions in solution.
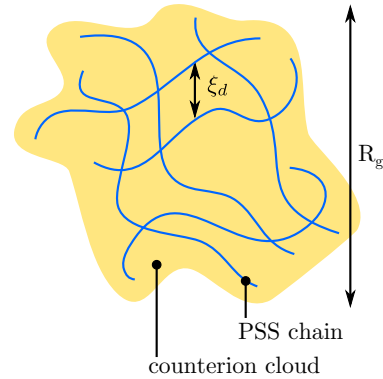

Figure 2.12: Scheme of a polymer domain, adapted from Zhang et al.[14].
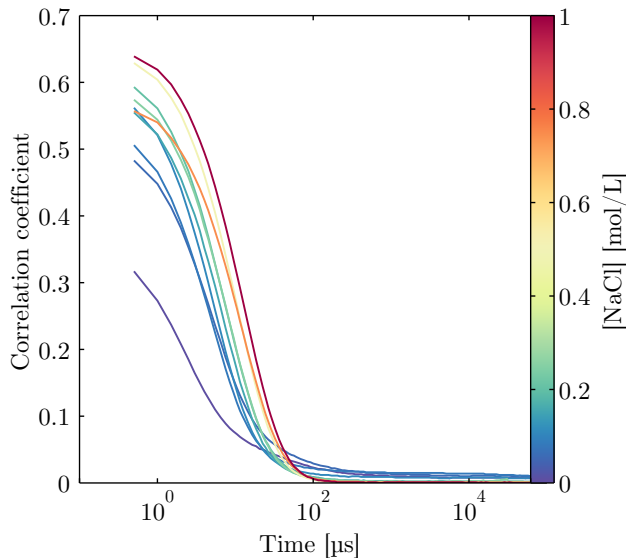

Figure 2.13: DLS correlograms as a function of the NaCl concentration in a solution of 0.2 mol/L PSS and 5 mol/L NH$_3$
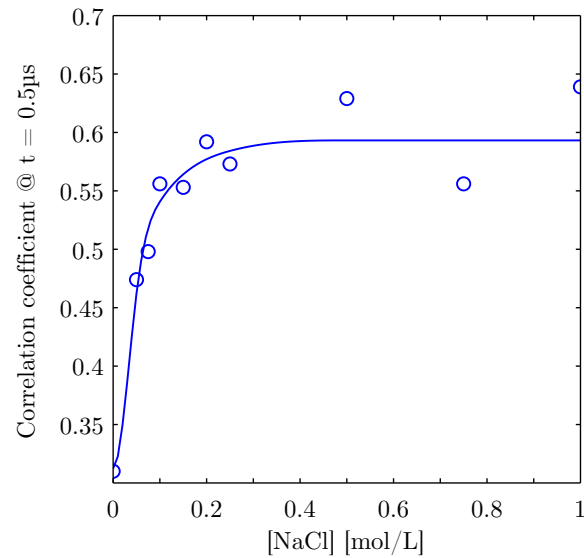
Figure 2.14: Correlation coefficient at 0.5 µs as a function of the concentration of NH$_3$. The correlation coefficient increases when the whole correlogram shifts to longer time scales.

I also investigated whether spin coating of the NaCl / PSS / NH$_3$ solutions could lead to microspheroids formation. Nevertheless, when coating these

films, I obtained fractal patterns similar to those already reported in the literature for this system[17] (see fig. 2.15). The article by Samanta and Mukherjee[17] reports that these patterns are formed first by a precipitation of NaCl excess species and then the aggregation of the polymeric domains containing additional NaCl on these first pattern. This may be a reason why I did not obtain microspheroids with NaCl, the main driving force for pattern formation being in that case the excess NaCl precipitation.

I learned from this DLS and SEM study that the PSS forms nano-metric domains in solution when it is deprotonated and when the solution ionic strength is high. In the case of AMT, the polymer is probably stabilized by AMT ions, $[(NH_4)_6HW_{12}O_{40}(H_2O)_{10}]^-$ and $[(NH_4)_6W_{12}O_{40}(H_2O)_{10}]^{2-}$. In addition when these nanometric domains form, the microspheroids are also appearing during spin coating. Hence the polymeric domains may be aggregating upon casting to form the microspheroids. To gain a better understanding of the transition that could occur from the polymeric domains to the microspheroids obtained upon spin coating I have performed static light scattering experiments during casting and after casting of the AMT / PSS/ NH_3 solutions.
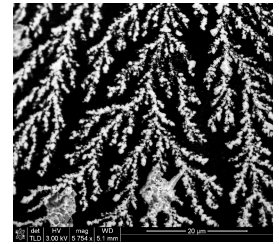

Figure 2.15: SEM of fractal patterns obtained when coating the NaCl/PSS/NH_3 solutions.

In-situ interferometry allows following interferences variations over time occurring during spin coating due to the decrease of film thickness. But this technique was also used in the literature to monitor other structural changes, such as phase separation[9]. An increase in scattering due to the formation of microspheroids during spin coating could be observed by a decrease in the reflected intensity over time.

Due to vibrations of the spin coater leading to oscillations of the reflected laser I used a band pass filter to increase the signal to noise ratio (see fig. 2.16 a.). The resulting spectra are not valid in the first 3 seconds because the frequency of the spin coater oscillations and the frequency of the interferences are similar in this region (grayed regions in c2.16). The treated data after 3 seconds was used for analysis.

For two different spin coating speeds, 1500 rpm (fig. 2.16 b.) and 2000 rpm (fig. 2.16 c.), coating a solution that forms microspheroids leads to a decrease of the reflected intensity (blue curves in fig. 2.16) while the reflection on film that do not form microspheroids remains relatively constant (red curves in fig. 2.16). This trend may be caused by an increase of the scattering over time, consequence of the microspheroid formation during coating.
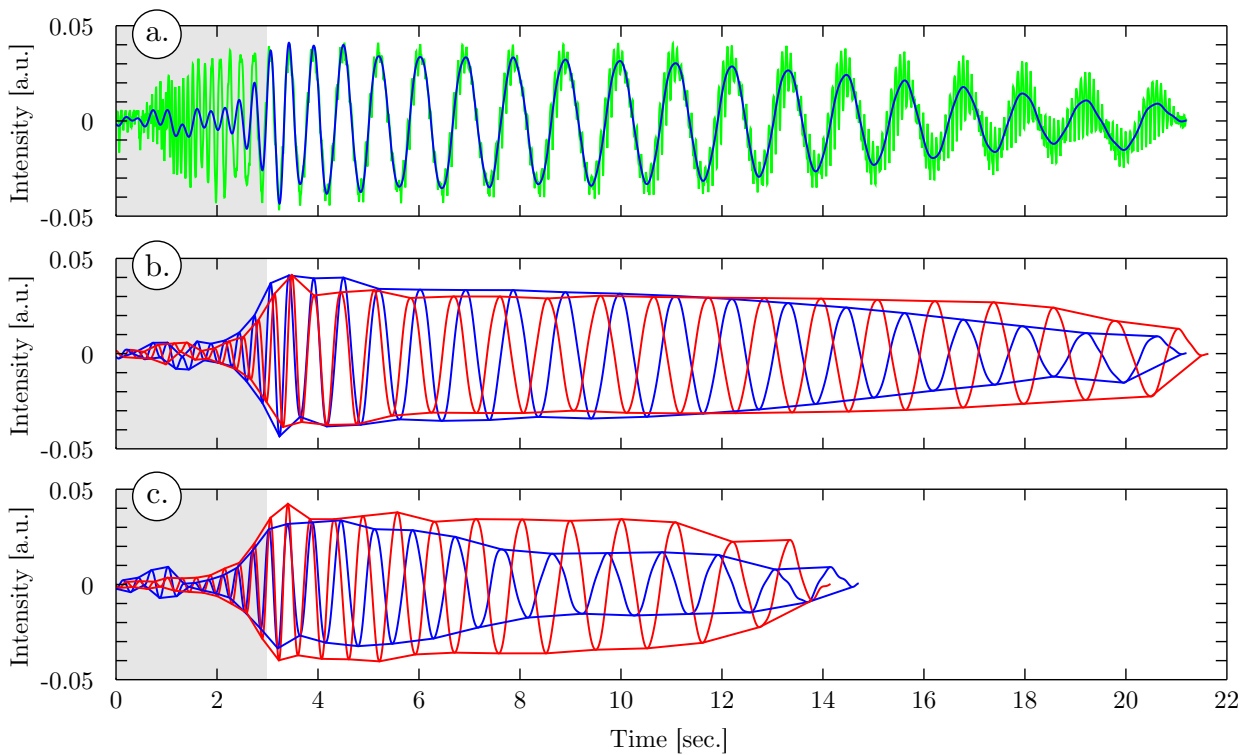
Figure 2.16: a. Raw interferogram (green line) and the same interferogram with the band pass treatment (blue line). b. Films spin coated at 1500 rpm: film with spheroids (0.2 mol/L PSS / 0.5 mol/L AMT / 5 mol/L NH$_3$, blue line) and film without spheroids (0.2 mol/L PSS / 0.5 mol/L AMT / 0.25 mol/L NH$_3$, red line). c. Films spin coated at 2000 rpm: film with spheroids (0.2 mol/L PSS / 0.5 mol/L AMT / 5 mol/L NH$_3$, blue line) and film without spheroids (0.2 mol/L PSS / 0.5 mol/L AMT / 0.25 mol/L NH$_3$, red line)

In order to verify whether this decrease in intensity can really be attributed to an increase of scattering over time I measured the scattering pattern of a film composed of microspheroids just after its spin coating. Significant scattering effects from the spheroids could be observed for wavelengths between 400 and 700 nm (see fig. 2.17). UV-visible spectroscopy (fig. 2.18) shows that below 400 nm more scattering is expected but the polymer is absorbing light significantly at these wavelengths leading to scattering spectra with very low signal to noise ratios. Hence scattering effects are significant at the wavelength where the laser operate (650 nm) in the in-situ interferometry experiments. The decrease in reflected light in this in-situ experiment can therefore be linked to light scattering.
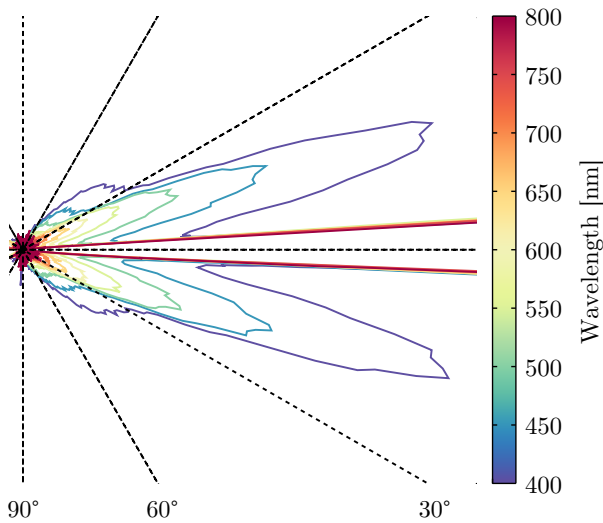
Figure 2.17: Angular scattering patterns as a function of the incident laser wavelength, from a film composed of microspheroids (0.2 mol/L PSS / 0.5 mol/L AMT / 5 mol/L NH_3)
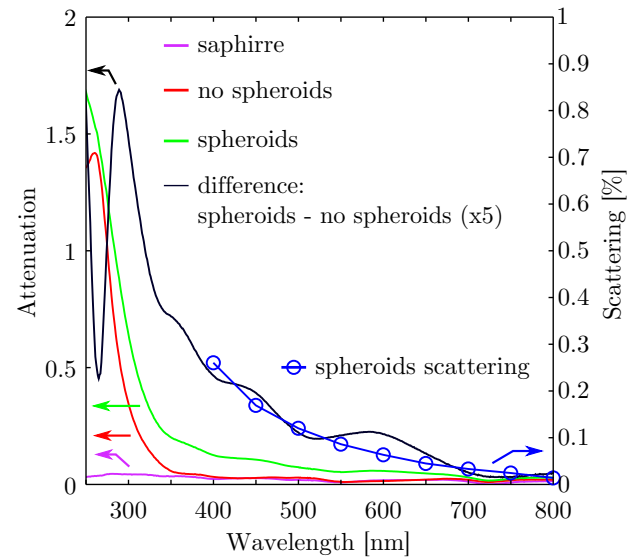
Figure 2.18: UV-visible transmission spectroscopy spectra from the substrate (sapphire, pink line); from a film without spheroids (0.2 mol/L PSS / 0.5 mol/L AMT / 0.25 mol/L NH_3, no spheroids, red line); from a film with spheroids (0.2 mol/L PSS / 0.5 mol/L AMT / 5 mol/L NH_3, spheroids, green line); difference spectra between the film with spheroids and the film without, multiplied by 5 for visibility; and amount of scattered intensity from a film with spheroids (spheroids scattering, blue line with blue cicles).

2.4 Conclusions

I have discovered, using DLS, that PSS nanometric domains form in solution when the polymer is deprotonated and when the solution ionic strength is high. In addition, coupling DLS and SEM experiments showed that the apparition of the polymer domains in solution and the formation of microspheroids upon casting occur at similar NH_3 concentration. There is therefore a relationship between these two aspects. One hypothesis is that the nanometric domains aggregate during spin coating into micrometric objects. In-situ interferometry during spin coating seems to show that light scattering appears during the spin coating process and increases until the film dries completely. Light scattering experiments after spin coating confirmed that this decrease in reflectivity during spin coating can be related to a scattering effect. This in-situ study seems to corroborate that the microspheroids appear during the coating process and could therefore emerge from the nanodomains in solution.

These self-assembled micrometric domains obtained upon spin coating can be converted to mWO_3 by a simple pyrolysis step. This facile synthesis route offers an inexpensive and upscalable way to obtain mWO_3 photoanodes with an original microstructure. In the next chapter we will see that these spheroids can be coated with a nanometric layer of hematite to obtain an all-oxide heterojunction photoanode and we will characterize the PE response of those films.

References

1. ⬀. Renata Solarska, Rafal Jurczakowski, and Jan Augustynski. A highly stable, efficient visible-light driven water photoelectrolysis system using a nanocrystalline WO_3 photoanode and a methane sulfonic acid electrolyte. *Nanoscale*, 4(5):1553–1556, 2012.

2. ⬀. Renata Solarska, Agata Krolikowska, and Jan Augustynski. Silver Nanoparticle Induced Photocurrent Enhancement at WO_3 Photoanodes. *Angewandte Chemie-international Edition*, 49(43):7980–7983, 2010.

3. ⬀. R. Solarska, B. D. Alexander, A. Braun, R. Jurczakowski, G. Fortunato, M. Stiefel, T. Graule, and J. Augustynski. Tailoring the morphology of WO_3 films with substitutional cation doping: Effect on the photoelectrochemical properties. *Electrochemica Acta*, 55(26): 7780–7787, March 2010.

4. ⬀. Xiaoqing Chen, Jinhua Ye, Shuxin Ouyang, Tetsuya Kako, Zhaosheng Li, and Zhigang Zou. Enhanced Incident Photon-to-Electron Conversion Efficiency of Tungsten Trioxide Photoanodes Based on 3D-Photonic Crystal Design. *Acs Nano*, 5(6):4310–4318, June 2011.

5. ⬀. V. M. Prabhu, M. Muthukumar, G. D. Wignall, and Y. B. Melnichenko. Dimensions of polyelectrolyte chains and concentration fluctuations in semidilute solutions of sodium-poly (styrene sulfonate) as measured by small-angle neutron scattering. *Polymer*, 42(21): 8935–8946, October 2001.

6. ⬀. V. M. Prabhu, M. Muthukumar, G. D. Wignall, and Y. B. Melnichenko. Polyelectrolyte chain dimensions and concentration fluctuations near phase boundaries. *Journal of Chemical Physics*, 119(7):4085–4098, August 2003.

7. ⬲. R. A. Mock and C. A. Marshall. Vinyltoluene-styrene Copolymer Sulfonic Acid
    .1. Viscous Properties and Ionic Character In Hydrochloric Acid Solutions. *Journal of
    Polymer Science*, 13(69):263–277, 1954.

8. ⬲. R. A. Mock, C. A. Marshall, and T. E. Slykhouse. Vinyltoluene-styrene Copolymer
    Sulfonic Acids .2. Ionic Dissociation In Methanol-water and Hcl-water Solutions. *Journal
    of Physical Chemistry*, 58(6):498–503, 1954.

9. ⬲. P. C. Jukes, S. Y. Heriot, J. S. Sharp, and R. A. L. Jones. Time-resolved light
    scattering studies of phase separation in thin film semiconducting polymer blends during
    spin-coating. *Macromolecules*, 38(6):2030–2032, March 2005.

10. ⬲. S. Török, J. Osàn, B. Beckhoff, and G. Ulm. Ultratrace speciation of nitrogen com-
    pounds in aerosols collected on silicon wafer surfaces by means of TXRF-NEXAFS. *Powder
    Diffraction*, 19:81–86, February 2004. ISSN 1945-7413.

11. ⬲. Adam W. Gillespie, Fran L. Walley, Richard E. Farrell, Tom Z. Regier, and Robert
    I. R. Blyth. Calibration method at the N *K*-edge using interstitial nitrogen gas in solid-
    state nitrogen-containing inorganic compounds. *Journal of Synchrotron Radiation*, 15(5):
    532–534, Sep 2008.

12. ⬲. E. Minatti and D. Zanette. Salt effects on the interaction of poly(ethylene ox-
    ide) and sodium dodecyl sulfate measured by conductivity. *Colloids and Surfaces A-
    physicochemical and Engineering Aspects*, 113(3):237–246, August 1996.

13. ⬲. M. Perez-Rodriguez, G. Prieto, C. Rega, L. M. Varela, F. Sarmiento, and V. Mos-
    quera. A comparative study of the determination of the critical micelle concentration by
    conductivity and dielectric constant measurements. *Langmuir*, 14(16):4422–4426, August
    1998.

14. ⬲. Y. B. Zhang, J. F. Douglas, B. D. Ermi, and E. J. Amis. Influence of counterion
    valency on the scattering properties of highly charged polyelectrolyte solutions. *Journal
    of Chemical Physics*, 114(7):3299–3313, February 2001.

15. ⬲. U. P. Strauss and Y. P. Leung. Volume Changes As A Criterion For Site Binding
    of Counterions By Polyelectrolytes. *Journal of the American Chemical Society*, 87(7):
    1476–&, 1965.

16. ⚏. A. Takahashi, T. Kato, and M. Nagasawa. 2nd Virial Coefficient of Polyelectrolytes. *Journal of Physical Chemistry*, 71(7):2001–&, 1967.

17. ⚏. T. Samanta and M. Mukherjee. Effect of added salt on morphology of ultrathin polyelectrolyte films. *Polymer*, 53(23):5393–5403, October 2012.

Chapter 3

Photoelectrochemical water splitting with hematite coated mWO$_3$ microspheroids

In the previous chapter we have seen how mWO$_3$ can self-assemble in a film constituted of a monolayer of oblate spheroids. When coated with a hematite overlayer this film constitute a photoanode for photoelectrochemical applications involving an all-oxide heterojunction. I will study in this chapter the PE behavior of those films. In addition we will see that the microspheroids size distribution can be controlled by tuning a single processing step. We will examine in particular the impact of the microspheroids size distribution on the film PE characteristics.

3.1   Introduction

Hydrogen production by solar water splitting in photoelectrochemical cells (PEC) is one of the technologies that could lead to economically viable hydrogen economy. This technology is based on photo-electrolysis of water and allows to split water into O$_2$ (anode) and H$_2$ (cathode). If photoactive materials are used to harness solar light, and provide the electric voltage needed to split water, H$_2$ is produced without generation of harmful byproducts and can be easily collected at the cathode. Compared to other solar hydrogen technologies, PEC

cells are beneficial in terms of system integration since PEC electrodes combine light absorption and electrocatalysis.

A major problem encountered when developing photoelectrode materials based on inorganic semiconductors is the combination of a low conductivity and limited light absorption. In the present study I propose to address this fundamental limitation by combining two different approaches: matching the electronic structure and optical properties of two different semiconductors and controlling their microstructure.

Tungsten oxide (mWO$_3$) and hematite (α-Fe$_2$O$_3$) have been extensively studied as photoanode materials for solar water splitting. These two oxides possess a valence band at energy lower than the oxygen evolution reaction potential, allowing to catalyze this reaction by providing photogenerated holes at their surface. Moreover their narrow band gap allows light absorption in the near UV by the tungsten oxide and in the visible range by hematite. State of the art hematite photoelectrodes, prepared by atmospheric pressure chemical vapor deposition, reach 3.3 mA.cm^{-2} at 1.43 V$_{RHE}$[1], while mWO$_3$ photoelectrodes can reach around 3 mA.cm^{-2} at the same potential for micrometer thick films[2]. Some studies aimed at coupling hematite and mWO$_3$ in an oxide heterojunction[3–6]. Coupling these two oxides in a heterojunction would allow absorption of up to 35% of the solar power spectrum. In addition, a depletion layer that can improve the separation of the photogenerated hole/electron pairs is forming at the mWO$_3$/hematite junction, emerging from a favorable matching of the valence and conduction bands in those materials.

Such design is nevertheless hindered by the low conductivity of metal oxides. This is particularly true for hematite and Kennedy and Frese[7] reported that the charge carrier diffusion length in hematite was close to 5 nm and further studies by Le Formal *et al.*[8] point to even shorter lengths (1-2 nm). This diffusion length is one order of magnitude shorter than hematite's optical thickness (44.6 nm at a wavelength of 400 nm[9]). Therefore, the full capability of hematite cannot be achieved in the case of a flat thin film geometry where increasing the film thickness would lead to more charge carrier accumulation (charging) and decreasing the film thickness would lead to less light absorption. In the present study I propose to decouple light absorption from the metal oxide film thickness using controlled microstructures.

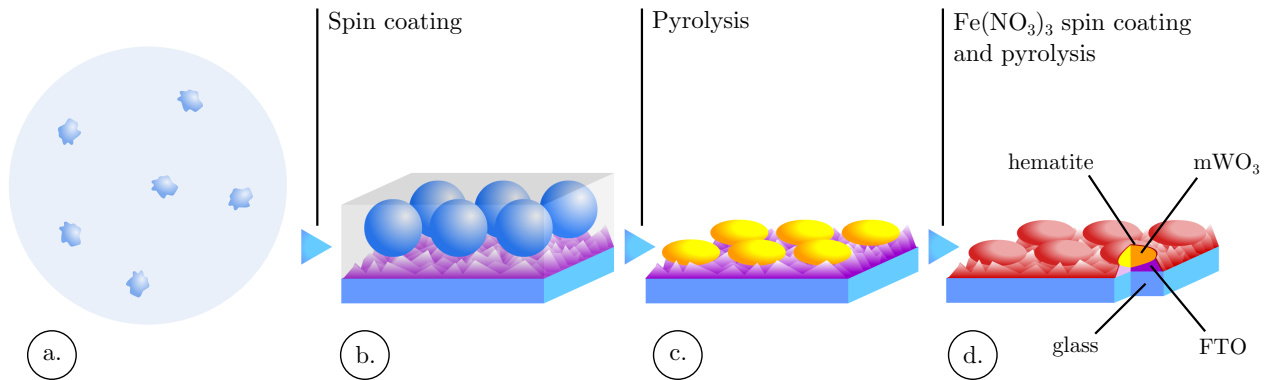## 3.2 Material and methods

3.2.1 Photoanodes preparation

Figure 3.1: Flow sketch of the mWO$_3$ microspheroids self-organization and hematite coating. a. PSS vesicle suspension in an ammonium tungstate solution for spin coating. b. Polymer film enclosing ammonium tungstate, after spin coating on FTO coated glass. c. mWO$_3$ spheroids after the first pyrolysis. d. Finalized film after Fe(NO$_3$)$_3$ / ethanol spin coating and pyrolysis.

The films preparation consists of four steps, depicted in fig. 3.1. The first step of the process consists in preparing a PSS / AMT / NH$_3$ as described in section 2.2.1, with a high concentration of ammonia in order to obtain PSS / AMT nanodomain formation (fig. 3.1 a.). This solution is spin coated on fluorinated tin-oxide coated aluminoborosilicate glass, 10 Ω/sq from Solaronix (fig. 3.1 b.). Different spin coating speeds are applied, ranging from 1000 rpm to 6000 rpm. The other spin coating parameters are kept constant, the holding speed is reached within 2 seconds and the holding time is 60 seconds. The spin coater used in this study is a Primus STT15 from ATMgroup. After spin coating the films are pyrolysed at 500°C for 2 hours and result in a tungsten oxide layer constituted of micrometric spheroids, sintered on the FTO surface (fig. 3.1 c.). The last step of the thin film preparation is the deposition of a hematite thin film overlay (fig. 3.1 d.). This thin film is obtained by spin coating Fe(NO$_3$)$_3$, dissolved in ethanol, at 6000 rpm for 60 seconds (holding speed reached within 2 seconds). By tuning the Fe(NO$_3$)$_3$ concentration between 0.0125M and 0.5M, hematite thin films with thicknesses ranging from a few nanometers to 30 nm have been obtained.

3.2.2   Photoelectrochemistry

The photoelectrochemical measurements were performed with a Voltalab PGZ402 potentiostat from Radiometer Analytical using a three electrode setup. A platinum electrode was used as counter electrode and a Ag/AgCl electrode was used as reference electrode. The measurement were carried under AM 1.5 illumination from a Lot-Oriel solar simulator. The electrolyte used in this study was a 0.05mol/L Phosphate Buffered Saline (solution) (PBS).

3.3   Results and discussion

An ultra-thin hematite film was casted on top of the mWO$_3$ film composed of spheroids, self-assembled according to the process described in the previous chapter. This film was produced by pyrolysis of a spin coated Fe(NO$_3$)$_3$ salt dissolved in ethanol. By tuning the concentration of Fe(NO$_3$)$_3$ different hematite thicknesses were obtained. Due to the strong scattering linked to the mWO$_3$ microstructure, the thickness of the hematite layer coated on the mWO$_3$ could not be measured by UV-visible spectroscopy. Therefore, the hematite films were first casted on transparent substrates (bare FTO glass) and analyzed by absorption spectroscopy (annex 6, fig. B.1). Characteristic hematite spectra were obtained. Assuming a Lambertian absorption and negligible reflection, the film thicknesses was calculated using the Beer-Lambert law:

$$L = \frac{A}{\alpha} \tag{3.1}$$

In this relation, L is the film thickness, α the absorption coefficient of hematite for a wavelength of 400 nm and A the absorbance measured at 400 nm. The absorption coefficient value of hematite at 400 nm was set to 2.24×10^{-2} nm^{-1} according to Marusak et al.[9]. A linear relationship (annex 6, fig. B.2) was observed between the Fe(NO$_3$)$_3$ concentration ([Fe(NO$_3$)$_3$]) and the hematite film thickness upon pyrolysis (L): $L = 52 \times$ [Fe(NO$_3$)$_3$]

No photocurrent was observed for these plain hematite films casted on bare FTO substrates, for all screened thicknesses. In order to observe the influence of the film thickness on the photocurrent, hematite ultra-thin films with thicknesses ranging from a few nanometer to 30 nm were casted on microstructured mWO$_3$ thin films. Due to the junction formed with mWO$_3$, and light trapping effects, a significant contribution of hematite to the photocurrent

could be recorded. Similar wetting behavior was observed experimentally when casting the iron solution on bare FTO substrates and mWO$_3$ coated FTO substrates. In addition charging effects in hematite, which will be discussed in details later in this paper, have a similar evolution as a function of the Fe(NO$_3$)$_3$ concentration when coated on mWO$_3$ and on bare FTO substrates (annex 6, fig. B.3). We therefore conclude that the observations of hematite thicknesses performed on bare FTO substrates can be applied to the mWO$_3$ coated FTO substrates case.

The curve presented in fig. 3.2 a. (light blue) shows a characteristic photocurrent/voltage signature obtained with the mWO$_3$ film composed of spheroids, coated with an ulta-thin hematite overlayer. This curve can be deconvoluted into two sigmoids. One of the sigmoids corresponds to the photocurrent generated by the mWO$_3$, which has an onset potential at around 0.2 V vs Ag/AgCl (yellow curve) and the second sigmoid corresponds to hematite, with an onset potential positioned at around 0.6 V vs Ag/AgCl (red curve). This difference is linked to a down shift of the conduction band in mWO$_3$ compared to hematite that provides mWO$_3$ with a better catalytic activity regarding the oxygen evolution reaction. A systematic study of the charging effects observed when chopping the light and monitoring the photocurrent response allowed quantifying the recombination length of the charge carrier in our hematite films (fig. 3.2 a., deep blue curve). When measuring the photocurrent at different potentials while opening / closing the light incident to the sample with a frequency of 1 Hz, transient phenomena can be characterized. These transient phenomena correspond to charging / discharging effects that are linked to the poor conductivity of hematite[8,10,11]. In a similar approach to Le Formal et al.[8] the discharging occurring in hematite after opening of the light shutter can be fitted by a single exponential:

$$J(t) = (J(t_0) - J(t_\infty))\, e^{\frac{t-t_0}{\tau}} \qquad (3.2)$$

In this formula, $J(t_\infty)$ is the photocurrent density at equilibrium, t_0 is the time when the light shutter is opened and τ is the characteristic decay time of the exponential. One example of this fitting procedure is presented in fig. 3.2 b. When plotting $J(t_0) - J(t_\infty)$, which gives the amplitude of charging, depending on the hematite thickness (fig. 3.2 c.), it is obvious that the charge carrier recombination is hindered when the hematite thickness is below 10 nm. This drastic decrease in charging for hematite films with a few nanometer thicknesses is well matching the values reported in the literature for the charge carrier recombination

length in hematite[7,8]. The optimal photocurrent has been obtained for a hematite thickness of 5 nm, where the film is thin enough for efficient charge carrier collection. The decrease in photocurrent observed for hematite thickness of 1-3 nm can be attributed to lower light absorption. Therefore the optimized hematite thickness that has been used to study the impact of light trapping is 5 nm, which constitutes a good compromise between light absorption and charge carrier transport.
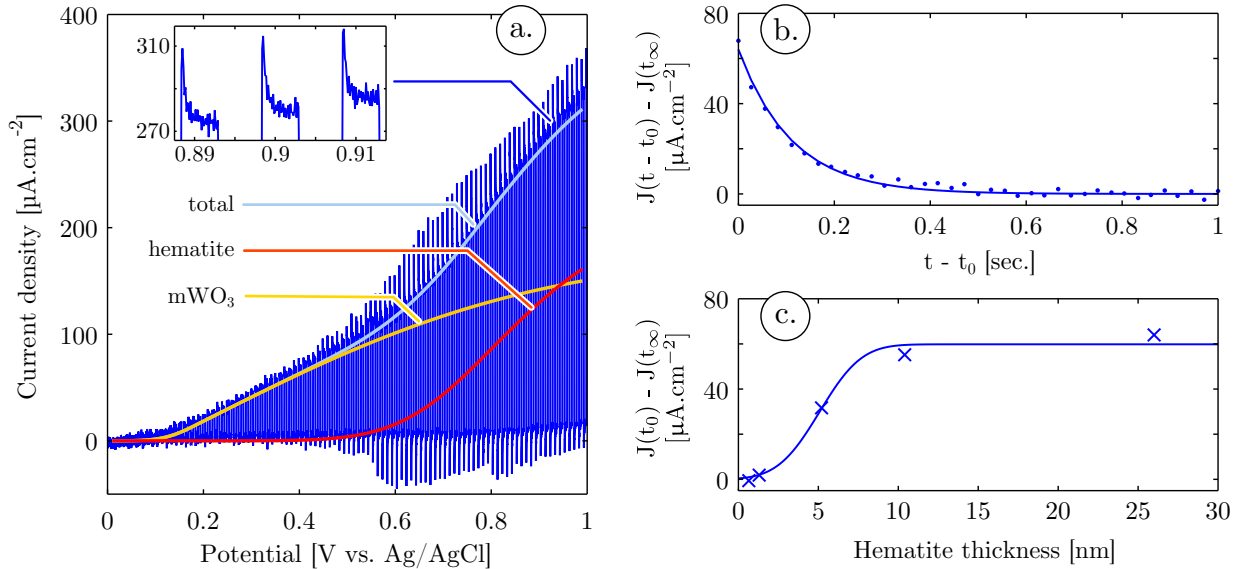

Figure 3.2: a. Typical curve obtained when chopping the light at 1Hz while recording the photocurrent at different potentials versus Ag/AgCl reference electrode in PBS electrolyte (pH = 7). The blue curve is the result of such measurement on a mWO$_3$ film made of spheroids (processed at 2000 rpm) with a 5 nm thick hematite overlayer. The yellow and red curves represent the two sigmoids that can be fitted to the photocurrent at equilibrium, they correspond to mWO$_3$ and hematite respectively. b. Example of decay observed for a 30 nm hematite thin film and the corresponding exponential fitting according to equation 3.2. c. Dependency of the charging amplitude over the film thickness.

A strong advantage procured by the bottom-up approach implemented in this study is the possibility to easily control the mWO$_3$ spheroid sizes in the micrometric to submicrometric range. By changing one parameter of the mWO$_3$ film casting, the spin coating speed, different film thickness are obtained. The polymer nanodomain aggregation upon casting is strongly influenced by the film thickness which is directly related to the spin coating speed. After pyrolysis of films processed at different spin coating speeds, mWO$_3$ thin films composed of spheroids with different size distributions are obtained. AFM scans and SEM imaging performed on these films show that the spheroid diameter varies from 1.2 μm to 0.5 μm. Their aspect ratio is constant and approximately equal to 1/3 (height/diameter) for all the screened spin coating speeds. To probe the photoelectrochemical properties of the films, photocur-

rent densities at varying potentials were measured on the films with different spheroid size distributions. These films were measured at pH = 7 in a 0.05M PBS electrolyte. Different behaviors were obtained depending on the mWO₃ microstructure (fig. 3.4). For all microstructures a similar shape of the photocurrent was obtained, allowing a clear distinction between hematite and mWO₃ contributions to the photocurrent densities. The photocurrents show a clear trend, an increase of the hematite contribution to the photocurrent and a decrease of the mWO₃ contribution to the photocurrent when decreasing the mWO₃ spheroid sizes (i.e. increasing the spin coating speed).
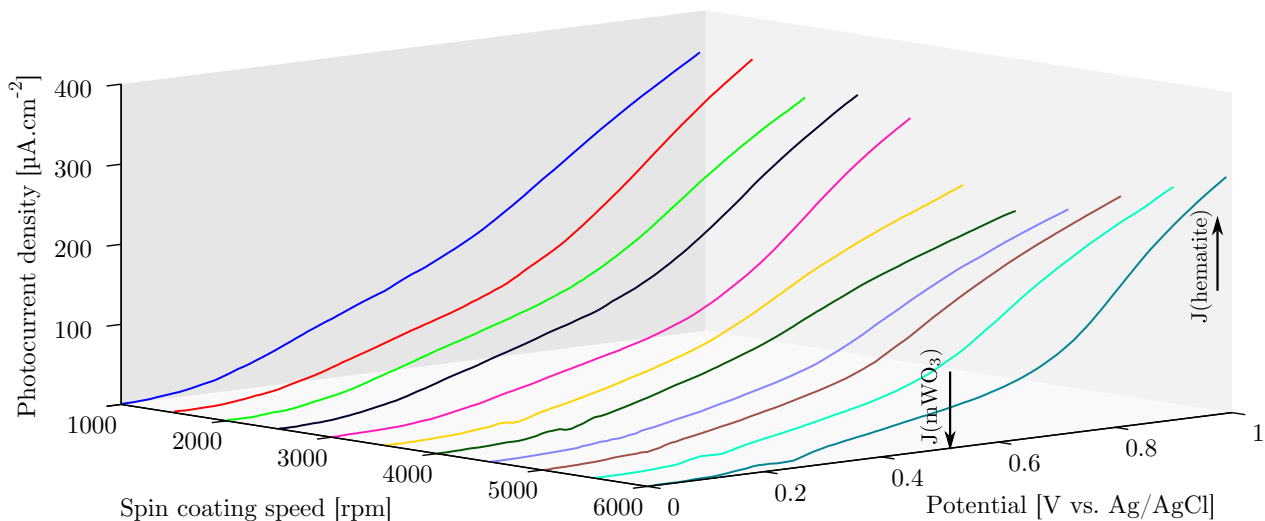

Figure 3.3: Photocurrents obtained at different applied bias for thin films coated at different spin coating speeds.

In order to characterize these variations quantitatively, a deconvolution of the photocurrent into two sigmoidal contributions was performed on each photocurrent / voltage curve, using a similar procedure as the one presented in fig. 3.2 a. In the Figure 3.4 a. and b., the values of the deconvoluted contribution of mWO₃ and hematite photocurrents at 0.9 V vs Ag(AgCl) were plotted for the different microstructures. The trend observed in the contribution of each oxide shows that the photoactivity of hematite is increasing while the photoactivity of mWO₃ is decreasing when the spheroid sizes are decreasing. An additional information obtained through this deconvolution is that the onset potentials for mWO₃ and hematite are invariant with the different microstructures, hence the change in microstructure do not influence the catalytic properties of the oxides.

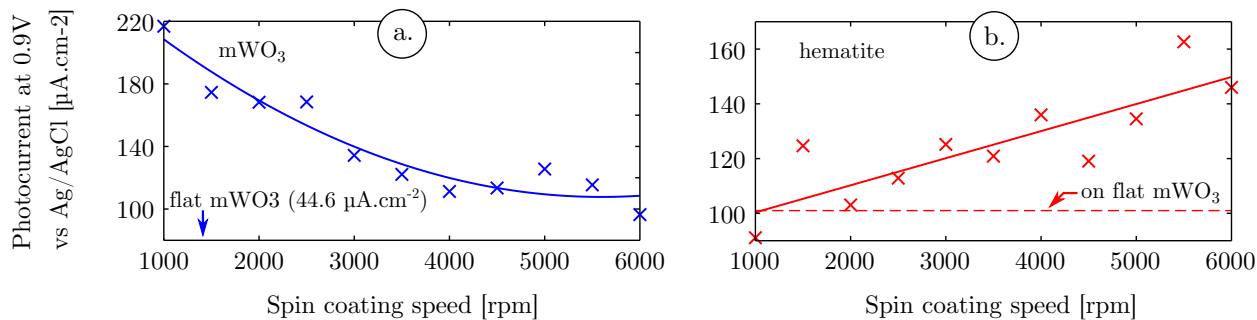In addition I compared the photocurrent density obtained with a flat mWO₃ film, coated

Figure 3.4: Photocurrent densities at 0.9V vs Ag/AgCl (current density under illumination - dark current density) as a function of the spin coating speed. Contributions from: a. hematite; and b. mWO$_3$; deconvoluted from the photocurrent presented in fig. 3.3

with hematite, to the photocurrent densities obtained with microstructured films (annex 6, fig. B.4). The photonic effects provide a two to four fold enhancement of mWO$_3$ photoactivity (fig. 3.4 b.). Hematite already benefits from a significant photoactivity in the flat film design because of the heterojunction with mWO$_3$. Nevertheless for the smallest spheroid sizes a 1.5 fold enhancement is observed for this oxide (fig. 3.4 a.).

3.4   Conclusions

In this chapter I presented the PE behavior of mWO$_3$ films composed of spheroids that were further coated with a hematite ultra-thin film. A comprehensive analysis of the charging effects in the hematite ultra-thin film overlay was also conducted. A good compromise between light absorption and charge carrier collection was obtained by correlating the hematite film thickness to its charging behavior. The spheroids size distribution can be easily tuned in the micrometric to submicrometric range by changing a simple process step, the spin coating speed. Samples were prepared with a 5 nm ultra-thin hematite film overlay on the mWO$_3$ films composed of spheroids with different size distributions. A significant contribution of hematite to the photocurrent was observed when coated on the light trapping mWO$_3$ spheroids whereas no photocurrent could be measured with the same hematite ultra-thin film coated on bare FTO glass. Tuning the spheroids sizes allowed an in depth study of the impact of this microstructure change on the overall photoanode photocurrent. We observed that the contribution of hematite is increased while the contribution of mWO$_3$ is decreased when decreasing the spheroid sizes.

    In the next chapter I focus on the optical properties of the photoanode composed of

microspheroids. Indeed this microstructure show a strong photonic response in the far field meaning that light interacts significantly with the spheroids. We will see how the different photonic regimes obtained when changing the spheroid sizes impact light absorption in these films and relate with the PE trends described in this chapter.

References

1. ⌕. Diane K. Zhong, Maurin Cornuz, Kevin Sivula, Michael Grätzel, and Daniel R. Gamelin. Photo-assisted electrodeposition of cobalt-phosphate (Co-Pi) catalyst on hematite photoanodes for solar water oxidation. *Energy & Environmental Science*, 4 (5):1759–1764, May 2011.

2. ⌕. Renata Solarska, Rafal Jurczakowski, and Jan Augustynski. A highly stable, efficient visible-light driven water photoelectrolysis system using a nanocrystalline WO$_3$ photoanode and a methane sulfonic acid electrolyte. *Nanoscale*, 4(5):1553–1556, 2012.

3. ⌕. Aiming Mao, Jung Kyu Kim, Kahee Shin, Dong Hwan Wang, Pill J. Yoo, Gui Young Han, and Jong Hyeok Park. Hematite modified tungsten trioxide nanoparticle photoanode for solar water oxidation. *Journal of Power Sources*, 210:32–37, July 2012.

4. ⌕. Heli Wang, Todd Deutsch, and John A. Turner. Direct water splitting under visible light with nanostructured hematite and WO$_3$ photoanodes and a GaInP$_2$ photocathode. *Journal of the Electrochemical Society*, 155(5):F91–F96, 2008.

5. ⌕. Coleman X. Kronawitter, Lionel Vayssieres, Shaohua Shen, Leijin Guo, Damon A. Wheeler, Jin Z. Zhang, Bonnie R. Antoun, and Samuel S. Mao. A perspective on solar-driven water splitting with all-oxide hetero-nanostructures. *Energy & Environmental Science*, 4(10):3889–3899, October 2011.

6. ⌕. Kevin Sivula, Florian Le Formal, and Michael Grätzel. WO$_3$-Fe$_2$O$_3$ Photoanodes for Water Splitting: A Host Scaffold, Guest Absorber Approach. *Chemistry of Materials*, 21 (13):2862–2867, July 2009.

7. ⌕. J. H. Kennedy and K. W. Frese. Photo-oxidation of Water At α-Fe$_2$O$_3$ Electrodes. *Journal of the Electrochemical Society*, 125(5):709–714, 1978.

8. ⎘. Florian Le Formal, Kevin Sivula, and Michael Grätzel. The Transient Photocurrent and Photovoltage Behavior of a Hematite Photoanode under Working Conditions and the Influence of Surface Treatments. *Journal of Physical Chemistry C*, 116(51):26707–26720, December 2012.

9. ⎘. L. A. Marusak, R. Messier, and W. B. White. Optical-absorption Spectrum of Hematite, α-Fe$_2$O$_3$ Near IR To UV. *Journal of Physics and Chemistry of Solids*, 41 (9):981–984, 1980.

10. ⎘. C. Sanchez, K. D. Sieber, and G. A. Somorajai. The Photoelectrochemistry of Niobium Doped Alpha-fe2(03). *Journal of Electroanalytical Chemistry*, 252(2):269–290, October 1988.

11. ⎘. S. M. Wilhelm, K. S. Yun, L. W. Ballenger, and N. Hackermann. Semiconductor Properties of Iron-oxide Electrodes. *Journal of the Electrochemical Society*, 126(3):419–424, 1979.

Chapter 4

Light Trapping Properties of the all-oxide Microspheroids

In this chapter we will see that the spheroid microstructure shows a strong interaction with light at visible wavelengths. A theoretical study of this photonic response allowed us to understand the interaction of light with the microstructure and showed that microspheroids can trap visible light through different photonic processes. The prevalence of different photonic regimes when changing the spheroids size is shifting the localization of light inside the film. I will determine how these different regimes impact light absorption inside the photoanode and can explain the photoelectrochemical behaviors described in the previous chapter.

4.1   Introduction

Light trapping strategies were developed recently to increase light absorption in thin hematite films[1,2]. Dotan et al.[1] used reflecting coatings and took advantage of resonant light trapping using multiple reflections in a flat hematite film on a reflective surface. Gao et al.[2] used nanostructured gold films to obtain both surface plasmons and light trapping effects. In the present case our hematite coated mWO_3 spheroids can combine light management and the production of an all-oxide heterojunction.

Dielectric spheroids of near wavelength dimensions are known to support confined resonant modes[3–5]. mWO_3 is a material of choice in order to confine light, since it possesses a high

refractive index for visible light wavelengths (2.2 to 3.7 for crystalline mWO$_3$[6]) and provide a strong refractive index contrast compared to the ambient medium, which in the present case is an aqueous electrolyte. By coating these mWO$_3$ spheroids with an ultra-thin hematite film, a semiconductor heterojunction is achieved and charge carrier recollection is enhanced. At the same time the interaction of light with the microstructure allows to decouple light absorption and thickness of the hematite film.

We have seen in the precedent chapter that this strategy has successfully enhanced the obtained photocurrents densities compared to a non-microstructured film. In the present chapter I will elucidate the photonic effects at the origin of this improvement.

4.2   Materials and methods

4.2.1   Ultraviolet-visible (UV-vis) transmission spectroscopy

Transmission spectroscopy was performed using a Varian Carry® 50 UV-vis spectrometer. The samples were held with the substrate facing the detector and the film facing the laser probe and was oriented orthogonally to the beam direction. The spectra were recorded between 300 and 800 nm with a step of around 1nm.

4.2.2   Finite-difference time-domain simulations

A commercial-grade simulator based on the Finite-Difference Time-Domain (FDTD) method was used to perform the calculations[7]. One model was created for each spin coating speed. Each model involves 67 oblate coated spheroids with a diameter distribution derived from image processing on SEM images. The mean distance and height of the spheroids was obtained by image processing on SEM images and AFM scans respectively. The spheroids were displayed to form a periodic triangular array respecting the experimental mean spheroid distance. Perfectly matched layers, parallel to the modeled film surface, were used before and after the film. The refractive index of the medium was given a value of 1.33 (water), the refractive index for mWO$_3$ was obtained from Hutchins et al.[6] and the refractive index for hematite was obtained from the University of Waterloo online database[8].

4.3   Results and discussion

It appears that the light trapping function of our films is closely related to their microstructure. A strong attenuation peak was observed in absorption spectroscopy experiments (fig. 4.1 b.) for all screened spheroid sizes (fig. 4.1 a.). This peak position is strongly influenced by the characteristic dimensions of the coated spheroids. These features could not be attributed to the chemical composition of the films, since they do not emerge from the absorption of hematite or mWO_3 but rather from the interaction of light with the microstructure. These attenuation peaks are related to diffraction phenomena, and far field scattering patterns (not shown here) shows photonic jets forming at wavelengths where the absorption peaks are significant. Tuning the spheroids size distribution allows to tune the wavelength range of this light interaction with the microstructure, with a shift of the attenuation feature to shorter wavelengths when decreasing the spheroid sizes.
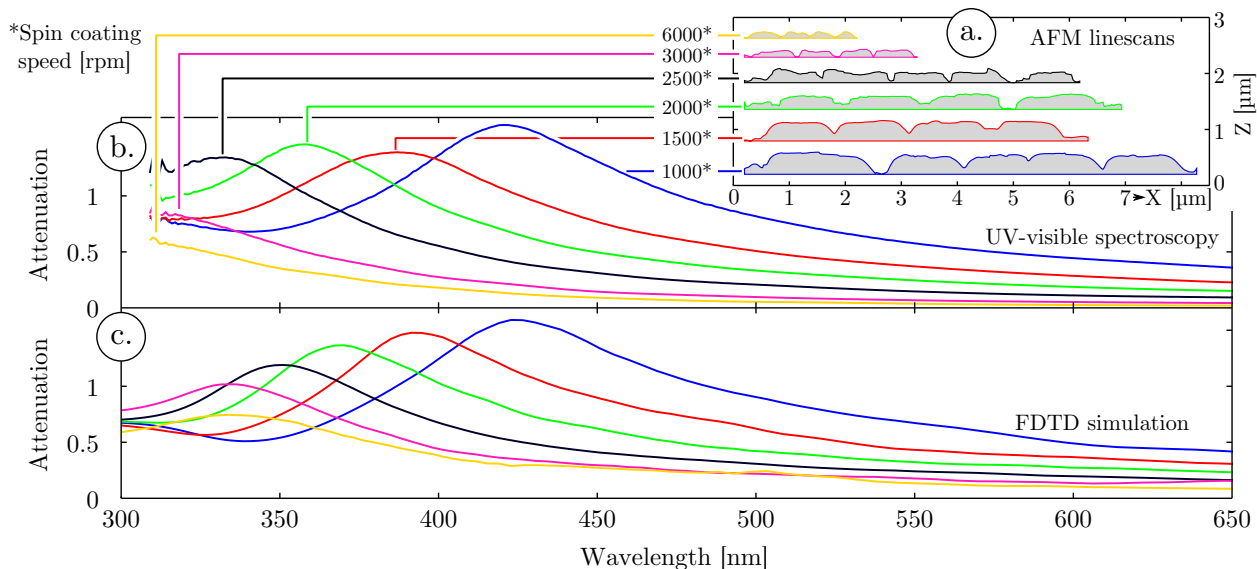

Figure 4.1: Correlation between the tungsten oxide microstructure and the far field scattering attenuation peak of the mWO_3 films composed of spheroids, processed at different spin coating speeds: a. AFM line scans of the surfaces; b. UV-vis absorption spectroscopy performed in water on the different films; c. Simulated attenuation spectra using the FDTD method.

In order to understand how the light behaves for these different regimes and to see whether light trapping can be achieved in such microstructures, numerical simulations were performed. Specifically, the distribution of the electric field inside the spheroids upon simulated solar light illumination was mathematically modeled. A commercial-grade simulator based on the

finite-difference time-domain method was used to perform the calculations[7]. The films microstructure was modeled by oblate coated spheroids with height and diameter representative of the size distributions obtained by SEM and AFM image processing.
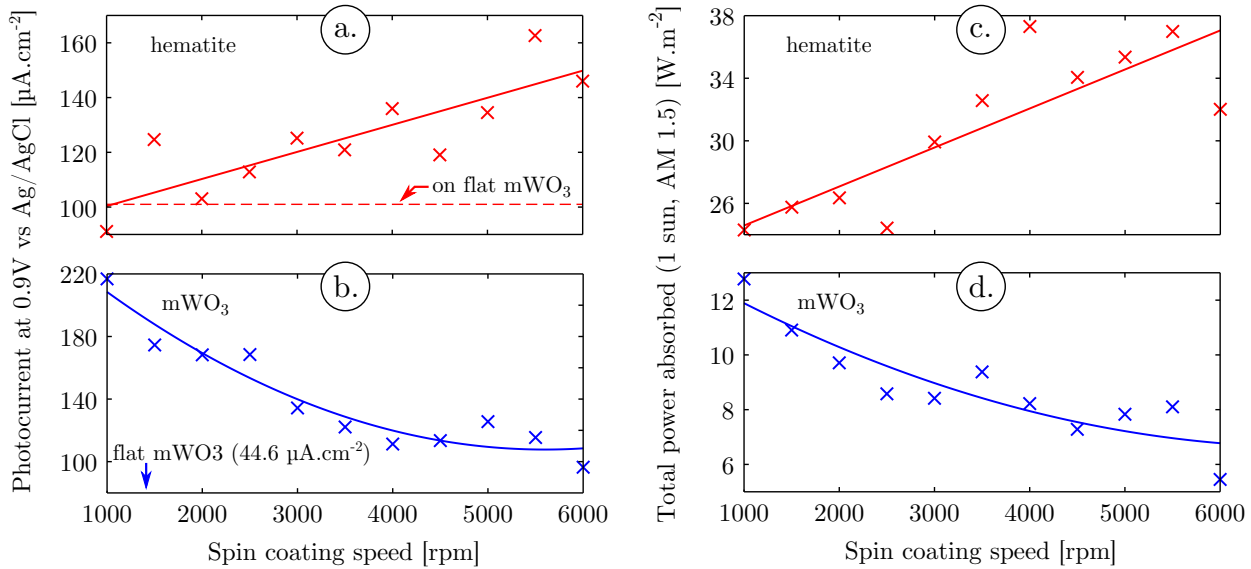

Figure 4.2: Photocurrent densities at 0.9V vs Ag/AgCl (current density under illumination - dark current density) as a function of the spin coating speed. Contributions from: a. hematite; and b. mWO$_3$ (see chapter 3). Calculated total power absorbed under simulated solar light conditions in: c. hematite; and d. mWO$_3$

In order to validate the microstructure modelization, far field projections of the electric field were calculated and simulated attenuation spectra were obtained for each microstructure (fig. 4.1 c.). When comparing simulated and experimental attenuation spectra a quantitative match is observed between the attenuation peak position and width, due to scattering, for each microstructure. Therefore the model implemented in the simulation is representative of the experimental conditions and can be used to gain quantitative understanding of the light / microstructure interaction. Moreover FDTD simulation is based on classical electrodynamic and is neglecting quantum size effects. Therefore the close match between simulation and experiments proves that the attenuation peak observed experimentally, as well as the blue shift of this peak when decreasing the microspheroids dimensions is a consequence of the film microstructure, and possible quantum size effects on light absorption can be neglected. The electric field distributions inside hematite and mWO$_3$ were obtained from the simulation. It is therefore possible to integrate the electric field inside hematite and mWO$_3$ and calculate the power absorbed in each materials using the divergence of the Poynting vector:

$$P_{abs} = -0.5\,\omega\,|E|^2\,k \qquad (4.1)$$

with ω the angular velocity, E the electric field, and k the imaginary part of the refractive index. By integrating the power absorbed over the wavelength range between 300 and 800 nm, taking into account the irradiance of 1 sun at AM 1.5, the total power absorbed in each oxide under simulated solar conditions has been obtained for the different microstructures (fig. 4.2 c. and d.). As shown in fig. 4.2 c. and d., when decreasing the spheroid sizes (increasing the spin coating speed), the power absorbed in hematite is increased while the power absorbed in mWO$_3$ is decreased. These tendencies can be explained by changes in the interaction of light with the film depending on the spheroid size distribution.

In order to explain the origin of this shift I performed a series of near-field simulations of the electric field distribution as a function of the microspheroid size and light wavelength (fig. 4.3). In these simulations only one spheroid is considered, with a radius determined by the mean radius obtained experimentally for three different spin coating speeds. Two photonic regimes are observed as a function of the relationship between the spheroid dimensions and the incoming light wavelength. In the first regime, light wavelength is smaller than the spheroid radius and strong resonant modes are observed while near-field scattering is weak. In the second regime, light wavelength is equivalent to the spheroid radius, the resonant modes intensity is decreased while the scattered field intensity increases. This explains why light confinement is shifting from mWO$_3$ to hematite when decreasing the spheroid sizes. When spheroids sizes are decreased, the confined modes intensities are decreased inside the spheroids while light is scattered more efficiently concen-
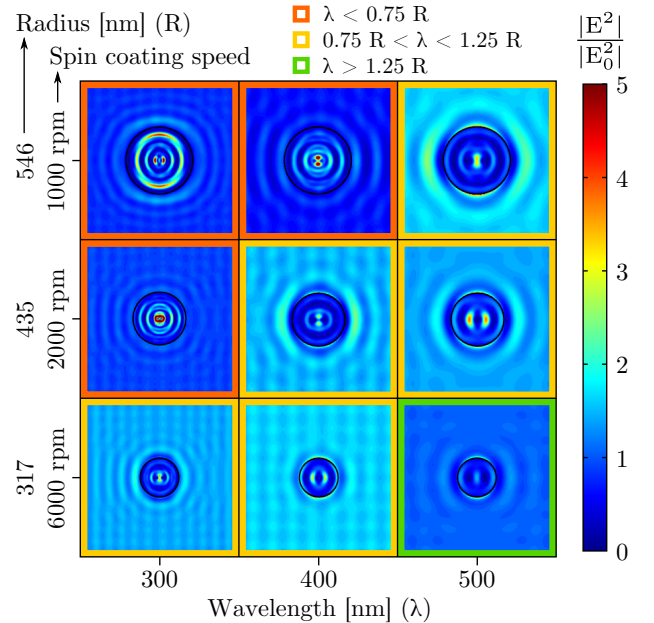

Figure 4.3: Optical intensity distribution in the near-field as a function of spheroid size for different incident light wavelengths. The simulations where light wavelength is lower than the spheroid radius (λ< 0.75 R) are highlighted with a red frame and the simulations where light wavelength is comparable to the spheroid radius (0.75 R < λ< 1.25 R) are highlighted with a yellow frame.

trated between and at the surface of the spheroids.

4.4   Conclusions

Tuning the structures sizes allowed an in depth study of the impact of the light/microstructure interaction on the overall photoanode photocurrent. Simulation of the photonic effects inside the microstructure, using an oblate coated spheroids modelization, quantitatively matched experimental results and allowed to calculate the power absorbed by each oxide. The variations in simulated power absorbed showed a strong correlation with the photocurrent. It is therefore possible that light trapping effects inside the spheroids have a strong influence on hematite and mWO_3 photoactivities, with photocurrent values ranging from single to double depending on the spheroid sizes.

It is worth noting that the variations in simulated power absorbed / photoactivity is decreasing in mWO_3, whereas it is increasing in hematite when the spheroid sizes is decreasing. Light is concentrated toward the surface of the spheroids when the spheroids size is decreasing and a compromise therefore needs to be achieved using spheroid sizes in the middle of the screened dimensions range (spin coating speed: 2500-3000 rpm, spheroid height $\approx$ 250 nm and diameter $\approx$ 750 nm).

Taking advantage of the same self-assembly technique, a possible outlook of this study would be the implementation of more complex microstructures. The present study was focused on a monolayer of mWO_3 spheroids but multiple vesicle layers can be coated on the substrate. Preliminary results already show that it is possible to obtain such mWO_3 films with micrometric light scattering centers displayed on multiple layers. This would allow to take advantage of more photonic effects, such as near field focusing that is another photonic feature of oblate spheroids[9], and also an increase of the photoanode surface and thickness. Nevertheless the produced multilayered films were showing a decrease in photocurrent compared to the films composed of a single layer. Maybe the charge conduction length is inhibiting current collection in these thicker films.

References

1. ⌖. Hen Dotan, Ofer Kfir, Elad Sharlin, Oshri Blank, Moran Gross, Irina Dumchin, Guy Ankonina, and Avner Rothschild. Resonant light trapping in ultrathin films for water splitting. *Nature Materials*, 12(2):158–164, February 2013.

2. ⌖. Hanwei Gao, Chong Liu, Hoon Eui Jeong, and Peidong Yang. Plasmon-Enhanced Photocatalytic Activity of Iron Oxide on Gold Nanopillars. *Acs Nano*, 6(1):234–240, January 2012.

3. ⌖. Jonathan Grandidier, Raymond A. Weitekamp, Michael G. Deceglie, Dennis M. Callahan, Corsin Battaglia, Colton R. Bukowsky, Christophe Ballif, Robert H. Grubbs, and Harry A. Atwater. Solar cell efficiency enhancement via light trapping in printable resonant dielectric nanosphere arrays. *Physica Status Solidi A-applications and Materials Science*, 210(2):255–260, February 2013.

4. ⌖. Jonathan Grandidier, Dennis M. Callahan, Jeremy N. Munday, and Harry A. Atwater. Light Absorption Enhancement in Thin-Film Solar Cells Using Whispering Gallery Modes in Dielectric Nanospheres. *Advanced Materials*, 23(10):1272–1276, March 2011.

5. ⌖. Y. N. Xia, B. Gates, Y. D. Yin, and Y. Lu. Monodispersed colloidal spheres: Old materials with new applications. *Advanced Materials*, 12(10):693–713, 2000.

6. ⌖. M. G. Hutchins, O. Abu-Alkhair, M. M. El-Nahass, and K. A. El-Hady. Structural and optical characterisation of thermally evaporated tungsten trioxide (WO_3) thin films. *Materials Chemistry and Physics*, 98(2-3):401–405, August 2006.

7. ⌖. Lumerical Solutions, Inc.

8. ⌖. Natural Phenomena Simulation Group, University of Waterloo.

9. ⌖. Manuel J. Mendes, Ignacio Tobias, Antonio Marti, and Antonio Luque. Light concentration in the near-field of dielectric spheroidal particles with mesoscopic sizes. *Optics Express*, 19(17):16207–16222, August 2011.

Chapter 5

Electrohydrodynamic lithography

In this chapter I will present an alternative structuration technique that was also investigated during this thesis, namely EHL. We have seen that tailoring hematite thin film nanostructure is particularly interesting since this oxide's function is closely related to its structure when implemented as a photoanode in water splitting solar cells. In this study, electrohydrodynamic destabilization was designed to grow hematite nanodroplets with morphologies controlled by a master electrode. A polymer/iron salt film was destabilized by electrohydrodynamic destabilization and the resulting structures were pyrolysed to achieve crystalline α-Fe$_2$O$_3$ nanodroplets of 30 nm height and 70 nm radius. NEXAFS spectroscopy proved that the structures contain ferrihydrite, which is converted into hematite during pyrolysis, while the polymer was decomposed. Homogeneous nanoparticle precipitation in the bulk of the polymer, due to encapsulation of the iron precursor in the polymer matrix, is accounted for the good preservation of the structures. This study represents the first step towards the use of electrohydrodynamic destabilization for nanostructuring of hematite thin films, with a control over the feature size.

5.1   Introduction

Metal oxide thin films based on nanopillar array have been suggested as efficient photoanode systems for solar water splitting and hydrogen fuel generation in photo-electrochemical

cells[1].Iron oxides such as α-Fe$_2$O$_3$ (hematite) are low-cost, environmentally benign and abundant semiconductors for use as such photoanodes. But hematite has the major disadvantage that its optical thickness is large (118 nm at λ=550 nm)[2] compared to its charge carrier recombination length (2-4 nm)[3]. To overcome this drawback, various approaches for micro- or nano-structuring of iron oxide into nanopillar, nanorod and nanotube arrays, for example by aqueous chemical growth[4] or anodization[5,6] have been investigated. Here I present a novel and simple method of obtaining iron oxide structures, taking advantage of the self-organisation occurring in molten polymers subjected to an external electric field. This phenomenon is known as electrohydrodynamic destabilization (EHD) and has been previously used to tailor micrometric droplets or pillar arrays[7,8]. The polymer structures obtained by Heier et al.[9], with spatially modulated electric fields, show that the sizes and aspect ratios obtained can be controlled using parameters such as the electric field strength and the lateral field modulation. The control provided by such heterogeneous electric fields has been exploited by Schaffer et al.[10] to achieve features with lateral dimensions down to 140 nm using a structured electrode. Moreover this electrolithographic phenomenon is a determining factor in the upscaling of the destabilized region[11]. The use of this technique to oxide films has been initiated by Voicu et al.[12]. They destabilized titanium alkoxide-alcohol solutions and obtained micrometric TiO$_2$ patterns. To the best of our knowledge no other attempt has been made to use EHD to structure inorganic materials. Our study focuses on the development of electrohydrodynamic destabilization for the high-fidelity conversion of polymer/iron salt structures obtained by EHD destabilization into hematite (α-Fe$_2$O$_3$) structures. The strategy adopted is to encapsulate an iron salt in a polymer thin film and then tailor the polymer structure using EHD. After structuring, the film is pyrolysed at 500°C in an air vented furnace to decompose the polymer matrix, whilst at the same time converting the iron to hematite.

5.2 Materials and methods

The thin film for destabilization was spin-coated from an aqueous solution on a silicon wafer. This solution was prepared by mixing 0.5M in pyridyl groups of Poly(4-vinylpyridine) (P4VP) (Mw $\approx$ 60,000, Sigma Aldrich) and 0.5M of FeCl$_3$ (reagent grade, 97% anhydrous, Sigma Aldrich) in double deionized water, leading to a 1:1 molar ratio between pyridyl groups and aqueous iron chloride. The resulting aqueous solution is acidic with a pH of 1.5. The spin coating was realized using a Primus STT15 spin-coater from ATMvision AG, with a holding

time of 60 seconds at a spinning speed of 6000 rpm which was reached within 2 seconds. After spin-coating, the thin film was air-dried at room temperature for at least 2 days. The resulting film has a thickness of 180-200 nm (profilometer), and is flat with only nanometer scale roughness (Fig. 5.1 a.).

This film was then melted under an electric field, facing a nanostructured aluminium electrode (Fig. 5.1 b. and c.). The nanostructured electrode acts as a master electrode and controls the size of the features developing at the surface of the polymer film. Since the present study is focused on controlling the size of the hematite structures, no attempts has been made to use a master electrode possessing an organized pattern as in the study of Voicu et al.[12]. The electrode nanostructure is obtained by evaporating aluminium in vacuum onto a silicon substrate. Aluminum evaporation pellets, 99.9996% pure, were thermally evaporated using a Univex 300 thermal evaporator from Oerlikon Leybold Vacuum. Arslan et al.[13] showed that vapour phase aluminium deposited on a silicon oxide surface followed with high fidelity the droplet deposition and

Figure 5.1: The two adjacent electrodes used for thin film destabilization. $5\times5\mu m$ AFM scan of: a. P4VP/FeCl$_3$ thin film surface before destabilization, b. nanostructured aluminium thin film as obtained by evaporation (master electrode), c. Size distribution of the master electrode features

coalescence model described by Family and Meakin[14] and obtained aluminium islands of nanometric dimensions after less than 2 minutes deposition. In the present study, the master electrode contains ten times larger droplets than the clusters obtained by Arslan. Since the droplet growth follows the Family and Meakin model, this difference is accounted for the longer deposition time (15-20 minutes), leading to more material coalescence and therefore larger features.

An air gap of less than 140-160 nm separated the polymer film surface and the master electrode. In order to maintain this submicrometric gap, SU8-2000 photoresist was spin coated, developed and etched on the master electrode surface to obtain a spacer. The wafers were then contacted and pressed together (see annex 6, chapter 6). The entire assembly was placed
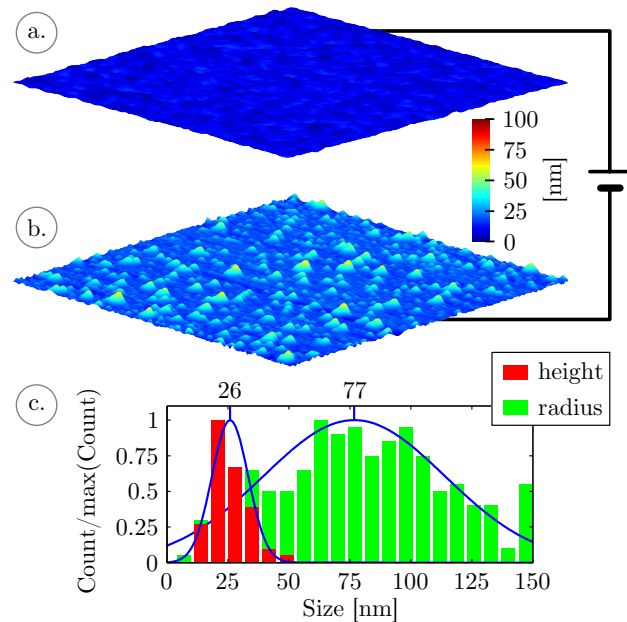
in an oven for 3 hours at 180°C and 0.01 mbar vacuum with a bias of 50 V applied to the wafers.The heating temperature of 180°C was chosen to melt the P4VP film, which has a glass transition temperature in the range 140-150°C[15,16]. After heating, the assembly was cooled to room temperature while maintaining the 50 Volt bias. After destabilization the films were heated in an air vented furnace at 500°C for 2 hours, using a heating ramp of $5°C.min^{-1}$.

5.3 Results and discussion

The destabilization of the P4VP/FeCl$_3$ thin film results in the formation of two different kinds of features: oblate droplets with sub-micrometer size, and droplets with nanometer size (Fig. 5.2 a.). Using complementary Matlab and Fiji procedures (see annex 6, chapter 6) the nanometric distribution has been mathematically separated from the submicrometric distribution by using a high pass filter (Fig. 5.2 and 5.3). The size distribution of the nanometric features (Fig. 5.2 b.) and of the master electrode (Fig. 5.1 c.) match quantitatively. Therefore, the nanometric droplets observed on the thin film surface most likely originate from heterogeneities in the electric field[9]. Where a feature of the master electrode is present the air gap is smaller, leading to a local enhancement of the electric field in the film. The electrostatically induced pressure is higher on the melted film surface in the regions facing a feature of the electrode, and the film surface replicates the electrode features. Since the mean height of the master electrode features is 26 nm and the air gap is in the 140-160 nm range, the increase in electrostatic pressure where a feature of the master electrode is present is in the range of 12 to 14%. In contrast, the sub-micrometric droplets originate from the average electric field. Indeed their order of magnitude matches the typical micrometer scale features obtained using homogeneous electric field for thin polymer film destabilization[7,8]. Although larger homogeneous electric field leads to smaller features, the minimum size that these features can reach is limited by viscous effects[17].

To convert this polymeric structure into an oxide, the film was pyrolysed at 500°C in air. This thermal oxidative treatment allows precipitation and pyrolysis of iron oxide inside the film, whilst simultaneously decomposing the polymer matrix. The film features are well preserved after pyrolysis (Fig. 5.3). Their shrinkage is not homogeneous; the radius distribution is almost invariant, while the height distribution significantly decreases. The calculated

shrinkage for the submicrometric and nanometric height distributions are 32% and 36% respectively.
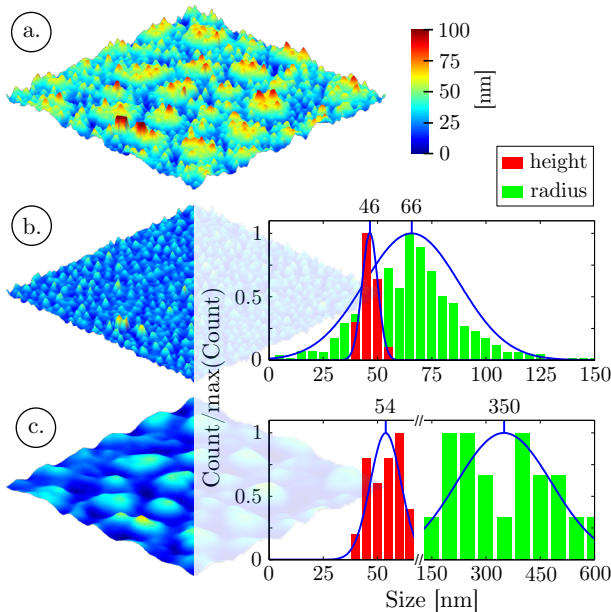

Figure 5.2: a. 5×5 µm AFM scan of the film surface after electrostatic destabilization (50V), b. high frequency features and their size distribution, c. low frequency features and their size distribution.
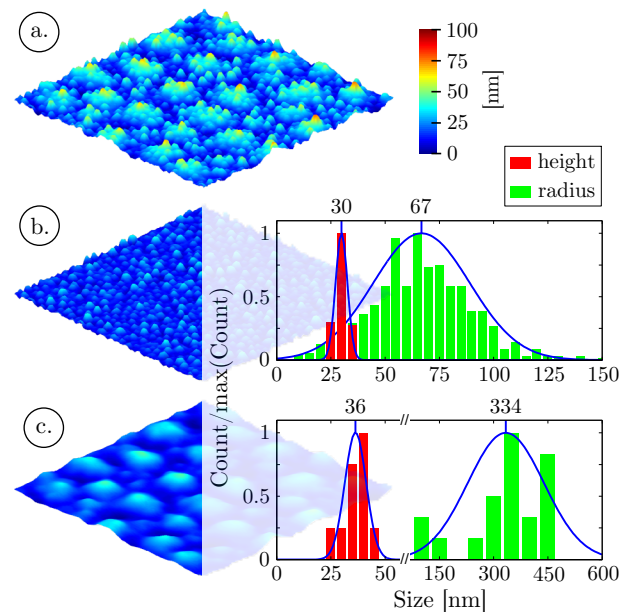
Figure 5.3: a. 5×5 µm AFM scan of the electrostatic destabilized film surface after pyrolysis at 500°C in air, b. high frequency features and their size distribution, c. low frequency features and their size distribution.

The resultant film consists of a homogeneously distributed structure of nanometric particles, around 30 nm in diameter (Fig. 5.4) and I propose that the iron chloride is homogeneously distributed within the pristine P4VP/FeCl$_3$ thin film and evolves into nanoparticles during the pyrolysis. The homogeneous nanoparticle precipitation in the bulk of the polymer accounts for the low shrinkage of the features.

In order to analyse the molecular structure of the thin film before and after pyrolysis (on 5 × 5 mm silicon wafers), near edge X-ray absorption fine structure (NEXAFS) spectroscopy measurements have been carried out at the experimental station SurICat, Optics beamline at BESSY-II, Helmholtz Zentrum Berlin. NEXAFS spectra provide distinctive features that are characteristic of the structure and bonding environment of an atom[18]. The screened energies correspond to the nitrogen K-edge (395 eV to 403 eV), the oxygen K-edge (520 eV to 560 eV) and the iron L-edge (700 eV to 730 eV). Excitation at the nitrogen edge is expected to correspond to an excitation of the nitrogen from the pyridine groups of the polymer, and excitation at the iron and oxygen edges have been chosen in order to identify iron oxide phases. These NEXAFS spectra were recorded using the Total Electron Yield (TEY) technique, by
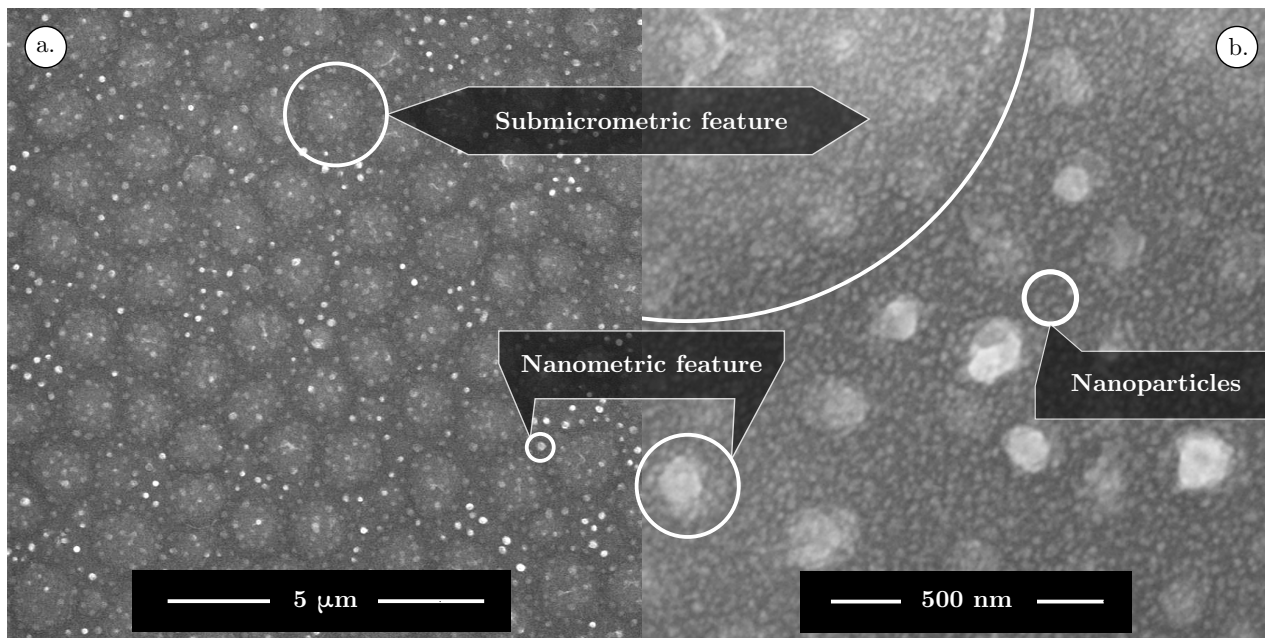
Figure 5.4: Scanning electron micrograph of the pyrolysed film, a. top view of the film surface, b. tilted view of the film surface.

measuring the current drain to ground normalized to the incident photon flux. The sampling depth in TEY measurements probes mostly the surface and sub-surface of the samples. The energy resolution is 66 meV at 400 eV. NEXAFS measurements at the nitrogen K-edge of samples prior to pyrolysis present two prominent spectral features at 398.6 eV and 400.0 eV (Fig. 5.5) corresponding to the transition from the 1s atomic nitrogen orbital to the π^* molecular orbitals of the pyridine. The presence of two features prior to pyrolysis, with a shift of around 1.4 eV probably corresponds to partial protonation of the P4VP nitrogen. Pease and Russel[17] recorded NEXAFS spectra at the nitrogen edge of both neutral and fully protonated P4VP and obtained peaks at 398.9 eV and 400.4 eV for the neutral form and protonated form respectively. The same shift of 1.5 eV between protonated and neutral nitrogen has also been observed in polyaniline samples by Hennig et al.[19]. The partial protonation of the polymer can be linked to the low pH (1.5) of the aqueous solution used for the spin coating of these films. This partial protonation could lead to the separation of the polymer into hydrophilic (protonated) and hydrophobic (neutral) regions and Millan et al.[20,21] have studied P4VP/iron hydroxide nanocomposites proposing that hydrophilic regions encapsulate the iron ions. When the iron ions precipitate, this encapsulation allows the stabilization of iron nanoparticles within the bulk of the polymer.

It should be noted that Millan et al. [20] in-
duced deprotonation of PVP compounds by
addition of NaOH and observed deprotona-
tion onset at pH = 3.0.   In our case no
NaOH was added to the solutions before cast-
ing and the solution pH was 1.5. It is there-
fore possible that the observed deprotonation
of P4VP in our films is not occurring in so-
lution but upon spin coating of the polymer.
After pyrolysis, no pyridine nitrogen K-edge
peaks are observed, providing strong evidence
that the polymer is fully combusted. Simi-
lar results have been obtained by Elmaci and
Hacaloglu [23] for P4VP homopolymers.

NEXAFS spectra obtained at the Fe L-
edge show multiplet peaks corresponding to
the transition from the 2p to the 3d orbitals

Figure 5.5: Nitrogen K-edge spectra of a P4VP/FeCl$_3$
thin film before and after pyrolysis in air at 500°C
(blue curves). The red curve correspond to neutral
P4VP and the green curve to fully protonated P4VP
as measured by Fujii et al. [22] (reproduced with per-
mission of the authors).

(Fig. 5.6). Two sets of features can be observed, one in the L3 region (705-717 eV) and
one in the L2 region (717-725 eV). For ease of spectral assignment, the spectra have been
deconvoluted. The doublet observed in each region arises from the splitting of the 3d orbital
of iron into two degenerate orbitals with e_g and t_{2g} symmetry due to the spin orbit cou-
pling. Close inspection of the L3 peak at around 708 eV shows noticeable differences between
the pre-pyrolysis and the post-pyrolysis samples. In the post-pyrolysis sample, the peak is
sharper, with well-defined e_g and t_{2g} features with a width of around 1.2 eV. Spectra of iron
oxide compounds with different structures containing Fe(III) have been studied by Peak and
Regier [24] who observed that the presence of tetrahedral coordinated Fe(III) in compounds
with predominantly octahedral coordinated Fe(III) tends to broaden the L3 peak, because the
tetrahedral and the octahedral forms show proximate but not identical main peak positions.
This suggests that our pre-pyrolysis sample does not yet fully constitute an iron oxide with
octahedral Fe(III) centres, but still contains a significant amount of iron in a non-octahedral
coordination geometry, which could be interpreted as presence of oxygen vacancies. In con-
trast, post-pyrolysis samples contain predominantly octahedral Fe(III) centres.

The O K-edge spectra also give relevant information about the structure. The pre-pyrolysis
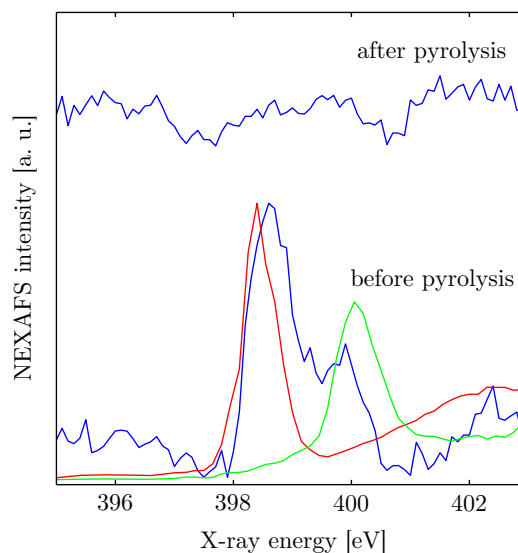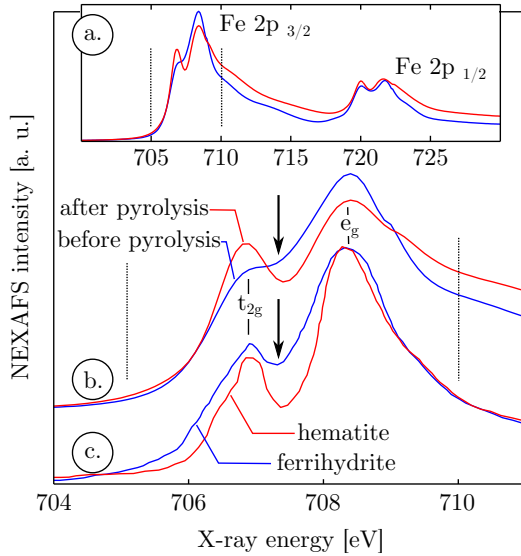
Figure 5.6: a. Fe L-edge spectra of a P4VP/FeCl$_3$ thin film before (blue curve) and after pyrolysis at 500°C (red curve). b. Fe 2p $_{3/2}$ region before (blue curve) and after pyrolysis (red curve). c. Fe 2p $_{3/2}$ region for ferrihydrite (blue curve) and hematite (red curve), reproduced from [24].
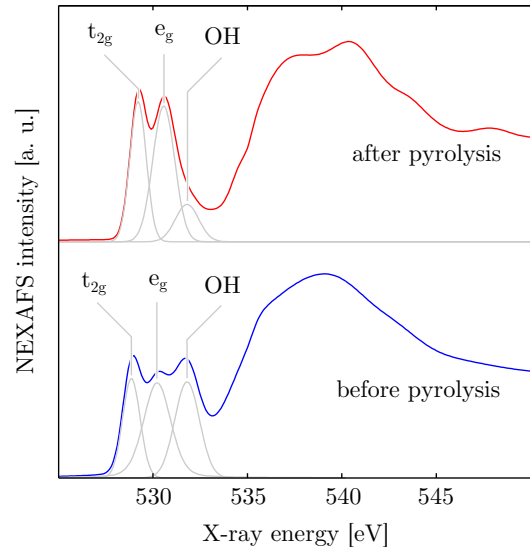
Figure 5.7: O K-edge spectra of a P4VP/FeCl$_3$ thin film before (bottom) and after pyrolysis at 500°C (top).

samples show a set of three peaks in the pre-edge region while the post-pyrolysis sample shows only two (Fig. 5.7). The peaks at 528.9 eV and 530.2 eV correspond to the transitions from the O 1s levels of O 2p to the Fe e_g and t_{2g} orbitals and the highest energy peak at 531.6 eV, which is only present before pyrolysis, has previously been observed in goethite samples by Todd et al.[25] and assigned to the transition from the O 1s levels of OH$^-$ to the Fe 3d orbitals.

To summarise the Fe L-edge and O K-edge NEXAFS data, pre-pyrolysis samples contain both tetrahedral and octahedral Fe(III) centres indicating that the iron does not initially precipitate in an akaganèite form, as in the P4VP/akaganèite nanocomposite material only containing octahedral centres obtained by Millan et al.[21] . Oxidic structures containing both tetrahedral and octahedral Fe(III) centres include ferrihydrite (Fe$_2$O$_3$.1/2H$_2$O) or maghemite (γ-Fe$_2$O$_3$). The O K-edge spectra further refine this structural elucidation and the strong peak observed at around 532 eV prior to pyrolysis is characteristic of an -OH group supporting the initial precipitation of ferrihydrite rather than maghemite. After pyrolysis, the Fe L-edge and O K-edge spectra perfectly match the spectra reported for hematite[24–26]. These data indicate that after spin-coating the aqueous FeCl$_3$ precipitates into ferrihydrite which is converted into hematite upon pyrolysis.

5.4   Conclusions

This study shows that it is possible to destabilize thin polymer films loaded with an iron containing precursor. Self-organized nanostructures may be grown by means of a master nanostructured master electrode. After the electric field assisted self-organization, the film can be pyrolised, allowing the simultaneous combustion of the polymer and conversion of the iron into hematite. This chemical conversion is achieved with conservation of the nanostructure. These results are promising and introduce a methodology for the conversion of polymer-stabilized nanostructures to metal oxides nanostructures. The control offered by this technique on hematite structure opens the way to comprehensive studies of the nanostructure influence on the photoelectrochemical behavior of this material. Using this technique, even complex architectures involving oxides heterojunction could be developed, based on the destabilization of multilayered thin films established by Morariu et al.[27].

Despite the successful implementation of this electrohydrodynamic lithography method to structure hematite no photoelectrochemical activity could be measured using a conventional photoelectrochemical setup with these films. This lack of photoelectrochemical activity can stem from a simple technical issue. The silicon wafer conductivity is low compared to the typical conductive transparent substrates used in photoelectrochemical water splitting studies. These kinds of substrates could not be implemented in this study since they are not atomically flat and resulted in electric spark and a discharge of the film surface, preventing its destabilization.

References

1. ⎘. B. M. Kayes, H. A. Atwater, and N. S. Lewis. Comparison of the device physics principles of planar and radial p-n junction nanorod solar cells. *Journal of Applied Physics*, 97(11):114302, June 2005.

2. ⎘. I. Balberg and H. L. Pinch. Optical-absorption of Iron-oxides. *Journal of Magnetism and Magnetic Materials*, 7(1-4):12–15, 1978.

3. ⎘. J. H. Kennedy and K. W. Frese. Photo-oxidation of Water At α-Fe$_2$O$_3$ Electrodes. *Journal of the Electrochemical Society*, 125(5):709–714, 1978.

4. ⬀. Coleman X. Kronawitter, Lionel Vayssieres, Shaohua Shen, Leijin Guo, Damon A. Wheeler, Jin Z. Zhang, Bonnie R. Antoun, and Samuel S. Mao. A perspective on solar-driven water splitting with all-oxide hetero-nanostructures. *Energy & Environmental Science*, 4(10):3889–3899, October 2011.

5. ⬀. R. R. Rangaraju, A. Panday, K. S. Raja, and M. Misra. Nanostructured anodic iron oxide film as photoanode for water oxidation. *Journal of Physics D-applied Physics*, 42 (13):135303, July 2009.

6. ⬀. Keyu Xie, Jie Li, Yanqing Lai, Wei Lu, Zhi'an Zhang, Yexiang Liu, Limin Zhou, and Haitao Huang. Highly ordered iron oxide nanotube arrays as electrodes for electrochemical energy storage. *Electrochemistry Communications*, 13(6):657–660, June 2011.

7. ⬀. Nicoleta E. Voicu, Sabine Ludwigs, and Ullrich Steiner. Alignment of lamellar block copolymers via electrohydrodynamic-driven micropatterning. *Advanced Materials*, 20(16): 3022–3027, August 2008.

8. ⬀. Pola Goldberg-Oppenheimer, Sumeet Mahajan, and Ullrich Steiner. Hierarchical Electrohydrodynamic Structures for Surface-Enhanced Raman Scattering. *Advanced Materials*, 24(23):OP175–OP180, June 2012.

9. ⬀. Jakob Heier, Jan Groenewold, and Ullrich Steiner. Pattern formation in thin polymer films by spatially modulated electric fields. *Soft Matter*, 5(20):3997–4005, 2009.

10. ⬀. E. Schaffer, T. Thurn-Albrecht, T. P. Russell, and U. Steiner. Electrically induced structure formation and pattern transfer. *Nature*, 403(6772):874–877, February 2000.

11. ⬀. Ning Wu, III Pease, Leonard F., and William B. Russel. Toward large-scale alignment of electrohydrodynamic patterning of thin polymer films. *Advanced Functional Materials*, 16(15):1992–1999, October 2006.

12. ⬀. Nicoleta E. Voicu, M. S. M. Saifullah, K. R. V. Subramanian, Mark E. Welland, and Ullrich Steiner. TiO2 patterning using electro-hydrodynamic lithography. *Soft Matter*, 3 (5):554–557, 2007.

13. ⬀. Leyla Colakerol Arslan, Christopher Sanborn, Eitan Anzenberg, and Jr. Ludwig, Karl F. Evidence for Family-Meakin Dynamical Scaling in Island Growth and Coalescence during Vapor Phase Deposition. *Physical Review Letters*, 109(10):106102, September 2012.

14. ⌞⌝. F. Family and P. Meakin. Kinetics of Droplet Growth-processes - Simulations, Theory, and Experiments. *Physical Review A*, 40(7):3836–3854, October 1989.

15. ⌞⌝. Nicole E. Zander, Joshua A. Orlicki, and Adam M. Rawlett. Thermal and FTIR characterization of poly (4-vinylpyridine) crosslinked with metal salts. *Abstracts of Papers of the American Chemical Society*, 238, August 2009.

16. ⌞⌝. C. X. Guan, D. G. Chen, W. J. Tang, and C. H. Liu. Properties and thermal degradation study of blend films with poly(4-vinylpyridine) and lignin. *Journal of Applied Polymer Science*, 97(5):1875–1879, September 2005.

17. ⌞⌝. L. F. Pease and W. B. Russel. Limitations on length scales for electrostatically induced submicrometer pillars and holes. *Langmuir*, 20(3):795–804, February 2004.

18. ⌞⌝. Joachim Stöhr. *NEXAFS Spectroscopy*. Springer, 1992.

19. ⌞⌝. C. Hennig, K. H. Hallmeier, and R. Szargan. XANES investigation of chemical states of nitrogen in polyaniline. *Synthetic Metals*, 92(2):161–166, January 1998.

20. ⌞⌝. A. Millan, F. Palacio, A. Falqui, E. Snoeck, V. Serin, A. Bhattacharjee, V. Ksenofontov, P. Guetlich, and I. Gilbert. Maghemite polymer nanocomposites with modulated magnetic properties. *Acta Materialia*, 55(6):2201–2209, April 2007.

21. ⌞⌝. A. Millan, A. Urtizberea, E. Natividad, F. Luis, N. J. O. Silva, F. Palacio, I. May-oral, M. L. Ruiz-Gonzalez, J. M. Gonzalez-Calbet, P. Lecante, and V. Serin. Akaganeite polymer nanocomposites. *Polymer*, 50(5):1088–1094, February 2009.

22. ⌞⌝. S. Fujii, S. P. Armes, T. Araki, and H. Ade. Direct imaging and spectroscopic characterization of stimulus-responsive microgels. *Journal of the American Chemical Society*, 127(48):16808–16809, December 2005.

23. ⌞⌝. Ayseguel Elmaci and Jale Hacaloglu. Thermal degradation of poly(vinylpyridine)s. *Polymer Degradation and Stability*, 94(4):738–743, April 2009.

24. ⌞⌝. Derek Peak and Tom Regier. Direct Observation of Tetrahedrally Coordinated Fe(III) in Ferrihydrite. *Environmental Science & Technology*, 46(6):3163–3168, March 2012.

25. ⌞⌝. E. C. Todd, D. M. Sherman, and J. A. Purton. Surface oxidation of pyrite under ambient atmospheric and aqueous (pH=2 to 10) conditions: Electronic structure and

mineralogy from X-ray absorption spectroscopy. *Geochimica Et Cosmochimica Acta*, 67 (5):PII S0016–7037(02)00957–2, March 2003.

26. ⎙. Debajeet K. Bora, Artur Braun, Selma Erat, Ahmad K. Ariffin, Romy Loehnert, Kevin Sivula, Joerg Toepfer, Michael Grätzel, Recardo Manzke, Thomas Graule, and Edwin C. Constable. Evolution of an Oxygen Near-Edge X-ray Absorption Fine Structure Transition in the Upper Hubbard Band in α-Fe$_2$O$_3$ upon Electrochemical Oxidation. *Journal of Physical Chemistry C*, 115(13):5619–5625, April 2011.

27. ⎙. M. D. Morariu, N. E. Voicu, E. Schaffer, Z. Q. Lin, T. P. Russell, and U. Steiner. Hierarchical structure formation and pattern replication induced by an electric field. *Nature Materials*, 2(1):48–52, January 2003.

Chapter 6

Final Conclusions and Outlooks

We have seen that thin films of metal oxides such as hematite and tungsten oxide are suited for applications as photoanodes for PE water splitting. They have appropriate band gaps for sunlight absorption and are stable against photocorrosion. Nevertheless they are limited by their poor charge conduction lengths. I have proposed two different strategies in order to structure thin films of these metal oxides to decrease the length that charges needs to travel through these oxides and avoid recombination. These strategies were based on a self-assembly of the microstructures, allowing for an inexpensive overall process compared to conventional lithography techniques. In addition, the self-assembled structures possess peculiar geometries that are prone to provide light trapping properties to the thin films. As a result, absorption could be increased inside the photoactive material and compensate for the metal oxide film thinness.

A first self-assembly strategy consisted in the preparation and casting of a solution containing a polyelectrolyte (PSS), a tungsten salt (AMT) and a relatively large concentration of ammonium hydroxide. Upon spin coating of this solution, tungsten rich micrometric domains are formed and were converted into mWO_3 oblate spheroids upon pyrolysis. I have discovered that the micrometric domains formation result from the aggregation of nanometric PSS domains, where the polyelectrolyte is deprotonated and its charge stabilized by a cloud of counterions (NH_4^+). A possible outlook of this study is to test what are the possible alternatives to AMT to form similar self-assembled structures. Seminal results show that other ammonium salts such as ammonium vanadate (NH_4VO_3) can also lead to the formation of

micrometric spheroidal domains. Nevertheless I did not achieve such kind of structuration with other salts so far, due their precipitation in solution or during spin coating.

The aforementioned self-assembly process provides an inexpensive and upscalable route to coat a monolayer of mWO$_3$ micrometric spheroids on conductive FTO glass substrates. I used a subsequent sol-gel process in order to obtain an ultra-thin overlayer of hematite on top of these structures, hence producing a structured photoanode involving an all-oxide n-n semiconductor heterojunction. Such structured electrodes are two-times more photoactive than a similar heterojunction implemented as a flat smooth film. They also exhibit strong photonic features that could be observed in the far field using UV-vis transmission spectroscopy. Interestingly, by varying a single parameter of the self-assembly process, namely the spin coating speed, different size distributions of the spheroids could be achieved. Films with different microspheroids size distribution could thereby be obtained. I gained a basic understanding of the relationship between light trapping and photoactivity of these films by experimenting their PE response and their far-field photonic properties and by simulating the light propagation inside the microstructures. I have shown that such microspheroids can support photonic resonant modes at their core while part of the trapped light is scattered and confined at the surface and between the spheroids. Different prospects can result from this discovery. I started for example to investigate the formation and performance of multilayered films. I have observed that multiple layers of microspheroids can be obtained, for instance by dip coating, and also that the spheroids can be coated on an underlying mWO$_3$ flat film. Different emerging photonic properties can be expected from such geometries. In the case of multiple layers of spheroids, the formation of a photonic band gap comparable to photonic crystals, that can also occur in amorphous structures[1–3]. In the case of a monolayer of spheroids on top of a flat film, deviation of light from normal incidence by the spheroids can lead to the formation of guided modes inside the underlying flat film. A decrease in PE response was observed when implementing these multilayered structures, maybe because of the increased majority charge carrier path length linked to increasing photoanode thickness.

A second self-assembly process, EHL, was also investigated. I have shown that a melted P4VP polymer film loaded with an iron salt (FeCl$_3$) could be destabilized in an electric field. The resulting features are domes that can be "frozen" upon cooling of the film below its glass transition temperature. A hierarchical structure was obtained. It is composed of nanometric droplets mimicking the counter electrode features and micrometric domes which are resulting from the overall average electric field applied between the electrodes. Upon pyrolysis of this

film the structures are preserved and the iron precursor is converted to hematite. Despite the successful use of EHL to obtain original micrometric to nanometric structures no photoelectrochemical response could be measured on these films. This lack of function was attributed to the poor electronic conductivity of the substrates used in order to perform the EHL destabilization. Further investigation are needed in order to apply this self-organization process on conductive substrates such as FTO glass.

In fine I have proven that different structuration strategies relying on polymer self-assembly can be successfully implemented to obtain metal oxide thin film with original morphologies. The resulting films may have emerging photonic properties linked to their microstructure that can improve the performances of metal oxide thin films used as photoanode for water splitting. In addition the control provided by the self-assembly process on the microstructure size distribution can be used to gain basic understanding into the photonic mechanisms linked to this performance increase.

References

1. ⎘. C. J. Jin, X. D. Meng, B. Y. Cheng, Z. L. Li, and D. Z. Zhang. Photonic gap in amorphous photonic materials. *Physical Review B*, 63(19):art. no.–195107, May 2001.

2. ⎘. R. Sapienza, P. D. Garcia, S. Gottardo, J. Bertolotti, M. D. Martin, A. Blanco, L. Vina, D. S. Wiersma, and C. Lopez. Light transport through Mie resonances in photonic glasses. *CLEO/Europe - IQEC 2007. European Conference on Lasers and Electro-Optics and the International Quantum Electronics Conference*, pages 773–773, 2007.

3. ⎘. Pedro David Garcia, Riccardo Sapienza, Alvaro Blanco, and Cefe Lopez. Photonic glass: A novel random material for light. *Advanced Materials*, 19(18):2597–+, September 2007.
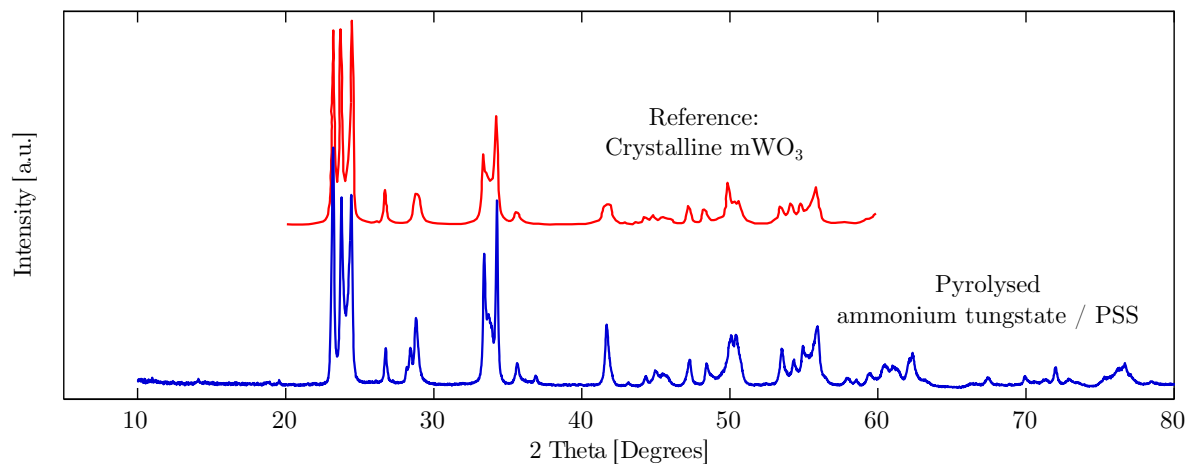
Appendices

Appendix A

Figure A.1: Red curve: Crystalline mWO$_3$ reference spectra scanned from Kuntz *et al.* [2010][*]; Blue curve: X-Ray diffraction spectra of the powder obtained after pyrolysis of 0.5M ammonium tungstate / 0.5M poly(4-styrenesulfonic acid) aqueous solution.
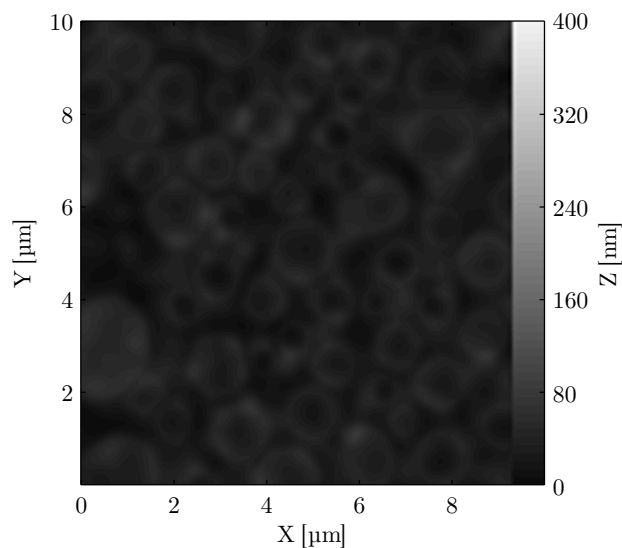
Figure A.2: AFM scan of the film surface obtained by spin coating of an ammonium tungstate/PSS aqueous solution, on FTO glass. Some halos with diameter comparable to the spheroid diameter obtained after pyrolysis are visible. The height of these features is lower than 50 nm and the roughness from the FTO substrate is not visible, suggesting a flat and continuous film.
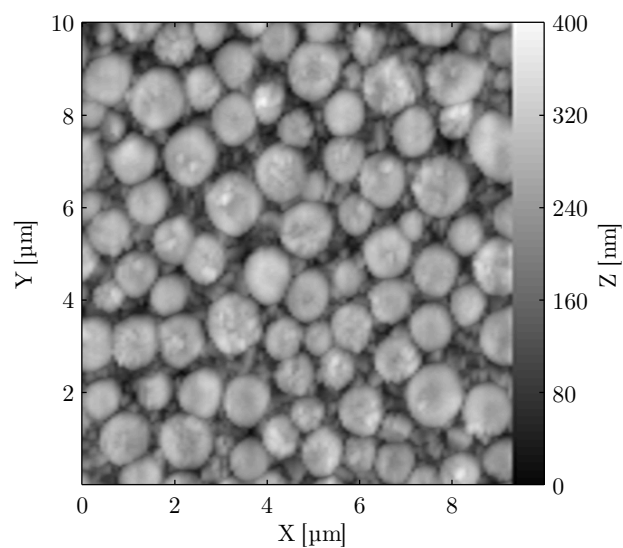
Figure A.3: AFM scan of the film surface obtained after pyrolysis of the film presented in fig. A.2. The film is no more continuous and the mWO$_3$ spheroids are now clearly visible. It is possible to observe the FTO substrate roughness between the spheroids.

Appendix B
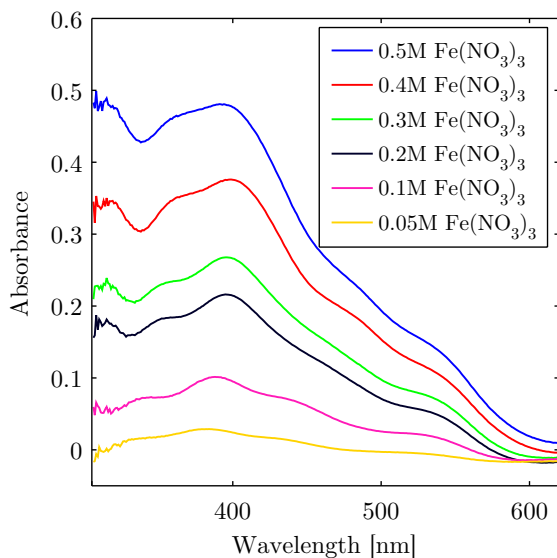

Figure B.1: UV-visible absorption spectroscopy of hematite films of different thickness obtained by spin coating of solutions composed of $Fe(NO_3)_3$ at different concentrations, dissolved in pure ethanol.
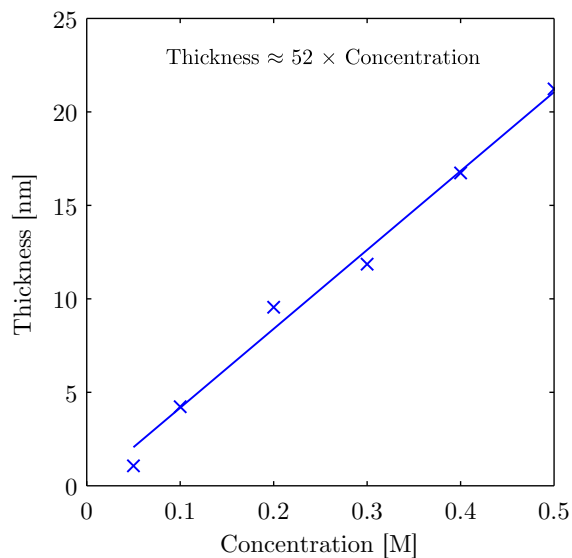
Figure B.2: Variation of the thickness calculated from Beer-Lambert law at 400 nm depending on the $Fe(NO_3)_3$ concentration used to prepare the hematite film (blue circles). The full line represent the linear fitting leading to the relationship: $L = 54 \times [Fe(NO_3)_3]$
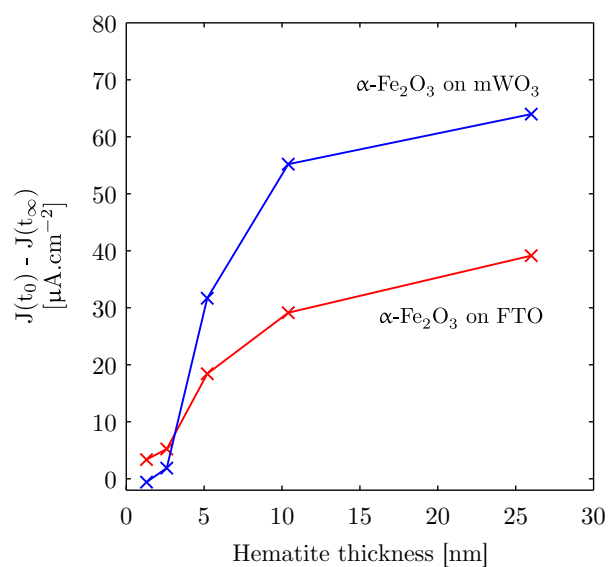
Figure B.3: Comparison of the photocurrent transient amplitude at 0.9V vs Ag/AgCl when different concentrations of $Fe(NO_3)_3$ are spin coated on bare FTO glass substrates and on the microstructured mWO_3 films
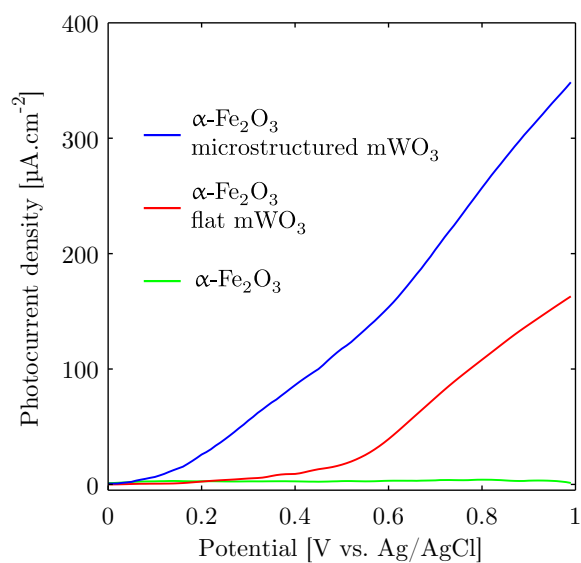
Figure B.4: Comparison of the photocurrents obtained with hematite coated on bare FTO glass (green line), hematite coated on a flat mWO_3 film (red line) and hematite coated on microstructured mWO_3 (blue line)

Appendix C

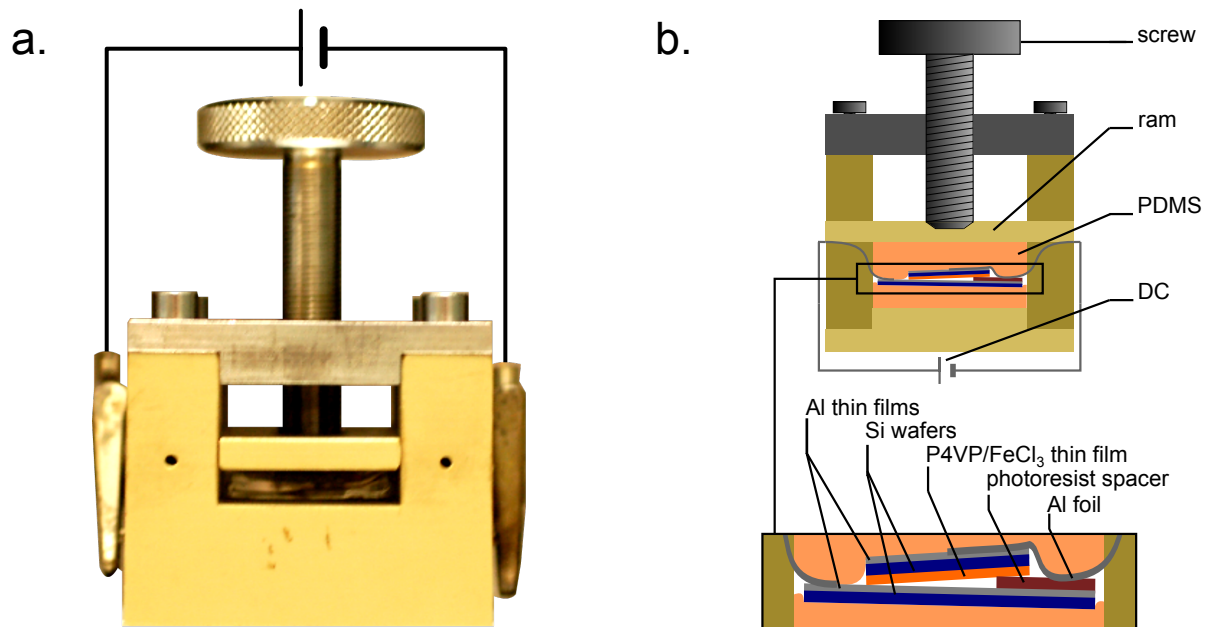## C.1 Details of the setup used for the electrohydrodynamic destabilization

Figure C.1: a. Photograph of the assembly under operation, b. sketch of the assembly design for the electrohydrodynamic destabilization

C.2   NEXAFS spectra with/without electrohydrodynamic destabilization, before pyrolysis
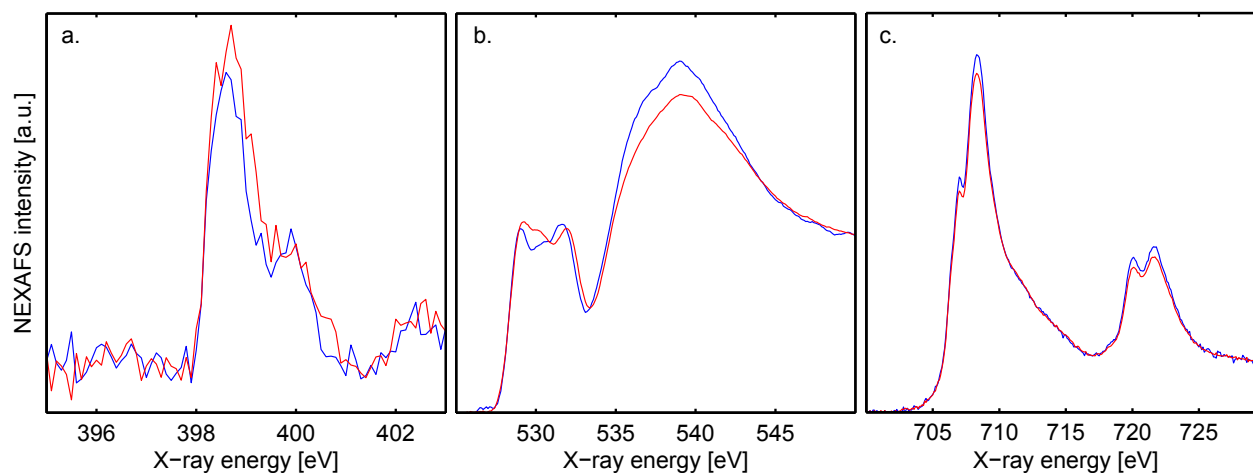

Figure C.2: NEXAFS spectra of the P4VP / FeCl$_3$ thin films with electrohydrodynamic destabilization (blue lines) and without electrohydrodynamic destabilization (red lines); a. At the N K-edge; b. at the O K-edge; c. at the Fe L-edge.

C.3   Matlab - Fiji code for image processing

The purpose of this code is to determine the height and radius distribution of the two kinds of features present on the surface of the film after destabilization. The quality of these measurements can be observed in Figure C.3 which represents graphically the results obtained after image processing.
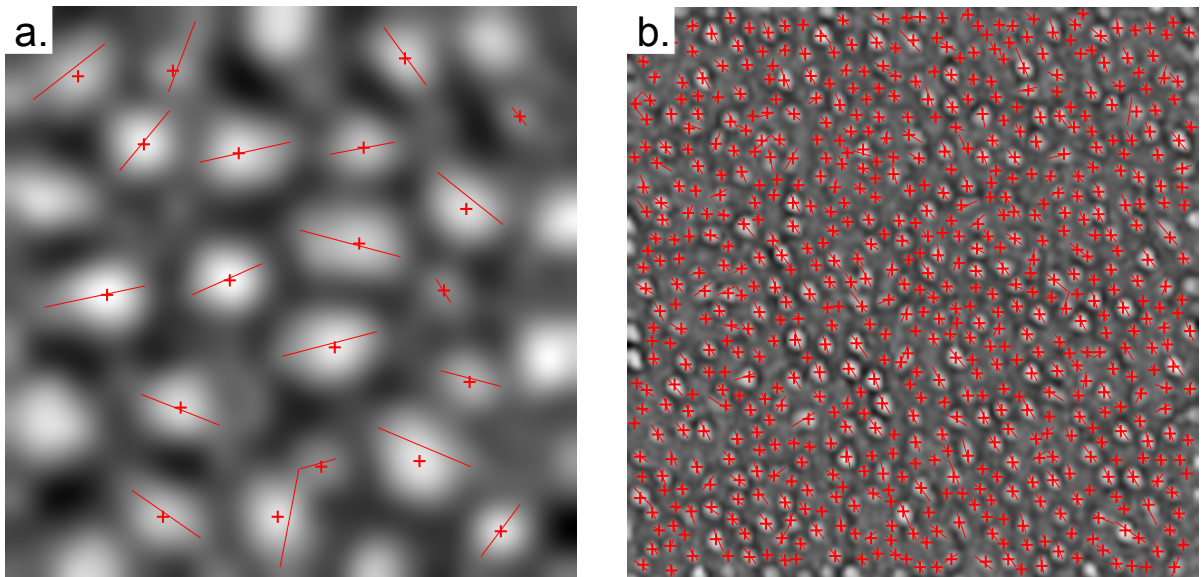

Figure C.3: a. AFM image, processed with a low pass filter, b. AFM image, processed with a high pass filter. On pictures a. and b. the red lines represent the position of the diameter measurements and the cross the position of the height measurements.

The Matlab procedures are used for pre- and post-processing of the data and the Fiji macro has been developed in order to process the images.

```matlab
clear();
close all;

% import the raw data from the AFM which is a three column vector ...
   containing x, y and z coordinates
data=importdata('postAnnealing4.txt');

% make a matrix Z out of the z coordinates
numRaw=512;
for i=1:length(data)/numRaw
    Z(1:numRaw,i)=data((i-1)*numRaw+1:i*numRaw,3);
end

% during AFM scan 128 lines of 512 points are scanned, to obtain a squared ...
   matrix each 128 line of the matrix is repeated 4 times:
for i=1:size(Z,2)
    for j=1:size(Z,1)/size(Z,2)
        squareMatrix(:,j+4*(i-1))=Z(:,i);
    end
end
Z=squareMatrix;

% the scale is set to 10 nanometers and the minimum set to zero to obtain ...
   a convenient format for handling in Fiji:
Z=Z*10^8;
Z=Z-min(min(Z));

% writing the Z matrix to a text file
save textImage.txt Z -ASCII

figure(1), imshow(Z,[min(min(Z)) max(max(Z))]);
```

```
//define the cutoff values for the low pass filter (sub—micrometric ...
   features) and the high pass filter (nanometric features)
var lowPassLim=30;
var highPassLim=10;

//SEPARATION OF THE NANOMETRIC AND SUBMICROMETRIC FEATURES

//open text image created in Matlab from the AFM data
run("Text Image... ", "open=C:\\Users\\Florent\\Desktop\\textImage.txt");
rename("data");

//apply the low pass filter
selectWindow("data");
run("Duplicate...", "title=submicrometric");
run("Bandpass Filter...", "filter_large=100000 filter_small=lowPassLim ...
   suppress=None tolerance=5 autoscale"); //low pass filter
saveAs("Text Image", "C:\\...\\submicrometric.txt"); //saving the ...
   processed image for Matlab

//apply the high pass filter
selectWindow("data");
run("Duplicate...", "title=nanometric");
run("Gaussian Blur...", "sigma=2"); //Gaussian blur is applied to remove ...
   the noise
run("Bandpass Filter...", "filter_large=highPassLim filter_small=0 ...
   suppress=None tolerance=5 autoscale"); //high pass filter
saveAs("Text Image", "C:\\...\\nanometric.txt"); //saving the processed ...
   image for Matlab

//MEASURING FEATURE DIAMETER AND LOCAL MAXIMA COORDINATES

run("Set Measurements...", "  feret's redirect=None decimal=3"); ...
   //definition of the measurement: diameter

//measurements for the submicrometric distribution:

//diameter measurement
selectWindow("submicrometric");
run("Duplicate...", "title=segmentationSubmicrometric");
run("8—bit"); //an 8—bit image is needed to process the orignal image to a ...
   binary image
run("Convert to Mask"); //binarize the image
run("Watershed"); //the watershed procedure allows segmentation of joining ...
   features
run("Analyze Particles...", "size=0.25—Infinity circularity=0.00—1.00 ...
   show=Masks  display exclude clear"); //diameter measurement of ...
   segmented features
saveAs("Results", "C:\\...\\diameterSubmicrometric.txt"); //saving the ...
   diameter measurement for Matlab
rename("diameterSubmicrometric");
```

```matlab
clear();
close all;

% loading the data saved in Fiji

submicrometric = importdata('submicrometric.txt');
nanometric = importdata('nanometric.txt');

dataImport = importdata('maximaNanometric.txt');
maximaNanometric =dataImport.data;

dataImport = importdata('maximaSubmicrometric.txt');
maximaSubmicrometric =dataImport.data;

dataImport = importdata('diameterSubmicrometric.txt');
diameterSubmicrometric =dataImport.data;

dataImport = importdata('diameterNanometric.txt');
diameterNanometric =dataImport.data;

% finding the heights corresponding to the maxima coordinates on the image ...
    processed with a low pass filter (submicrometric features) and ...
    representing both diameter and maxima positions for control

maxima=maximaSubmicrometric(:,2:3);
diameter=diameterSubmicrometric;

Z= submicrometric;
figure(1), imshow(Z,[min(min(Z)) max(max(Z))]); % the result of this plot ...
    is shown in Fig. 2 a.)
hold on;
for i=1:length(maxima)
    yPos=maxima(i,1)+1; % read the y coordinate from the maxima number i
    xPos=maxima(i,2)+1; % read the x coordinate from the maxima number i
    heightSubmicrometric(i)=Z(xPos,yPos);
    plot(yPos, xPos,'+'); % plot the maxima position
end
% plotting the diameter position
for i=1:length(diameter)
        if(diameter(i,5)≥90)
    plot([diameter(i,3);...
        diameter(i,3)−diameter(i,2)*cosd(diameter(i,5))],...
        [diameter(i,4);...
        diameter(i,4)+diameter(i,2)*sind(diameter(i,5))]);
    else
        plot([diameter(i,3);...
        diameter(i,3)+diameter(i,2)*cosd(diameter(i,5))],...
        [diameter(i,4);...
        diameter(i,4)−diameter(i,2)*sind(diameter(i,5))]);
    end
end
```

```matlab
hold off;

% finding the heights corresponding to the maxima coordinates on the image ...
    processed with a high pass filter (nanometric features), same procedure ...
    as the one employed for the submicrometric distribution

maxima=maximaNanometric(:,2:3);
diameter=diameterNanometric;
Z= nanometric;
figure(2), imshow(Z,[min(min(Z)) max(max(Z))]); % the result of this plot ...
    is shown in Fig. 2 b.
hold on;
for i=1:length(maxima)
    yPos=maxima(i,1)+1;
    xPos=maxima(i,2)+1;
    heightNanometric(i)=Z(xPos,yPos);
    plot(yPos, xPos,'+');
end
for i=1:length(diameter)
        if(diameter(i,5)≥90)
    plot([diameter(i,3);...
        diameter(i,3)-diameter(i,2)*cosd(diameter(i,5))],...
        [diameter(i,4);...
        diameter(i,4)+diameter(i,2)*sind(diameter(i,5))]);
    else
        plot([diameter(i,3);...
        diameter(i,3)+diameter(i,2)*cosd(diameter(i,5))],...
        [diameter(i,4);...
        diameter(i,4)-diameter(i,2)*sind(diameter(i,5))]);
    end
end

hold off;

% converting the data back to nanometer scale:
rescaledRadiusSubmicrometric=diameterSubmicrometric(:,2)/2*5000/512;% ...
    known distance: 5000 nm, corresponding to 512 pixels. The radius is ...
    chosen over the diameter because it gives a better appreciation of the ...
    features aspect ratio when compared to the height
rescaledHeightSubmicrometric=heightSubmicrometric*10;% the scale was set ...
    for convienience to 10 nm in the first part of the Matlab code
rescaledRadiusNanometric=diameterNanometric(:,2)/2*5000/512;
rescaledHeightNanometric=heightNanometric*10;
```